15^{th} DELTA
User Meeting

&

Annual Report
2019

Dortmund
27. November 2019

Edited by C. Sternemann, R. Wagner,
D. Lützenkirchen-Hecht (2019)

November 2019

Preface

Dear reader, dear colleague,

this annual report is now the 15th, which demonstrates the continuous developments in the fields of accelerator physics and use of synchrotron radiation related to research carried out at DELTA. You'll see a compilation of different projects concerning application of synchrotron radiation and accelerator physics since the last users meeting in November 2018.

The ongoing activities related to accelerator-physics improve the operation and the reliability of the DELTA machine, in particular for orbit correction (using e.g. machine learning methods), beam diagnostics, and continuous work on the radiofrequency systems. Those projects are of great importance for users' daily work with synchrotron radiation and we are very grateful for all the contributions of the technicians, engineers and scientists involved. Experimental developments in the past year include significant progress in the fields of higher harmonic generation using CHG and EEHG schemes and generation of terahertz radiation.

As in the years before, numerous experimental studies conducted at DELTA beamlines are reported in the present annual report, using the entire spectrum of photon energies from the UV-range to hard X-rays, and scattering as well as spectroscopic techniques. Research topics addressed are soft-matter physics and chemistry, polymers, biological systems, as well as semiconductor physics, (bio-) corrosion, and high-pressure physics. The annual report thoroughly mirrors the diversity of research with synchrotron radiation carried out at DELTA.

The success of a facility like DELTA is always directly linked to the commitment of the institutions involved, and we would therefore like to take this opportunity to thank all the universities and research institutions that have contributed to the various experiments and research. We deeply acknowledge the support from TU Dortmund, the funding agencies and the local government, and are looking forward to the upcoming year 2020, expecting many exciting experiments.

Christian Sternemann, Ralph Wagner & Dirk Lützenkirchen-Hecht

Contents:

Instrumentation 1

DELTA radiofrequency systems 3
P. Hartmann, W. Brembt, V. Kniss, A. Leinweber, T. Weis and the DELTA team

Orbit correction using machine learning methods at the storage ring DELTA 5
D. Schirmer

Progress on survey and alignment of the DELTA magnets and vacuum chambers 7
G. Schmidt, B. Büsing, T. Dybiona, S. Khan, B. Sawadski, T. Schulte-Eickhoff

Towards an adaptive orbit-response-matrix model for Twiss-parameter diagnostics and orbit correction at DELTA 9
S. Kötter, T. Weis

Measuring the tune shift with amplitude at the DELTA storage ring 11
S. Kötter, A. Glassl, W. Helml, M. Jebramcik, C. Mai

Integration of a model server into the DELTA control system 13
A. Althaus, D. Schirmer

Harmonic off-axis seeding 15
A. Meyer auf der Heide, B. Büsing, S. Khan, D. Krieg, C. Mai

Progress towards EEHG at the DELTA short-pulse facility 17
B. Büsing, S. Khan, C. Mai, A. Meyer auf der Heide

Towards arbitrary pulse shapes in the THz domain 19
C. Mai, B. Büsing, S. Khan, D. Krieg, A. Meyer auf der Heide

The new wide and small angle scattering setup at beamline BL2 of DELTA 21
E. Schneider, M. Paulus, T. Witt, J. Bolle, L. Hagen, M. Kowalski, W. Tillmann, M. Tolan

High-pressure powder X-ray diffraction at DELTA 23
L. Frentzel-Beyme, P. Kolodzeiski, R. Pallach, S. Henke

Soft X-ray spectroscopy 27

Investigation of thin boron layers on silicon (PureB) by means of x-ray photoelectronspectroscopy (XPS) 29
A.S. Burkowitz, M. Schmitz, L. Kesper, U. Berges, S. Dreiner, D. Weier, L.K. Nanver, C. Westphal

Interaction effects of cathode power, bias voltage, and mid-frequency on the structural and mechanical properties of sputtered amorphous carbon films 31
W. Tillmann, N. F. Lopes Dias, D. Stangier, M. Bayer, H. Moldenhauer, J. Debus, M. Schmitz, U. Berges, C. Westphal

XPS-/XPD-studies on the low-dimensional formation of self-assembled germanium on Ag(110) 33
L. Kesper, C. Kohlmann, M. Schmitz, P. Roese, M. Schulte, U. Berges, C. Westphal

X-ray scattering 35

PECVD Ti-Si-B-C-N nanocomposite coatings for tribological high temperature applications 37
A. Nienhaus

Influence of bias potential on texture and thermal resilience of CrAl(Si)N coatings 41
J. Latarius, D. Stangier, K. Berger, J. Forov, C. Weis, M. Paulus, W. Tillmann, M. Tolan

Studying the feasibility of depositing alumina reinforced Sn-Sb-Cu based composite coatings by means of low pressure cold spraying 43
W. Tillmann, L. Hagen, M. Abdulgader, D. Kokalj, D. Stangier, M. Paulus, M. Tolan

X-Ray diffraction on heat-treated metal foils 47
F. Eckelt, B. Bornmann, R. Wagner, D. Lützenkirchen-Hecht, R. Frahm

Role of microstructure and surface morphology on charge carrier transport in organic semiconductor 49
H. Makowska, M. Brzezinski, O. Yildiz, W. Pisula, T. Marszalek

Supramolecular structure of n-octanol 51
J. Bolle, C. Sternemann, M. Paulus, C. Albers, G. Surmeier, S. Dogan, M. Tolan

In-situ synchrotron powder diffraction on tetraethynylozincates and –cadmates upon heating 53
M. Werker, U. Ruschewitz

Crystalline and highly oriented growth of SCO Hofmann-type coordination polymers over MoS$_2$ flakes 57
A. Núñez-López, R. Torres-Cavanilles, V. Rubio-Giménez, A. Forment-Aliaga, E. Coronado

Crystallinity of swollen PMMA composite films with various GNP and CNT contents 59
O. Ozturk, G. A. Evingur, U. Pietsch

Supramolecular structure of n-octanol/water mixtures 61
J. Bolle, C. Sternemann, M. Paulus, E. Schneider, M. Tolan

The effect of viral fusion peptides on the lamellar to cubic transition dynamics of monoolein in excess water 63
G. Surmeier, M. Paulus, C. Sternemann, M. Elbers, C. Albers, J. Bolle, M. Moron, M. Moron, M. Kowalski, C. Cewe, J. Nase

Gas adsorption on hydrophobic surfaces near the critical point 65
M. Moron, G. Surmeier, J. Bolle, M. Moron, J. Nase, M. Paulus, M. Tolan

Exploring the breathing behaviour of functionalized flexible metal-organic frameworks during n-butane sorption via in situ PXRD 67
R. Pallach, L. Frentzel-Beyme, S. Henke

Temperature-dependent behaviour of oligomer thin films 71
E. Mikayelyan, L. Grodd, V. Ksianzou, D. Wesner, A.I. Rodygin, H. Schönherr, Y. Luponosov, S. Ponomarenko, U. Pietsch, D.A. Ivanov, S. Grigorian

Adsorption of ions at OTS-coated surfaces under an electric potential field 73
A. Sparenberg, M. Paulus, S. Dogan, G. Surmeier, C. Albers, J. Forov, C. Sternemann, M. Tolan

Hard X-ray spectroscopy 75

XANES and EXAFS absorption spectroscopy on cobalt valence tautomers and reference compounds at beamline BL8 77
F. Otte, C. Sternemann, R. Wagner, F. Alves Lima, C. Bressler, M. Tolan

Density determination of liquids in the pressure range up to 5000 bar 79
J. Nase, P. Salmen, M. Paulus, C. Sternemann, M. Tolan

Effect of cultivation conditions on the electrochemical activity of metal reducing bacteria (MRB) on stainless steel surfaces 81
N. Wurzler, J. D. Schütter, R. Wagner, D. Lützenkirchen-Hecht, O. Ozcan

Unravelling the local structure of $(Ca/Sr)F_2{\cdot}(Eu/Tb)F_3$ luminescent nanoparticles 83
A. Guilherme Buzanich, A. Kabelitz, K. Yusenko, R. Wagner

Von Hamos spectrometer commissioning and Kα X-ray emission spectroscopy on cobalt valence tautomers at beamline BL9 85
F. Otte, K. Lehninger, S. Jannuzzi, C. Sternemann, R. Sakrowski, M. Elbers, F. Alves Lima, C. Bressler, M. Tolan

K_β X-ray emission spectroscopy on cobalt valence tautomers at beamline BL9 87
F. Otte, K. Lehninger, C. Sternemann, C. Albers, J. Bolle, R. Sakrowski, F. Alves Lima, C. Bressler, M. Tolan

Cobalt-doping of barium aluminate ($BaAl_2O4$) as investigated by XANES 89
M. Vrankić, A. Šarić, S. Bosnar, D. Lützenkirchen-Hecht, R. Wagner

EXAFS investigations of a noblegas treatment of Nb at elevated temperatures 91
P. Rothweiler, J. Kläs, R. Wagner, D. Lützenkirchen-Hecht

XANES investigations of pea plants exposed to soil contaminated with Cu nanoparticles 93
P. Mathiak, R. Wagner, R. Frahm, D. Lützenkirchen-Hecht

Notes 95

Instrumentation

DELTA radiofrequency systems

P. Hartmann, W. Brembt, V. Kniss, A. Leinweber, T. Weis and the DELTA team

Zentrum für Synchrotronstrahlung (DELTA), Technische Universität Dortmund

Human resources

On April 30, 2019 Wolfgang Brembt retired from the RF group. We thank Wolfgang for 23 years of excellent work. Having him on the team made a big difference. On Oct. 1, 2019 Andreas Leinweber started working in the DELTA RF group.

Linac RF system

While all low-level radiofrequency (RF) components in the linear accelerator (linac) operated without failures in 2019, the linac klystron amplifier shows signs of fatigue after roughly 22,000 hours of operation. A new klystron tube was shipped from the manufacturer in October. It will be installed in spring 2020. The old klystron tube will be kept as a spare while the previous spare will be sent to the manufacturer for refurbishment.

Booster RF system

In August, the PLC (programmable logic controller Siemens S7) of the booster solid state amplifier (SSA) was defective. The SSA manufacturer replaced it by a spare PLC on the same day. Other than that, all components performed the usual way.

Storage ring RF system

A defective power coupler of the DORIS cavity (no water flow through the central rod) was replaced in the spring shutdown by a spare coupler purchased already in 1999. The DORIS cavity performs well ever since.

Preparation for and installation of the HOM damped EU-type cavity in the storage ring

A broken power coupler of the HOM damped EU-type cavity (cavity 2) was replaced in January by a power coupler generously provided by HZB Berlin. In order to avoid this kind of failure in the future, a fast reflected-power interlock was developed which is capable to detect arcing in the coupler and shut down the power amplifier within microseconds. The reflected-power interlock was deployed before the reconditioning of the cavity in the bunker started. Very careful reconditioning of the cavity was undertaken leading eventually to cw operation at 75 kW without any further problems.
In April, cavity 2 was vented with dry nitrogen, removed from the test stand in the bunker and installed in the storage ring. Due to the careful survey in the preparation phase, the storage ring vacuum could be re-established after a few hours and baked to 130°C subsequently. This newly installed cavity is now pumped by two NEG pumps and two additional ion getter pumps in order to provide pumping speed even if the NEG pumps saturate.

The cavity cooler and the cavity interlock system were also installed to the full extent in the storage ring so that any power induced into the cavity by the electron beam could be absorbed. In case of any failure on cavity 2, the power to cavity 1 would have been cut off by

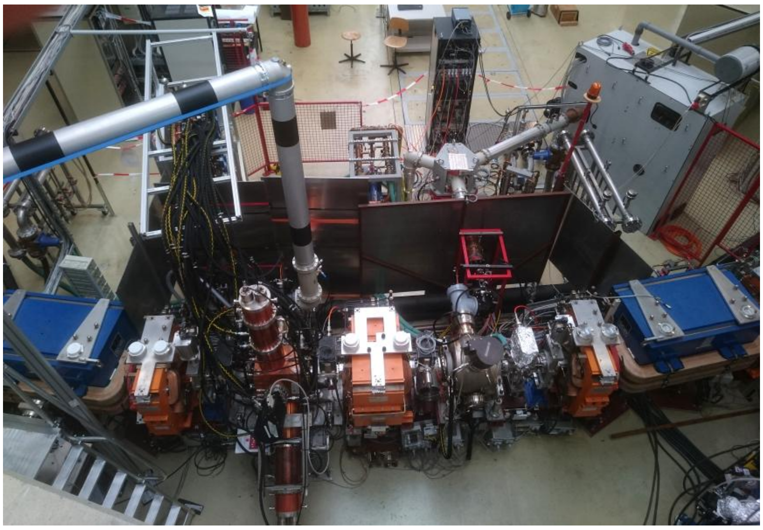

Figure 1: DELTA storage ring RF section with the new HOM-damped EU-type cavity on the left and the old DORIS-type cavity on the right.

the newly installed interlock system. Shortly after the installation of cavity 2, a vacuum leak at the old DESY-style HOM coupler of cavity 1 was encountered. The coupler was removed.

Between April and July the storage ring was still operated by cavity 1 only. The HOM-damped cavity 2 was detuned so that it received less than 5W RF power in ground mode from the electron beam. In the summer shutdown starting in July, the coaxial RF power line between the power circulator and cavity 2 was installed and the cavity was conditioned to 40 kW cw power, which is sufficient to operate the storage ring with cavity 2 only. During conditioning, a micro leak at the cavity probe window was encountered. The probe was replaced by an improved design (so-called ALBA design, drawings provided by A. Salom from ALBA, Barcelona, Spain). Starting in August, the storage ring was operated with cavity 2 active and cavity 1 detuned. For plunger control of cavity 2, the BESSY plunger driver already deployed in the bunker was used.

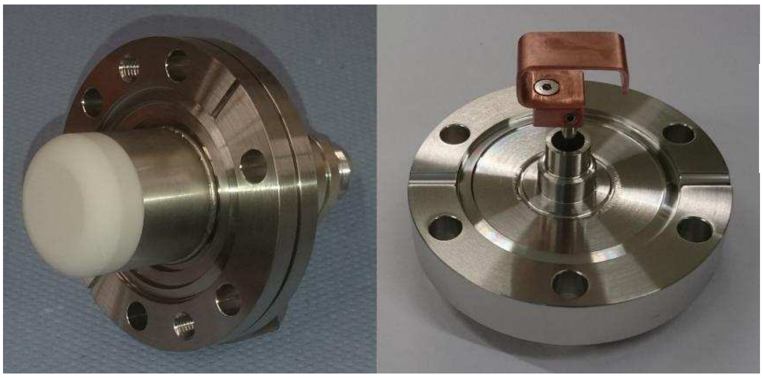

Figure 2: Classic cavity probe (left) and in-vacuum ALBA design (right).

During a one-week shutdown in September, the old low-level RF setup was replaced by a digital low-level RF system (DLLRF) purchased in 2018. After a commissioning phase of three days, the storage ring was operated feeding 25 kW RF power to both cavities. Ever since, two-cavity operation is the standard operational mode of DELTA. Three weeks after installation of the digital low-level RF system, the storage ring started to suffer from frequent beam trips due to reflected power above the trip level in both cavities caused by a failure of the DLLRF system. After a downtime of 4 days, operation could be resumed thanks to a spare DLLRF system provided by KIT, Karlsruhe. The defective system was repaired in November.

Orbit correction using machine learning methods at the storage ring DELTA

D. Schirmer

Zentrum für Synchrotronstrahlung (DELTA), Technische Universität Dortmund

Machine learning (ML) methods have found their application in a wide range of accelerator control tasks. Among other possible use cases, neural networks are utilized for automated control of the electron beam position (orbit correction). Uncorrected orbit implies large beam amplitudes and angles and thus causes vacuum chamber heating, reduces injection efficiency and does not optimally illuminate the synchrotron radiation beamlines. Therefore, conventional fully connected three-layer Feed-Forward Neural Networks (FFNN, see Fig. 1 left) were trained by supervised learning on measured orbits (see Fig. 1 right) to apply local and global beam position corrections at the 1.5-GeV storage ring DELTA [1, 2].

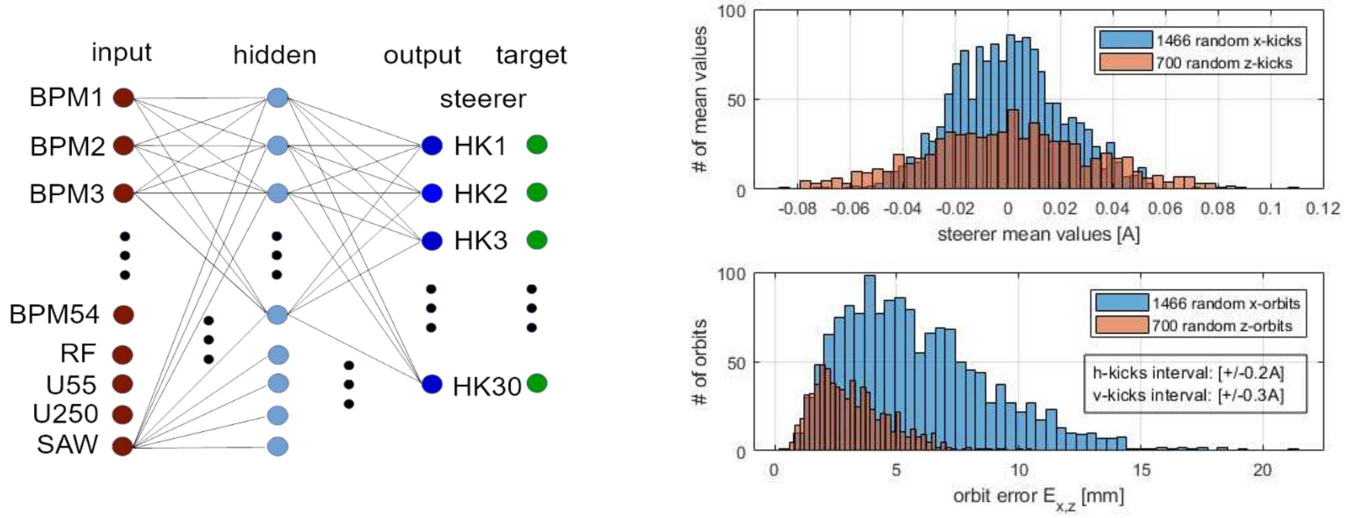

Figure 1: Left: Layout of the Feed-Forward Neural Network (FFNN 58x58x30) for horizontal orbit correction at DELTA (left). The FFNN was trained with several response matrices (BPM readings for positive and negative single steerer kicks) and 1466/700 arbitrary orbits, generated by randomly distributed horizontal and vertical steerer kicks [+/-0.2 A, +/-0.3 A]. Right: Measured ML training target (top) and input (bottom) data for the horizontal (blue) and vertical (red) orbit plane.

The supervised learning was carried out with a back-propagation method using the Levenberg-Marquardt (LM) algorithm with Bayesian Regularization (BR) [3, 4]. The quality of the ML-based orbit correction (OC) was evaluated by the Euclidian norm $E_{x,z}$ which considers the orbit errors in both storage ring planes between the currently measured and a reference orbit at all 54 BPM positions. The correction performance was compared to two other computing methods, singular value decomposition (SVD) [5,6] and cone-based (convex optimization) [7,8] implementations, respectively.

Figure 2 depicts exemplarily the horizontal orbit error depending on correction iterations for randomly disturbed orbits (mean values and corresponding standard deviations). All tested OC algorithms converged to comparable results after multiple successive correction steps. For ML-based OC, the absolute closed orbit error was reduced in average nearly by two orders of magnitude to less than 200 μm after three iterations. Other OC approaches need more iteration steps and fundamentally a higher numerical effort. A further advantage relates to the fact that ML incorporates the real storage ring as it was set up at the time of training data acquisition. Therefore, all machine imperfections like nonlinearities (e.g., sextupole magnets) or other higher-order multipoles due to magnetic fringe fields effects are intrinsically considered.

Although the ML-based OC is only a prototype application so far and the potential has not yet been fully exploited, it has been shown that ML techniques are an alternative approach for automated orbit correction for the DELTA storage ring. Despite ML-based OC being competitive, there is still potential for optimizations [2]. Furthermore, long-term stability and robustness must be proven during standard machine operation.

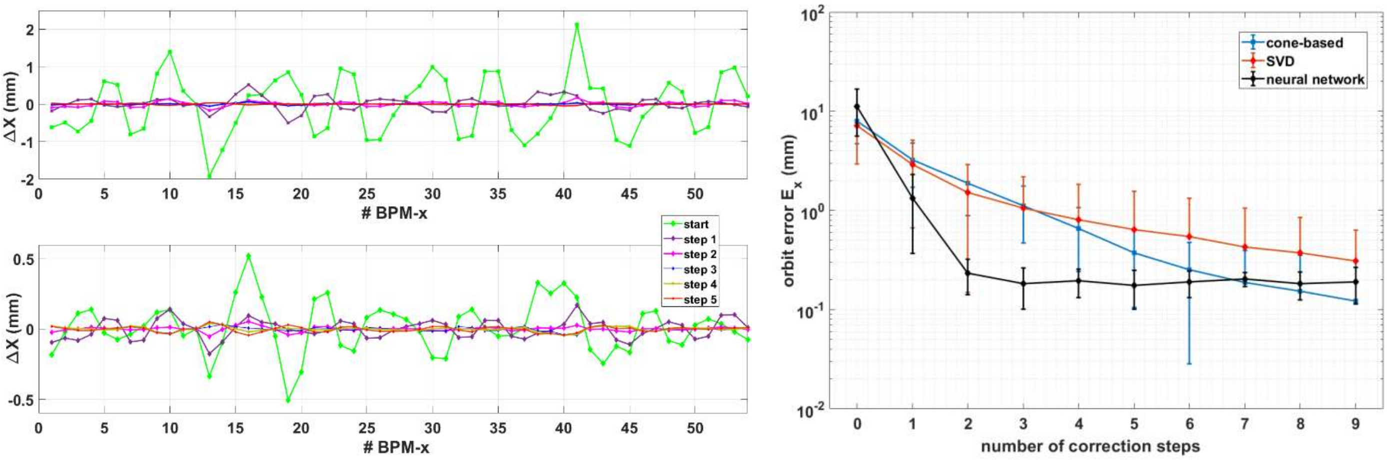

Figure 2: Left: Stepwise application of the LM-BR-pretrained FFNN referred to the previously corrected orbit, starting from a randomly disturbed orbit (green). Right: Performance comparison for different computing orbit correction implementations: Singular value decomposition (SVD), cone-based (convex optimization) and based on machine learning (neural network). For ML-based OC, after 3 successive correction steps, a residual orbit error of < 200 µm was achieved.

References:

[1] D. Schirmer, “Intelligent Controls for the Electron Storage Ring DELTA”, Proc. IPAC’18, Vancouver, Canada, pp. 4855-4858.

[2] D. Schirmer, “Orbit Correction with Machine Learning Techniques at the Synchrotron Light Source DELTA”, Proc. ICALEPCS’19, New York, USA, paper WEPHA138.

[3] David J. and C. MacKay, “Bayesian Interpolation”, Neural Computation, vol. 4, no. 3, pp. 415-447, 1992.

[4] F. Dan Foresee and Martin T. Hagan, “Gauss-Newton Approximation to Bayesian Learning”, Proc. Int. Conf. on Neural Networks (ICNN'97), Jun. 1997, vol. 3, pp. 1930-1935.

[5] E. Zimoch, “Entwicklung und Einsatz eines intelligenten Agentensystems zur Optimierung der Injektion in den Speicherring der Synchrotronstrahlungsquelle DELTA”, Dissertation, TU Dortmund University, Germany, 2003.

[6] M. Grewe, “SVD-basierte Orbitkorrektur am Speicherring Delta”, Dissertation, TU Dortmund University, Germany, 2005.

[7] S. Kötter, A. Glassl, B. D. Isbarn, D. Rohde, M. Sommer, and T. Weis, “Evaluation of an Interior Point Method Specialized in Solving Constrained Convex Optimization Problems for Orbit Correction at the Electron Storage Ring at DELTA”, Proc. IPAC’18, Vancouver, Canada, pp. 3507-3510.

[8] S. Kötter, B. Riemann, and T. Weis, “Status of the Development of a BE-Model-Based Program for Orbit Correction at the Electron Storage Ring DELTA”, Proc. IPAC’17, Copenhagen, Denmark, pp. 673-675.

Progress on survey and alignment of the DELTA magnets and vacuum chambers

G. Schmidt, B. Büsing, T. Dybiona, S. Khan, B. Sawadski, T. Schulte-Eickhoff

Zentrum für Synchrotronstrahlung (DELTA), Technische Universität Dortmund

Overview

The performance of a storage ring regarding beam lifetime, stability and injection efficiency depends on the alignment of all components. If the stored beam passes through the center of the quadrupole magnets, nonlinearities are minimized, the model of the magnetic optics is more accurate and the machine is easier to operate. During the last three years, all quadrupole magnets and vacuum chambers of the storage ring were realigned horizontally [1,2]. The storage ring has now stabilized on a good beam lifetime, high orbit stability, reproducibility of magnet settings, improved injection efficiency and on a low radiation level in the DELTA hall.

Alignment of quadrupole magnets

After adjustments of the quadrupoles section by section during the last years, a general survey of all magnets positions was performed during the summer shutdown using a Leica Absolute Tracker AT 402 [3]. A reference coordinate system for the DELTA magnets, which takes into account several boundary conditions, was adapted to the new length of the DELTA orbit. One constraint is given by the injection bump, another is the fact that the quadrupole magnets cannot be adjusted longitudinally.

The tracker position must be balanced into the local coordinate and reference system of each section, and the balancing procedure was optimized. A new alignment campaign was started to reduce the offsets in some areas of DELTA. Due to previous experience with the quadurpole adjustment, a section of up to a length of 20 m was aligned in one step making the procedure much more time-efficient. The anticipated settings of the respective corrector magnets allowed to store beam immediately after the alignment intervention. Without anticipation of the corrector strength, beam cannot be stored if a focusing quadrupole is moved by about 0.5 mm horizontally. User operation was possible at all beamlines without loss of intensity by retaining the orbit position.

The undulator U55 was adjusted to its target position [4]. The beamline is adjusted in a second step to the reference orbit close to the center of the quadrupole magnets [4].
The superconducting wiggler SAW will be the last insertion device to be adjusted horizontally.

The alignment of quadrupoles was followed by a beam-based calibration of the beam position monitor centers with respect to the corresponding quadrupole centers. During the calibration, several position monitors were found to show offsets which cannot be explained by the alignment procedure. The source of these offsets needs further investigations.

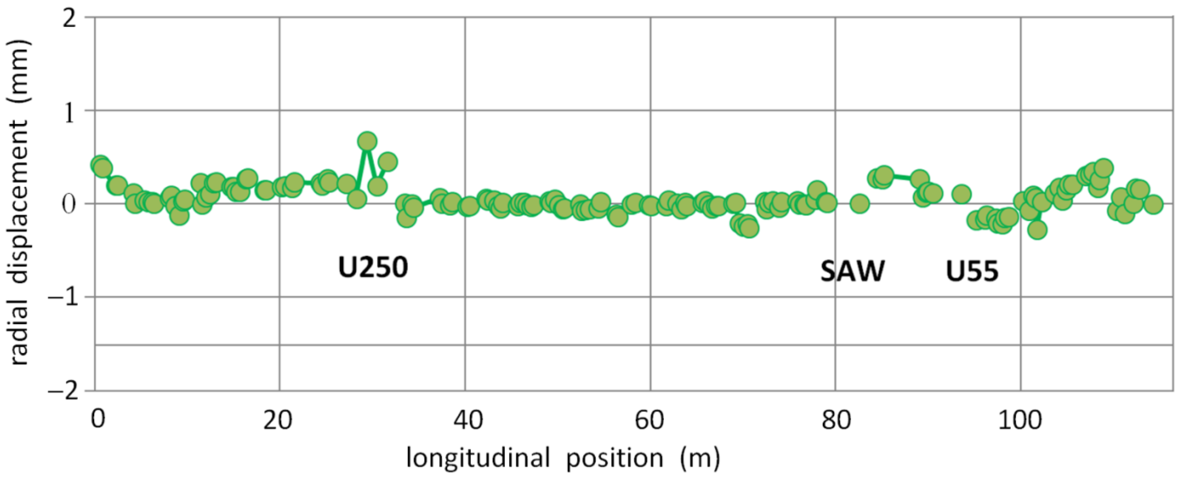

Figure 1: Radial displacement of quadrupole magnets after adjustment. Each magnet is equipped with two alignment marks shown as two dots. The measurement accuracy is ± 0.3 mm.

Outlook

The final goal of the alignment program is a stored electron beam passing through the center of the aligned quadrupole magnets. Sensitive beamlines were aligned horizontally to the new electron reference orbit. At some places, the electron beam must still pass off-center through quadrupole magnets due to injection constraits, lifetime issues and to avoid local heating of the vacuum chamber. Further adjustment of the chambers may be required in these areas.

References

[1] G. Schmidt et al., *Survey and Alignment of the DELTA Magnets and Vacuum Chamber*, DELTA Annual Report 2017.

[2] G. Schmidt et al., *Survey and Alignment of the DELTA Magnets and Vacuum Chamber*, DELTA Annual Report 2018.

[3] Hexagon Metrology GmbH, *Leica Absolut Tracker AT 402*, D-35578 Wetzlar.

[4] U. Berges, private communication.

Towards an adaptive orbit-response-matrix model for Twiss-parameter diagnostics and orbit correction at DELTA

S. Kötter, T. Weis
Center for Synchrotron Radiation (DELTA), TU Dortmund, 44227 Dortmund, Germany

The plan to integrate the bilinear-exponential model with dispersion (BE+d model) [1] into the new slow-orbit feedback software under commissioning for the DELTA storage ring was investigated [2].

The new software applies global corrections to the closed orbit of the storage ring with a maximum rate of about 0.1 Hz [3]. These orbit corrections are characterized by a tuple of corrected orbit displacements and applied changes in steering angles which can be stored in a ring buffer. The BE+d model is an analytic representation of the orbit-response matrix, a measurable quantity which relates orbit displacements and steerings angles. It depends on the beta functions, the betatron phases and the tunes in both planes. Fitting the BE+d model to the ring buffer is possible as long as the data set is large enough. Updating this fit with every orbit correction then results in a live-updated BE+d model. This setup should achieve:

1. Non-invasively obtaining good estimates for beta functions and betatron phases
2. Providing an adaptive orbit-response matrix for estimating correction steps

The closed-orbit bilinear-exponential analysis (COBEA) algorithm is available to fit the BE+d model to a given orbit-response matrix [4]. Applying this algorithm to the ring buffer is possible but requires acquiring the orbit-response matrix via linear regression first. With this approach, the theoretical minimum buffer size is constrained by the number of degrees of freedom of the orbit-response matrix. The new fit method introduced allows fitting the BE+d model directly on the ring buffer by increasing the complexity of the fitted model in three consecutive steps. This reduces the theoretical minimum size of the required buffer to about 1/8th. The performance of both algorithms was tested on a set of measurements. The resulting beta functions are given in Fig. 1. The new fitting procedure yielded results (blue) practically coinciding with COBEA beta functions (green) for fits over the complete set of measurements and still achieved acceptable results on small buffer sizes (red) where the orbit-response fit required to use COBEA at all was underconstrained and therefore applying COBEA was infeasible.

The viability of using a BE+d-model representation of a measured orbit-response matrix for orbit correction was asserted by benchmarking two measuered matrices against their BE+d-model representations with the new slow-orbit-feedback software under development. The number of miscorrections for the BE+d-model of about 7 % was close to the 8 % miscorrections achieved with the measured matrices. Thus, both matrix types work equally well for orbit correction.

Further studies revealed that in order to fit the disperion information in the BE+d model correctly, a very large buffer of over 200 tuples of orbit displacments and steering angles is required.

All in all, integrating a live-updated BE+d model into the slow-orbit-feedback software seems promising. Both alleged capabilities of this setup, achieving good estimates of optical

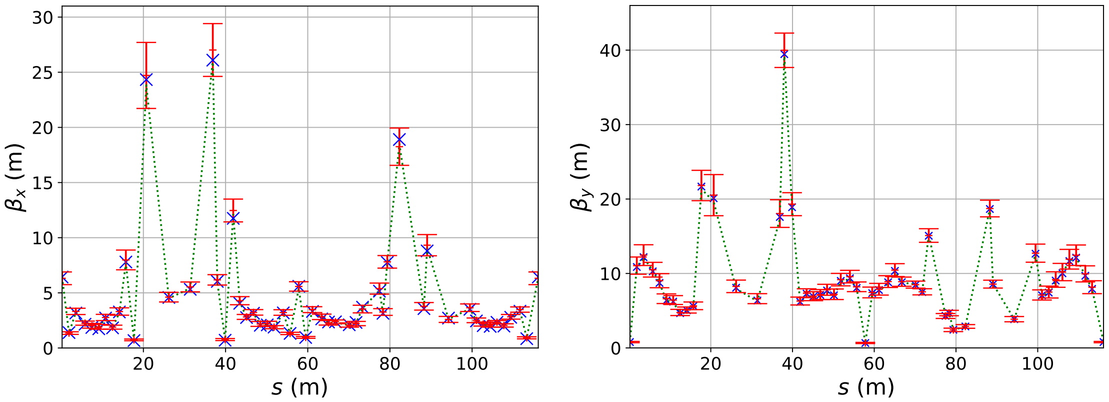

Figure 1: Comparison of average horizontal (left) and vertical beta function (right) at the beam position monitors of the storage ring for fits over the complete set of measurements (blue) and smaller randomly selected subsets (red) with COBEA results (green) as reference. The error bars mark standard deviations calculated accross all fits.

functions and using the fitted model for orbit correction, were supported by measurement results. This idea should therefore be further investigated. Research should target determining a suitable length for the ring buffer and conducting first orbit-correction tests with a preliminary implementation of an adaptive BE+d model.

References

[1] B. Riemann, "The bilinear-exponential closed-orbit model and its application to storage ring beam diagnostics", dissertation, TU Dortmund University, April 2016.

[2] S. Kötter and T. Weis, "Towards an adaptive orbit-response-matrix model for twiss-parameter diagnostics and orbit correction at DELTA", in *Proc. IBIC'19*, paper WECO02, Malmö, Sweden, September 2019.

[3] S. Kötter, A. Glassl, B. Isbarn, D. Rohde, M. Sommer, and T. Weis, "Evaluation of an interior point method specialized in solving constrained convex optimization problems for orbit correction at the electron storage ring at DELTA", in *Proc. IPAC'18*, paper THPAK114, Vancouver, Canada, May 2017.

[4] B. Riemann, S. Kötter, S. Khan, and T. Weis, "COBEA - optical parameters from response matrices without knowledge of magnet strengths", in *Proc. IPAC'17*, paper MOPIK066, Copenhagen, Denmark, May 2017.

Measuring the tune shift with amplitude at the DELTA storage ring

S. Kötter, A. Glassl, W. Helml, M. Jebramcik and C. Mai
Center for Synchrotron Radiation (DELTA), TU Dortmund, 44227 Dortmund, Germany

The tune shift with amplitude (TSWA) was measured by analyzing turn-by-turn data according to methods presented in [1]. This endeavor aims to further characterize non-linear beam dynamics of the DELTA storage ring to enable the development of a beam-optics setting for transverse resonance island buckets (TRIBs) in the future.

In linear beam dynamics, the tune is a constant which determines the betatron phase advance per turn of any particle in the storage ring. The addition of beam-aligned concentric non-linear magnetic fields, as for example sextupole magents, shifts the tune for particles subject to betatron motion with increasing oscillation amplitude. This effect is known as TSWA. It is important for TRIBs optics because it determines the direction in which a resonance has to be approached to detune the island tune towards the resonance.

The TSWA can be reconstructed from turn-by-turn data if coherent betatron motion with large amplitudes is excited. This measurement was achieved by using Libera electronics for recording the transverse beam position and relying on the injection kickers of the storage ring to excite coherent betatron motion. The TSWA was then reconstructed in two steps. First, the oscillation amplitude of the recorded turn-by-turn data was transformed from the position of the beam positon monitor (orange line on the left in Fig 1) to the position at which the oscillation amplitude was largest (pink line on the left in Fig. 1) using a lattice model [2] (left, Fig. 1). Afterwards, the Hilbert transform was applied. According to the reconstructed TSWA (right, Fig. 1), any resonance has to be approached from higher tunes to support the formation of TRIBs.

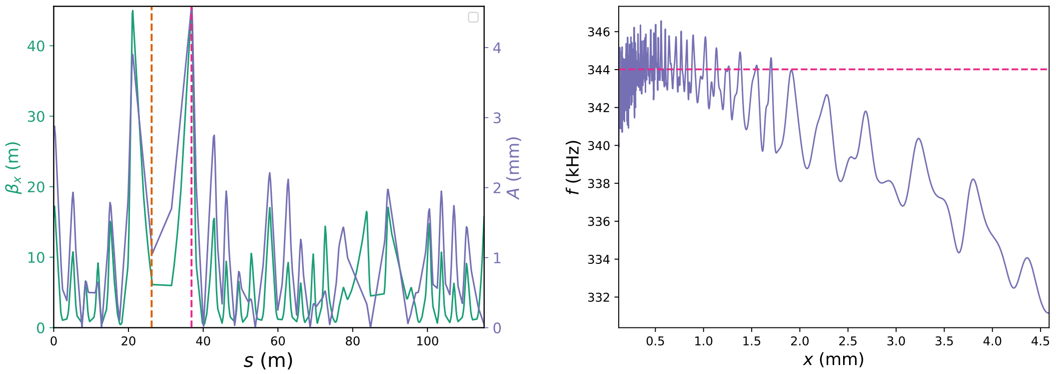

Figure 1: Left: Beta function (green) and betatron-oscillation amplitude (purple) along the beam path of the storage ring including the position of the turn-by-turn capable beam position monitor (orange) and the position of the largest oscillation amplitude (pink). Right: TSWA (purple) and tune (pink) in the horizontal plane.

References

[1] P. Goslawski, F. Kramer, M. Ruprecht, A. Jankowiak, M. Ries, and G. Wüstefeld, "Status of transverse resonance island buckets as bunch separtion scheme", in *Proc. IPAC'17*, paper WEPIK057, Copenhagen, Denmark, May 2017.

[2] S. Hilbrich, "Studies of the DELTA lattice in view of a future short-pulse facility based on echo-enabled harmonic generation", Master's thesis, TU Dortmund University, March 2015.

Integration of a model server into the DELTA control system

André Althaus and Detlev Schirmer

Zentrum für Synchrotronstrahlung (DELTA), Technische Universität Dortmund

During the past years, a variety of particle optics programs have been applied for accelerator studies at the storage ring facility DELTA. Depending on the application, most programs were used offline without dynamic machine synchronization. In order to centralize and standardize storage ring modeling capabilities, a dedicated online model server was developed and integrated into the EPICS-based control system. The core server is based on Python/EPICS service modules using OCELOT [1] and COBEA [2] as simulation tools. All data, actual machine readings/settings, conversion coefficients, results of simulation calculations as well as manual parameter settings, are handled via EPICS process variables (PVs). Thus, the data are transparently available in the entire control system for further processing or visualization. To improve maintainability and adaptability, the remote presentation model controller (RPM) [3] concept was realized in the software implementation.

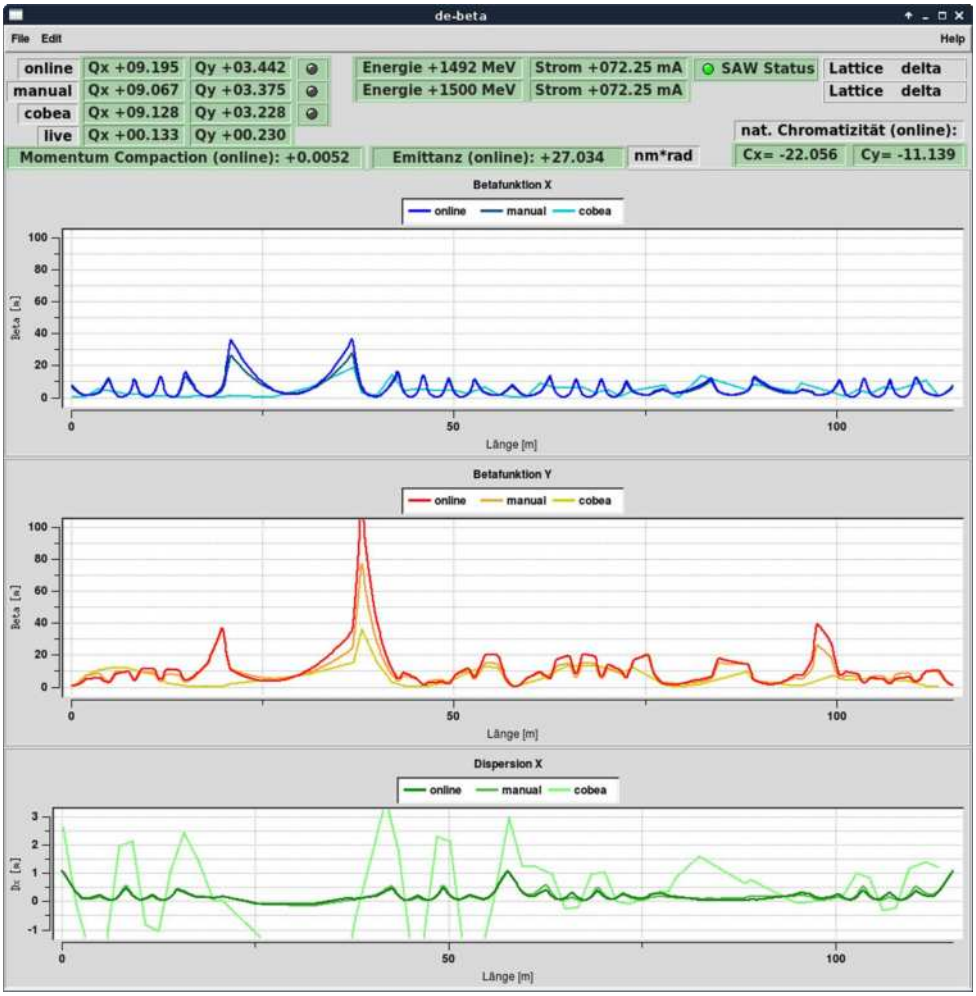

online Qx +09.195 Qy +03.442
manual Qx +09.067 Qy +03.375
cobea Qx +09.128 Qy +03.228
live Qx +00.133 Qy +00.230
Energie +1492 MeV Strom +072.25 mA
Energie +1500 MeV Strom +072.25 mA
SAW Status
Lattice delta
Lattice delta
nat. Chromatizität (online):
Cx= -22.056 Cy= -11.139
Momentum Compaction (online): +0.0052
Emittanz (online): +27.034 nm*rad

Fig. 1: Comparison of optical-function calculations based on online (i2k-converted) and manual values (e.g., design parameters) as well as COBEA results. In addition, the corresponding data of online mode simulations together with live tune measurements are displayed.

Other dedicated graphical user interfaces (GUIs) are available, e.g., to manually set individual magnet currents for offline simulations. The resulting model parameters (manual *k*-values) can be reconverted into new magnet current settings (reverse mode). Furthermore, global machine parameters like beam energy or beam current can be changed individually and assigned to different simulation modes. An important feature is the possibility to exchange (copy) all model parameter settings between the different model server modes. Moreover, stored setup files of real machine magnet settings can be read and the corresponding radiation integrals, calculated by online and manual mode simulations, are displayed in a comparison table.

References:

[1] OCELOT, https://github.com/ocelot-collab/ocelot/.

[2] B. Riemann, S. Kötter, S. Khan and T. Weis, “COBEA - Optical Parameters from Response Matrices without Knowledge of Magnet Strengths”, Proc. IPAC'17, Copenhagen, Denmark, pp. 676-679.

[3] RPM, https://canoo.github.io/dophin-platform/#_the_remote_presentation_model.

Harmonic off-axis seeding

A. Meyer auf der Heide, B. Büsing, S. Khan, D. Krieg, C. Mai
Zentrum für Synchrotronstrahlung (DELTA), Technische Universität Dortmund

Since 2011, seeding experiments by employing the coherent harmonic generation (CHG) scheme [1] are performed [2]. At DELTA, an ultrashort 800-nm laser pulse interacts with a stored electron bunch in an undulator (modulator) which imprints a sinusoidal modulation onto the electron energy. By passing through a magnetic chicane, so-called microbunching occurs, which gives rise to coherent emission at harmonics of the laser wavelength in a subsequent undulator (radiator). The modulation amplitude correlates with the spontaneous synchrotron light emission at the same wavelength, polarization and emission angle as the laser beam. Since the second harmonic of undulator emission only exists off-axis (Fig. 1), seeding with a 400-nm laser pulse in an undulator tuned to 800 nm is only possible by introducing a crossing angle between laser pulse and electron beam.

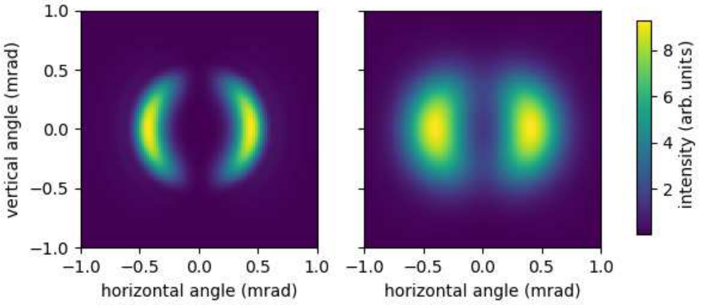

Figure 1: Left: Angular distribution of 400-nm radiation from an undulator tuned to 775 nm as calculated with SPECTRA [3]. Right: Convolution with a 2-dimensional Gaussian includes the effect of laser beam divergence [4].

To measure the amount of modulation, a THz signal also caused by the laser-electron interaction [5] is monitored while the crossing angle is varied by manipulating the electron beam orbit. The obtained signals are presented in Fig. 2. A scan of the horizontal crossing angle shows the expected double-peak structure in the THz signal, since a crossing angle ≠ 0 is required. In the top-left corner, a coarse 2D-scan of the crossing angles is shown, which resembles the expected angular distribution according to the SPECTRA [3] calculations.

The small intensity asymmetry is currently under investigation and first results indicate that the spontaneous undulator emission shows the same asymmetry.

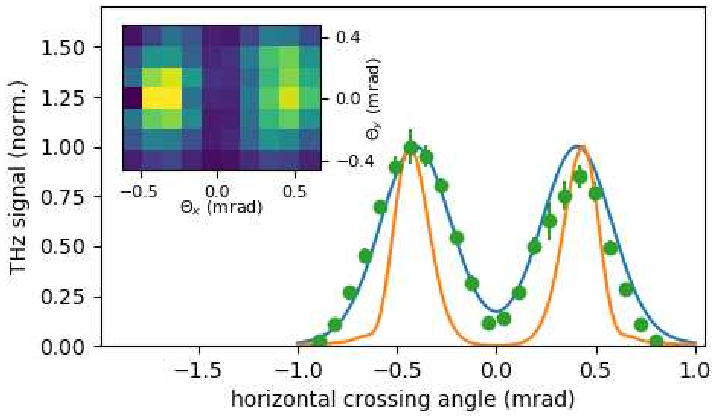

Figure 2: Normalized THz signal (dots) under variation of the horizontal crossing angle at zero vertical angle together with SPECTRA calculations without (orange) and including (blue) the laser divergence (see Fig. 1). Inset: THz signal under coarse variation of the horizontal and vertical crossing angles $\theta_{x,y}$ [4].

References

[1] R. Coisson and F. De Martini, *Free-electron coherent relativistic scatterer for UV-generation*, in Physics of Quantum Electronics 9, edited by S. F. Jacobs et al., USA: Addison Wesley, 1982, p. 939.

[2] S. Khan et al., *Coherent Harmonic Generation at DELTA: A New Facility for Ultrashort Pulses in the VUV and THz Regime*, Sync. Rad. News 24(5), 2011, pp. 18-23.

[3] T. Tanaka and H. Kitamura, *SPECTRA: a synchrotron radiation calculation code*, J. Synchrotron Rad. 8, 2001, pp. 1221-1228.

[4] A. Meyer auf der Heide et al., *The DELTA Short-Pulse Source: Upgrade Plans from CHG to EEHG*, IPAC 2019, Melbourne, Australia, pp. 1457-1460.

[5] M. Höner et al., "A Dedicated THz Beamline at DELTA", IPAC 2011, San Sebastián, Spain, pp. 2939-2941.

Progress towards EEHG at the DELTA short-pulse facility

B. Büsing, S. Khan, C. Mai, A. Meyer auf der Heide
Zentrum für Synchrotronstrahlung (DELTA), Technische Universität Dortmund

Overview

Echo-enabled harmonic generation (EEHG) is a seeding scheme for free-electron lasers proposed in 2009 [1]. As shown in Fig. 1 (left), it is based on a twofold laser-induced modulation of the energy of relativistic electrons. Test experiments were conducted at SLAC in the USA, SINAP in China, and at FERMI in Italy [2-4]. EEHG is also proposed as a method to generate ultrashort pulses in storage rings [5,6]. Compared to coherent harmonic generation (CHG) presently employed at the DELTA short-pulse facility [7], EEHG will enable coherent emission at higher harmonics of the laser wavelength. DELTA is presently the only storage ring worldwide at which the implementation of EEHG is planned.

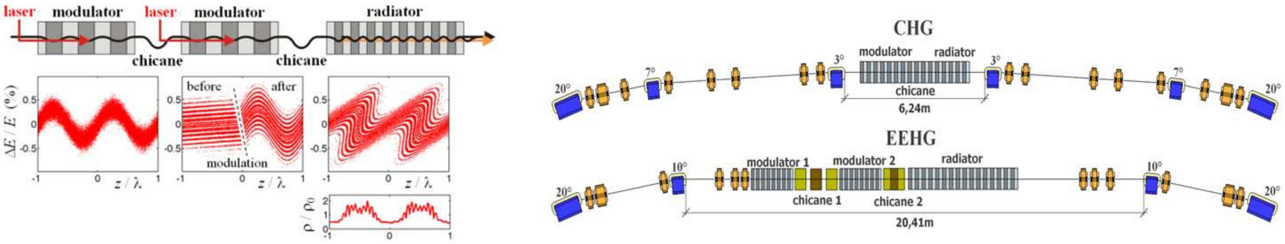

Figure 1: Left: EEHG principle with twofold laser-induced energy modulation in two undulators (modulators) converted into microbunching by magnetic chicanes and coherent emission at high laser harmonics in a third undulator (radiator). Right: Present CHG (top) and planed EEHG (bottom) configuration in the northern part of the DELTA storage ring [8].

BPM positioning and vacuum chamber set-up

After defining the magnet positions it is necessary to find suitable positions for beam-position monitors (BPMs). Some BPM positions are pre-defined due to the design of undulator chambers. To get an idea for the right positions the response matrix was simulated (Fig. 2) and the normalized sum of the response was calculated as an indicator for a good position (Fig. 3).

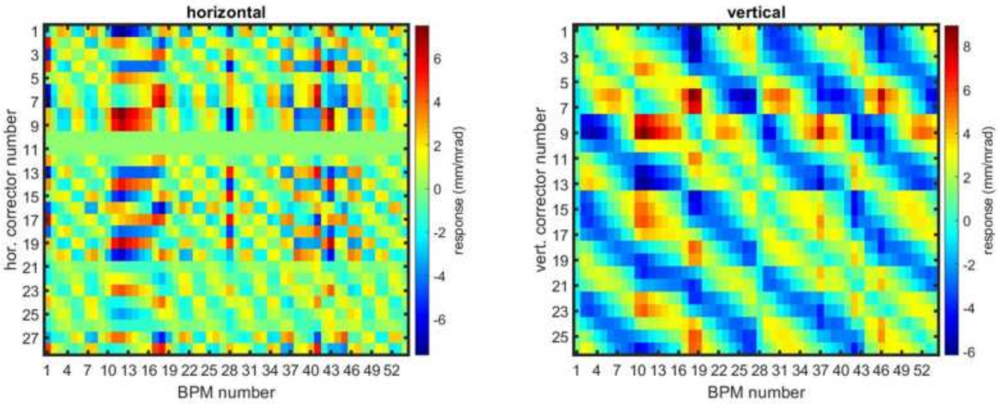

Figure 2: BPM response to corrector kicks. Left: Horizontal response matrix, where correctors 10 and 11 are not yet included in the modified storage ring optics. Right: Vertical response matrix.

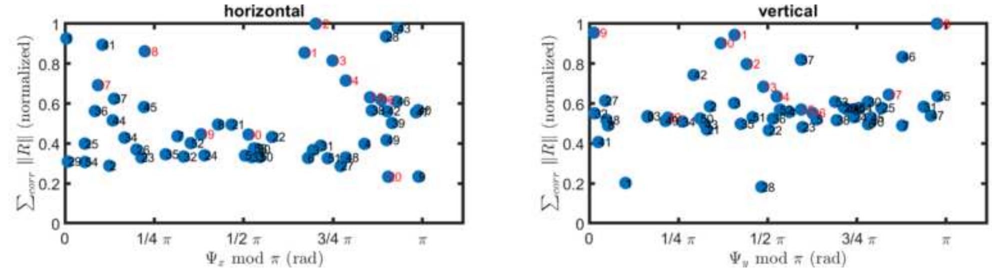

Figure 3: Normalized sum of the BPM responses as function of the horizontal (left) and vertical (right) phase advance. Red numbers indicate the BPMs in the EEHG section.

Hardware

For the implementation of EEHG at DELTA, two new electromagnetic modulators (period length 200 mm, 7 periods) are already in house and tested [9] while the present U250 undulator (period length 250 mm, 17 periods) will be employed as radiator. Vacuum chambers for the modulators are currently manufactured and new dipole chambers were designed [10].

Outlook

With the now defined magnet and BPM positions, the rearrangement of the vacuum chambers including calculations for the vacuum system (pump positions) can be planned.

References

[1] G. Stupakov, *Using the Beam-Echo Effect for Generation of Short-Wavelength Radiation*, Phys. Rev. Lett. 102, 074801 (2009).

[2] Z. Zhao et al., *First lasing of an echo-enabled harmonic generation free-electron laser*, Nature Photonics 6, 360 (2012).

[3] E. Hemsing et al., *Echo-enabled harmonics up to the 75th order from precisely tailored electron beams*, Nature Photonics 10, 512 (2016).

[4] P. R. Ribič et al., *Coherent soft X-ray pulses from an echo-enabled harmonic generation free-electron laser*, Nature Photonics 13, 555 (2019).

[5] C. Evain et al., *Soft x-ray femtosecond coherent undulator radiation in a storage ring*, New J. Phys. 14, 023003 (2012).

[6] R. Molo et al., *EEHG and Femtoslicing at DELTA*, Proc. FEL 2013, New York, USA, 594.

[7] S. Khan et al., *Generation of Ultrashort and Coherent Synchrotron Radiation Pulses at DELTA*, Sync. Rad. News 26:3, 25 (2013).

[8] A. Meyer auf der Heide et al., *The DELTA Short-Pulse Source: Upgrade Plans from CHG to EEHG*, Proc. IPAC 2019, Melbourne, 1457.

[9] D. Zimmermann, *Aufbau eines Magnetmessstandes zur Feldvermessung von Undulatoren bei DELTA*, Master Thesis, TU Dortmund (2016).

[10] B. Büsing, *Teilchenoptische Auslegung und Entwicklung von Dipolkammern für die EEHG-basierte Kurzpulsquelle bei DELTA*, Master Thesis, TU Dortmund (2017).

Towards arbitrary pulse shapes in the THz domain

C. Mai, B. Büsing, S. Khan, D. Krieg, A. Meyer auf der Heide
Zentrum für Synchrotronstrahlung (DELTA), Technische Universität Dortmund

Generation of THz radiation at DELTA

At DELTA, a dedicated beamline for experiments with (sub-)THz radiation is in operation since 2011 [1]. Here, an interaction of short laser pulses with electron bunches is used to give rise to coherent emission of broadband as well as tunable narrowband radiation from 75 GHz to 6 THz. A laser-induced, sinusoidal energy modulation of a short slice of the electrons inside the electromagnetic undulator U250 is converted into a modulation of the longitudinal density profile of the electron bunch. For the generation of broadband radiation, a ps-scale density dip is used, whereas a periodic density modulation leads to narrowband emission.

Laser-pulse shaping by liquid crystal phase modulators

During the past years, the longitudinal shaping of laser pulses with periodic patterns was studied at DELTA to improve the properties of the narrowband THz generation process [2-5]. One possibility is to use the interference of two stretched, and hence chirped, pulses with a short delay which leads to a beating on the (sub-)ps timescale. However, the beating frequency determines the THz output frequency and therefore nonlinearities of the chirp lead to spectral broadening and asymmetries of the spectra, as shown in Fig. 1.

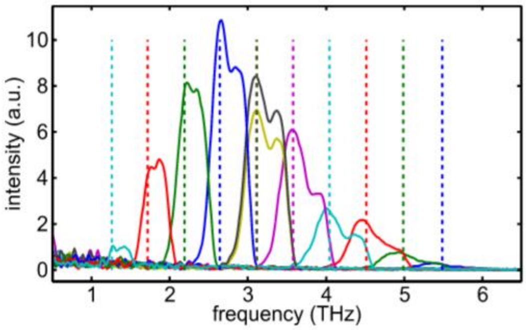

Figure 1: Spectra of tunable THz radiation, which were generated using an interferometric setup (see text for details).

Two dimensional arrays of voltage controlled liquid-crystals are commercially available as laser reflectors which allow for a pixelwise phase shift of the laser wavefront. These computer-controllable devices are known as *spatial light modulators*. The spatially separated pixel mask can be used to influence the temporal profile of a laser pulse by transforming the laser pulse to the Fourier plane by a grating (see Fig. 2, left). The grating introduces a correlation between the transverse coordinate of the modulator and the laser wavelength. Hence, a periodic phase shift leads to a periodic modulation of the laser pulse after retransforming the pulse with another grating. By changing the periodicity of the spatial phase modulation, the central frequency can be varied freely. Experimental studies reached frequencies from 75 GHz to 6 THz [5]. Figure 2 (right) shows spectra of controllable THz radiation recorded with a Fourier-transform spectrometer. The spectral width is controlled by changing the number of phase modulation periods (outer and inner lines at every peak). Here, a relative spectral widths as low as 1.5 % (FWHM) was reached. Furthermore, two or more phase configurations can be superimposed to achieve more than one peak in the spectrum.

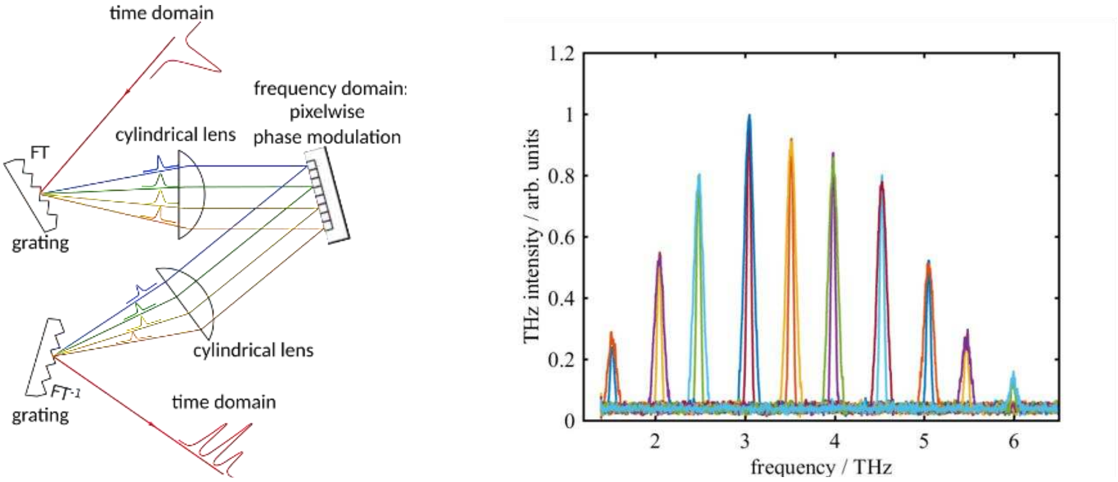

Figure 2: Left: Setup to transform a laser pulse to the Fourier plane before a spatial light modulator introduces a frequency-dependent phase modulation. Back-transforming the pulse by a second grating results in a periodic intensity modulation used for the laser-electron interaction. Right: Spectra of THz radiation generated with the setup based on spatial light modulation. Different line colors at same peak position indicate the change of spectral width between two configurations.

References

[1] M. Höner et al., *A dedicated THz-Beamline at DELTA*, IPAC 2011, San Sebastian, 3074.

[2] A. Weling et al., *Novel sources and detectors for coherent tunable narrow-band terahertz radiation in free space*, J. Opt. Soc. Am. B 13, 2783 (1996).

[3] P. Ungelenk et al., *Studies of Ultrashort THz Pulses at DELTA*, IPAC 2014, Dresden, 1936.

[4] P. Ungelenk et al., *Continuously tunable narrowband pulses in the THz gap from laser-modulated electron bunches in a storage ring*, Phys. Rev. Accel. Beams 20, 020706 (2017).

[5] C. Mai et al., *A Tunable Narrowband Source in the Sub-THz and THz Range at DELTA*, IPAC 2018, Vancouver, 4534.

The new wide and small angle scattering setup at beamline BL2 of DELTA

Eric Schneider[1], Michael Paulus[1], Thorsten Witt[1], Jennifer Bolle[1], Leif Hagen[2], Marvin Kowalski[1] , Wolfgang Tillmann[2] and Metin Tolan[1]
[1]Fakultät Physik/DELTA, Technische Universität Dortmund, 44221 Dortmund, Germany

[2]Institute of Materials Engineering, TU Dortmund University, Dortmund, Germany

The beamline BL2 was a bending magnet beamline operating only with white beam. Consequently, the beamline was used in the past predominantly for x-ray fluorescence spectroscopy and tomography. In order to overcome this limitation, a multilayer monochromator set up was installed in the last year providing monochromatic radiation in an energy range around 12 keV, allowing wide angle and small angle x-ray scattering.

As the critical energy of the bending magnet is 2.2 keV, the photon flux drops down in the hard x-ray regime above 10 keV. Thus, monochromators with relatively low energy resolution compared to single crystal monochromators are well suited to keep the photon flux on a high level. Therefor a PdB_4C multilayer mirror was installed in the experimental hutch providing an energy resolution ΔE/E of 1.5 %. The flat multilayer consists of 100 slabs. These slabs are divided in two sublayers of the same thickness of 1.69 nm (Pd, and B_4C) yielding a suppression of higher harmonics. The choice of Pd was motivated by the energy of the Kα and L emission lines which are far from the working energy (around 12 keV) of the monochromator (Pd Kα = 21 keV, Pd Lα = 2.8 keV). The multilayer is prepared on a flat silicon substrate covering an area of 92 x 50 mm^2. The mirror is placed in an aluminum housing with two polyimid windows for beam entrance and exit. The housing is permanently flushed by helium in order to prevent the formation of ozone and to protect the mirror's surface from humidity. The production of ozone in combination with water cause a fast disintegration of multilayer structures. The whole monochromator is placed on a Huber translation and rotation stage which allows an alignment of the multilayer and the choice of the photon energy. In front of the monochomator a 0.2 mm thick aluminum foil is installed which removes the low energy spectrum of the photon beam. Furthermore, a fast absorber and a jj-x-ray slit system are installed in front of the monochromator. The slit system defines the beam size to typically 0.5 x 0.5 mm^2. At a photon energy of 12 keV, the beam is deflected 0.9 ° downwards and passes a guard silt of 1 x 1 mm^2 size. The sample stage consists of a Huber stage which allows to translate and rotate the sample in all three dimensions. For detection of the scattered beam a PILATUS 100k and a MAR345 image plate detector are available. For x-ray fluorescence measurements an Amptec x-123 spectrometer can be used. A sketch of the setup is shown in figure 1. Actually, a flightpath for SAXS experiments, which has to be installed behind the sample is under construction. A Linkam temperature controlled stage and high hydrostatic pressure cell are available. In a commission run the photon flux at the sample position at 12 keV was determined to 3 x 10^9 photons/s/mm^2. The energy resolution ΔE/E of the multilayer was confirmed to 1.5%.

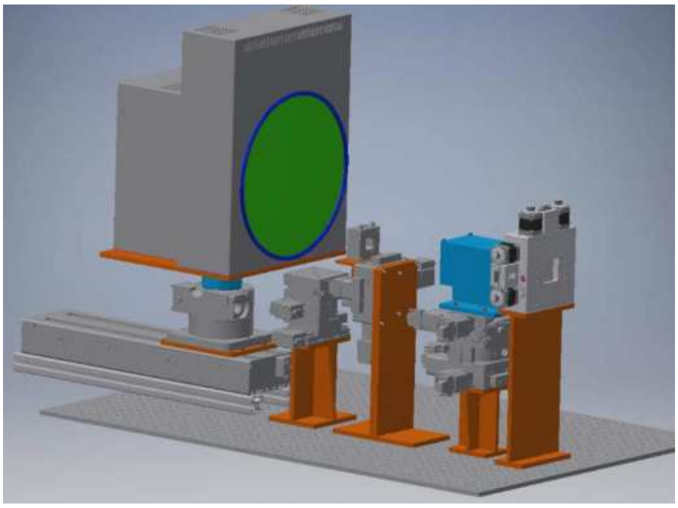

Figure 1: Sketch of the experimental setup

In first experimental runs wide and small angel x-ray scattering experiments were performed. Among other, the phase composition of tungsten carbide – cobalt feedstock material was analyzed. Due to their high hardness and the resulting wear resistance, they have established themselves in many different industrial applications. During production of the feedstock material the formation of phases such as W_3Co_3C or W_6Co_6C can occur. These so called η-phase compounds are undesirable as they increase the porosity and brittleness of the coating [1, 2]. Different samples were examined for their composition by X-ray diffraction. The results are shown in Figure 2.

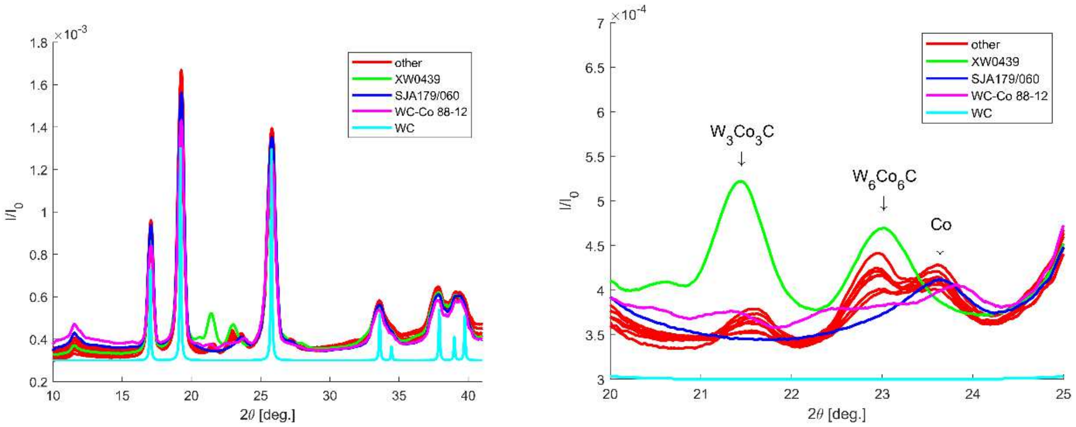

Figure 2: left: X-ray diffraction patterns of WC-Co feedstock materials and WC reference Right: Section of the XRD pattern showing the Bragg reflections of η-phases.

The measurements show that SJA179/060 is the only sample that has no η-phases. This study shows that phase analyses can be carried out well at BL2.

Acknowledgments: We acknowledge the Delta machine group for providing synchrotron radiation and technical support.

Reference

[1] Antonio Formisano et al., Influence of Eta-Phase on Wear Behavior of WC-Co Carbides, in: Advances in Tribology 2016 (Jan. 2016), S. 1-6,

[2] Wolfgang Tillmann et al., Nanostructured WC-Co coatings manufactured by fine powders (-10+2 _m) with ultra-fine carbides (400 nm) by means of HVOF, in: DVS Congress 276 (Sep. 2011), S. 167-173.

High-pressure powder X-ray diffraction at DELTA

Louis Frentzel-Beyme, Pascal Kolodzeiski, Roman Pallach, Sebastian Henke*

Anorganische Chemie – TU Dortmund, Otto-Hahn-Str. 6, 44227 Dortmund

Scientific context

Metal-organic frameworks (MOFs) are an emerging class of porous solid state materials.[1,2] These materials have been proposed for several applications ranging from gas storage or separation to catalysis. So far, investigations have been predominantly focussed on the synthesis of new materials with novel or optimized properties.[3,4] Less research has been performed to investigate their fundamental properties regarding the materials' structural behaviour towards temperature or mechanical pressure. Nevertheless, especially those properties are highly important if it comes to industrial applications.

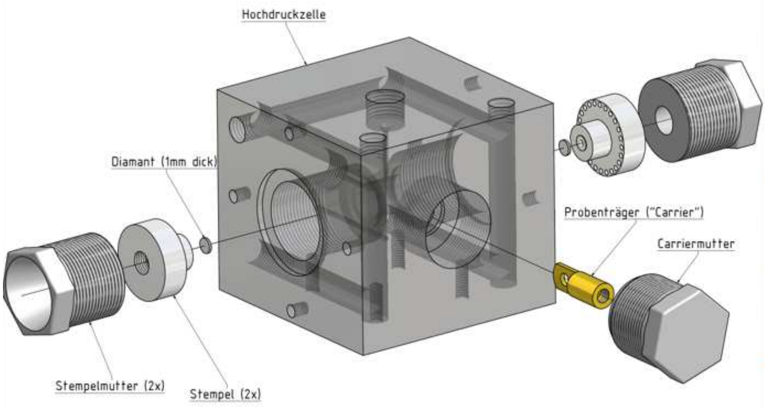

Fig. 1. Sketch of the sample cell developed at DELTA for X-ray reflectivity measurements under mechanical pressure.

Just recently, large changes in the compressibility of zirconium-based MOFs as function of the concentration of so-called "missing-linker" defects were observed with the help of high-pressure powder X-ray diffraction (HP-PXRD).[5] For flexible zeolitic imidazolate frameworks (ZIFs), a subset of MOFs, dramatic open pore to closed pore phase transitions have been discovered and it was even possible to map entire p/T phase diagrams on the basis of temperature dependent HP-PXRD data.[6–8] Given these first exciting results, we expect a lot more interesting phenomena to be discovered in the area of MOF mechanics via HP-PXRD.

A few years ago, a set-up for in-situ X-ray reflectivity measurements under variable hydrostatic pressure has been developed at Beamline 9 (BL9) of DELTA (see Fig. 1).[9] This set-up utilizes water as the pressure transmitting fluid (PTF) to allow investigations in a pressure range from 1 – 4000 bar. These pressures are relatively low, when compared to the pressures achieved in diamond anvil cells (DACs), the standard sample environment for HP-PXRD. However, for the relatively soft and flexible MOF materials, these lower pressure range is ideally suited. It is further important that the pressure can be adjusted precisely with an excellent pressure resolution (Δp = 25 - 50 bar) due to the manual hydraulic pressure system. The goal of the current work was to utilize and test this high-pressure X-ray reflectivity cell for HP-PXRD experiments. The opening angle of the beam outlet of the cell is ~30°. Hence, by using a photon energy of 27 keV (the maximum for BL9), we can cover a Q range up to ~3.6 Å^{-1}, sufficient for the determination of unit cell parameters and study of the compressibility of the materials in question.

Modified experimental set-up and aims

During our beamtime, we firstly aimed on modifying and testing the existing set-up to make HP-PXRD possible at BL9 of DELTA. Therefore, the sample powder was filled in a Kapton capillary (1.0 mm diameter Kapton tube, bottom sealed with superglue) and silicon oil was added to the capillary as a PTF in order to fully transmit the applied water pressure on the powder sample. At last, the capillary was sealed with a metal cap to prevent the sample from direct water contact (see Fig. 2, left). The capillary is then fixed in a modified "Carrier" (see Fig. 2, right) and the sample containing "Carrier" subsequently mounted in the high-pressure set-up (see Fig. 1, the "Carrier" is displayed in yellow).

The intention of these first experiments was to bring the proof-of-concept and to improve the set-up in terms of data quality. Further calibration measurements must be conducted in upcoming beamtimes to verify the set-up's functionality.

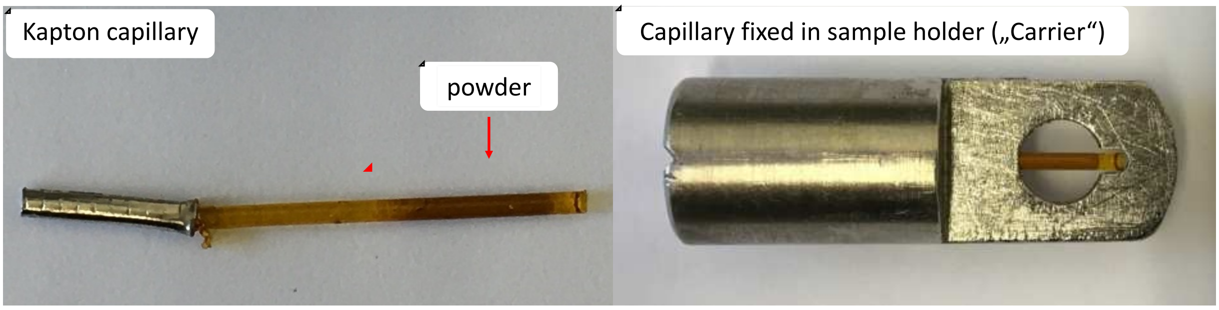

Fig. 2. Photographs of a filled Kapton capillary (left) and a filled Kapton capillary fixed in the modified sample holder (right).

Results

Firstly, we optimized the sample preparation, which made a reproducible mounting and PXRD data collection of powder samples possible. Beam and detector (MAR345) distance optimization helped to improve the data quality to obtain data with good signal to noise ratio and good angular resolution. Then, we collected the first set of reference data. For this purpose, we mixed lanthanum hexaboride (LaB_6) and aluminium (Al) in a 1:2 ratio (by weight) and filled it in a Kapton capillary (together with silicon oil as PTF).

The experimental PXRD data recorded in the pressure range from 1 – 3800 bar show a small shift of the Bragg reflections corresponding to Al upon increasing pressure (see Fig. 3a). We conclude that the applied hydrostatic water pressure is indeed transmitted on the powder sample in the Kapton capillary. Reflections corresponding to LaB_6 only barely shift, es expected because of its much higher bulk modulus ($K_0(LaB_6) \sim 176$ GPa, $K_0(Al) \sim 72$ GPa). Sequential dual phase profile fits with the software package TOPAS academic v6 were performed in order to precisely determine the zero offset (i.e. changes in sample to detector distance due to capillary displacement). Secondly, the evolution of the unit cell volume of Al as a function of the water pressure should be used to determine the offset of the 'real' pressure in the capillary to the applied pressure. We found that the unit cell volume of Al nearly linearly decreases as expected for these rather low hydrostatic pressures (see Fig. 3b). Unfortunately, inserting the obtained data into a reported equation of state for Al[10] yielded systematically higher 'real' pressures compared to the applied water pressures. This offset can be explained by the low accuracy of literature data for the low-pressure range of interest here, but also by the still relatively high bulk modulus of Al, which results in only small peak shifts and therefore quite large uncertainties. Next time, we will conduct further calibration measurements with much softer materials such as sodium chloride ($K_0(NaCl) \sim 25$ GPa) and potassium bromide ($K_0(KBr) \sim$

15 GPa). A much larger shift of the Bragg peaks will be observed for these alkali salts, which should allow us to perform a proper pressure calibration of the set-up.

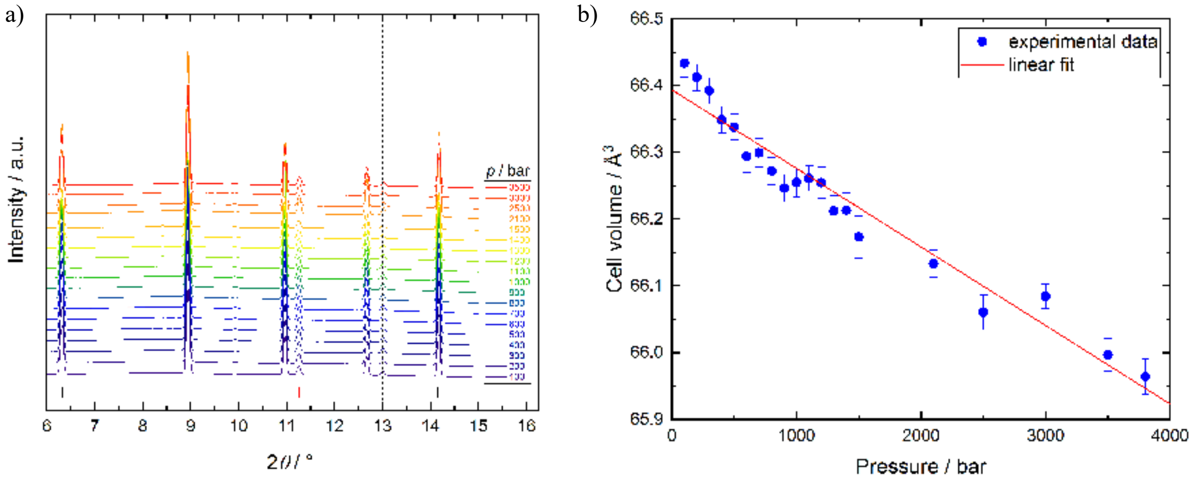

Fig. 3. a) PXRD patterns at variable pressures of the calibration measurement (calibrant LaB_6:Al (1:2)). Black and red tick marks indicate the allowed Bragg reflections for LaB_6 and Al, respectively. b) Plot of the unit cell volumes of Al against pressure obtained from profile fitting of the powder diffraction data shown in panel a).

Nevertheless, preliminary PXRD experiments with the prototypical MOF material Zn_2(dobdc) (aka MOF-74(Zn), dobdc^{4-} = 2,5-dioxido-1,4-benzenedicarboxylate) already show that good quality pressure dependent PXRD patterns can be collected even for such a low-density MOF material with the above described set-up (see Fig. 4). Shifts of the reflections to higher Bragg angles with increasing pressure are clearly obvious for these data. Hence, determination of the bulk modulus of these important MOF compound should be straight forward after successful pressure calibration of the set-up.

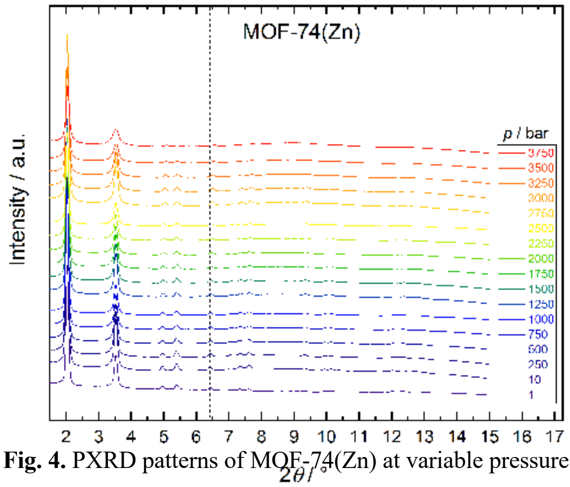

Fig. 4. PXRD patterns of MOF-74(Zn) at variable pressures.

In conclusion, we demonstrated that high-pressure powder X-ray diffraction can be performed at DELTA using a previously build X-ray reflectivity set-up after minor modifications. Diffraction patterns in a quality sufficient for profile analysis (extraction of unit cell parameters) are achievable. More time has to be invested, in order to perform a proper calibration of the applied pressure vs. the ‘real’ pressure. This, as well as a complete study of the high-pressure behaviour of a series of isoreticular MOF-74(M) materials (with $M^{2+} = Mg^{2+}, Co^{2+}, Ni^{2+}, Cu^{2+}, Zn^{2+}$), will be done in an upcoming beamtime in December 2019 (Beamtime ID: 66).

The authors thank the DELTA team for the possibility to modify their high-pressure X-ray reflectivity set-up and the beamline scientists of BL9, Dr. C. Sternemann and Dr. M. Paulus, for their outstanding support during the experiments and fruitful discussions about set-up optimization.

References

[1] B. Li, H. M. Wen, Y. Cui, W. Zhou, G. Qian, B. Chen, *Adv. Mater.* **2016**, *28*, 8819–

8860.

[2] S. Yuan, L. Feng, K. Wang, J. Pang, M. Bosch, C. Lollar, Y. Sun, J. Qin, X. Yang, P. Zhang, et al., *Adv. Mater.* **2018**, *30*, 1–35.

[3] O. M. Yaghi, *J. Am. Chem. Soc.* **2016**, *138*, 15507–15509.

[4] U. Mueller, M. Schubert, F. Teich, H. Puetter, K. Schierle-Arndt, J. Pastré, *J. Mater. Chem.* **2006**, *16*, 626–636.

[5] S. Dissegna, K. Epp, W. R. Heinz, G. Kieslich, R. A. Fischer, *Adv. Mater.* **2018**, *30*, 1–23.

[6] R. N. Widmer, G. I. Lampronti, S. Anzellini, R. Gaillac, S. Farsang, C. Zhou, A. M. Belenguer, C. W. Wilson, H. Palmer, A. K. Kleppe, et al., *Nat. Mater.* **2019**, *18*, 370–376.

[7] S. Henke, M. T. Wharmby, G. Kieslich, I. Hante, A. Schneemann, Y. Wu, D. Daisenberger, T. Cheetham, *Chem. Sci.* **2018**, *9*, 1654–1660.

[8] R. N. Widmer, G. I. Lampronti, S. Chibani, C. W. Wilson, S. Anzellini, S. Farsang, A. K. Kleppe, N. P. M. Casati, S. G. Macleod, S. A. T. Redfern, et al., *J. Am. Chem. Soc.* **2019**, *141*, 9330–9337.

[9] F. J. Wirkert, M. Paulus, J. Nase, J. Möller, S. Kujawski, C. Sternemann, M. Tolan, *J. Synchrotron Rad.* **2014**, *21*, 76–81.

[10] K. Syassen, W. B. Holzapfel, *J. Appl. Phys.* **1978**, *49*, 4427–4430.

Soft X-ray Spectroscopy

Investigation of thin boron layers on silicon (PureB) by means of x-ray photoelectronspectroscopy (XPS)

A.S. Burkowitz[1,2,*], **M. Schmitz**[1,2], **L. Kesper**[1,2], **U. Berges**[1,2],
S. Dreiner[3], **D. Weier**[3], **L.K. Nanver**[4] **and C. Westphal**[1,2]

[1] Experimentelle Physik I - Technische Universität Dortmund, Otto-Hahn-Str. 4a, D-44221 Dortmund
[2] DELTA - Technische Universität Dortmund, Maria-Goeppert-Mayer-Str. 2, D-44221 Dortmund
[3] Fraunhofer-Institut für Mikroelektronische Schaltungen und Systeme IMS, Finkenstr. 61, D-47057 Duisburg
[4] Universität Twente, Drienerlolaan 5, 7522 NB Enschede, Niederlande
[*] corresponding author: annika.burkowitz@tu-dortmund.de

We present an investigation of thin pure boron layers (PureB) on silicon. PureB systems yield excellent results regarding detection of ultraviolet light [1, 2] and low-energy electrons [2, 3]. The required extremly shallow pn-junctions can be provided by applying a few nanometers thick boron layer to ultra-pure silicon substrate wafers [4]. Detectors using the PureB technology show a near-theoretical sensitivity and a good robustness [1, 2, 5] as well as an exceptionally low leakage current [6].
The aim of this research is to analyze the interface between the silicon substrate and the boron adsorbate by means of x-ray photelectron spectroscopy (XPS). XPS studies reveal information about chemical bonding types present in the boron layer and about the composition of the surface.

The samples were kindly provided by Prof. Dr. Lis Nanver[4] and the research group of Dr. Stefan Dreiner[3]. The studied samples have varying boron layer thicknesses between 3 nm and 4 nm.

Figure 1a shows exemplarily an XPS-survey of the sample with a boron layer thickness of 3.4 nm at the polar angle $\Theta = 0°$ using a photon energy of $h\nu = 650\,\mathrm{eV}$. Five peaks are clearly visible at the kinetic energies $E_{\mathrm{kin}} = 118\,\mathrm{eV}, 366\,\mathrm{eV}, 462\,\mathrm{eV}, 500\,\mathrm{eV}$ and $550\,\mathrm{eV}$ that correspond to the core-level orbitals of the elements O 1s, C 1s, B 1s, Si 2s and Si 2p, respectively.

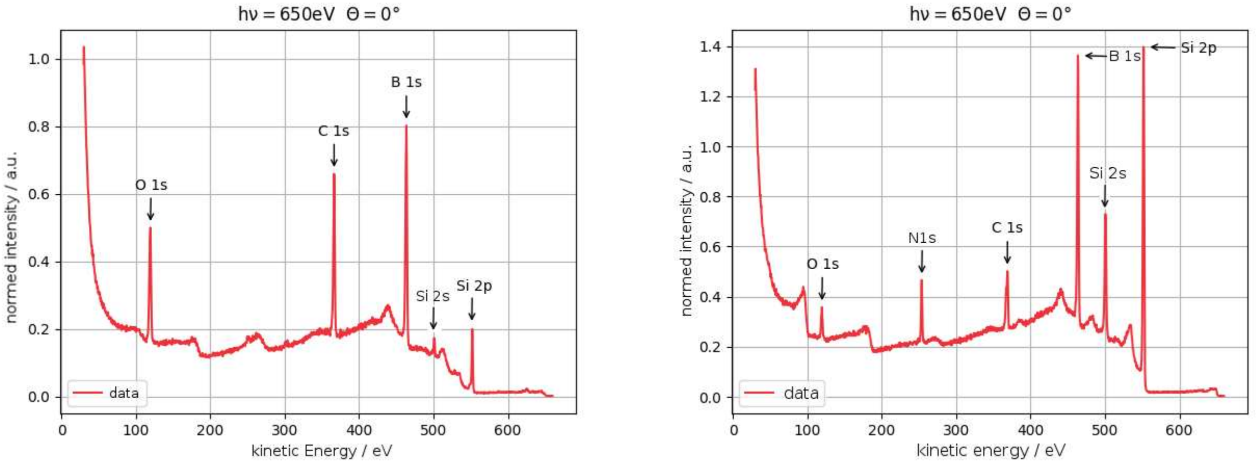

(a) Before annealing.

(b) After 12 min annealing at $T = 950\,°\mathrm{C}$.

Figure 1: Surveys of the sample with a boron layer thickness of 3.4 nm boron on silicon at $\Theta = 0°$.

Heating the sample to about 1000 °C reduces the oxygen and carbon contamination, but some contamination remains and a new peak appears at $E_{\mathrm{kin}} \approx 250\,\mathrm{eV}$. This new peak is an additional contamination that could be caused by nitrogen N 1s due to residual gas being present either during annealing or during the preparation of the sample. The survey of the heated sample can be seen in figure 1b.

High resolution XPS measurements were performed for the B 1s and the Si 2p core-level signals. In figure 2, the high resolution XPS spectrum of the B 1s orbital of the sample with a 3.4 nm thick boron layer at the polar angle of 0° is presented. In accordance with results by Xu et al. [7] and Ennaceur et al. [8], the spectrum was fitted with three Voigt-like components. These are B-B bonds at $E_{\text{kin}} \approx 68.5\,\text{eV}$, B-C bonds with a chemical shift of 0.6 eV and B-O bonds shifted by 1.4 eV. A B-Si componet was not seen, since the boron-silicon interface is buried beneath about 3 nm amorphous boron. Due to inelastic scattering of the photelectrons, the possibility to detect signal from the interface is low.

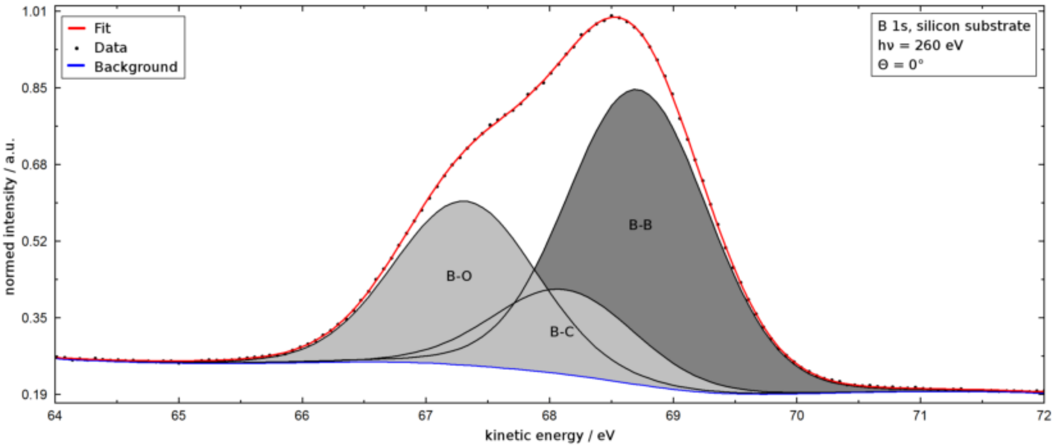

Figure 2: Fit of the hight resolution XPS spectrum of the sample with a boron layer thickness of 3.4 nm boron on silicon at $h\nu = 260\,\text{eV}$ and $\Theta = 0°$.

High resolution XPS spectra of samples after annealing show changes in the compontents that are present. The evaluation of these spectra is still going on, therfore no results regarding the fitted components are included in this report.

In oder to gain more knowlegde of the boron silicon interface, it is essential to repeat the high resolution XPS measurements with samples that have notably smaller boron layer thicknesses as well as less contamination. XPD studies could be useful in order to investigate the structure of the boron silicon interface.

References

[1] L. K. Nanver et al. “Robust UV/VUV/EUV PureB Photodiode Detector Technology With High CMOS Compatibility”. In: *IEEE Journal of Selected Topics in Quantum Electronics* 20.6 (2014).

[2] V. Mohammadi et al. “VUV/Low-Energy Electron Si Photodiodes With Postmetal 400 °C PureB Deposition”. In: *IEEE Electron Device Letters* 34.12 (2013).

[3] A. Sakic et al. “Versatile silicon photodiode detector technology for scanning electron microscopy with high-efficiency sub-5 keV electron detection”. In: *2010 International Electron Devices Meeting.* 2010.

[4] F. Sarubbi, T. L. M. Scholtes, and L. K. Nanver. “Chemical Vapor Deposition of α-Boron Layers on Silicon for Controlled Nanometer-Deep p+n Junction Formation”. In: *Journal of Electronic Materials* 39.2 (Feb. 2010).

[5] L. Shi et al. “Surface-Charge-Collection-Enhanced High-Sensitivity High-Stability Silicon Photodiodes for DUV and VUV Spectral Ranges”. In: *IEEE Transactions on Electron Devices* 59.11 (2012).

[6] L.K. Nanver et al. “Pure Dopant Deposition of B and Ga for Ultrashallow Junctions in Si-based Devices”. In: *ECS Transactions* 49 (Oct. 2012).

[7] Terry T. Xu et al. “Crystalline Boron Nanoribbons: Synthesis and Characterization”. In: *Nano Letters* 4.5 (2004).

[8] M.M Ennaceur and B Terreault. “XPS study of the process of oxygen gettering by thin films of PACVD boron”. In: *Journal of Nuclear Materials* 280.1 (2000).

Interaction effects of cathode power, bias voltage, and mid-frequency on the structural and mechanical properties of sputtered amorphous carbon films

Wolfgang Tillmann[1], Nelson Filipe Lopes Dias[1], Dominic Stangier[1], Manfred Bayer[2], Henning Moldenhauer[2], Jörg Debus[2], Marie Schmitz[3], Ulf Berges[3], Carsten Westphal[3]

[1]Institute of Materials Engineering, TU Dortmund University, 44227 Dortmund Germany
[2]Experimental Physics 2, TU Dortmund University, 44227 Dortmund Germany
[3]Experimental Physics 1, TU Dortmund University, 44227 Dortmund Germany

The Design of Experiments is a promising method to investigate the cause-effect relation between the mid-frequency magnetron sputtering parameters on the structural and mechanical properties of amorphous carbon (a-C) films. Based on the Central Composite Design, the cathode power of two graphite targets, bias voltage, and mid-frequency were simultaneously varied from 1500 to 4000 W, -100 to -200 V, and 20 to 50 kHz, respectively. The chemical bonding state was characterized using UV and visible Raman spectroscopy with excitation wavelengths of 266 and 532 nm. Corresponding measurements were performed by X-ray photoelectron spectroscopy (XPS) using synchrotron radiation. Additionally, hardness and elastic modulus of the sputtered a-C films were determined in nanoindentation tests.

Multi-wavelength Raman spectroscopy identified an sp^3 content below 20%, with most a-C films having an sp^3 value in the range of 12 to 18%. The formation of sp^3 bonded atoms is negatively influenced by a high cathode power and bias voltage, whereas the highest sp^3 content is obtained with a-C films sputtered with a cathode power and bias voltage of 2750 W and -150 V. However, higher values of the cathode power and bias voltage result in a film delamination and decrease of the sp^3 concentration. The bonding state affects the mechanical properties, as high hardness and elastic modulus result from a high sp^3 content. Therefore, a targeted adjustment of cathode power and bias voltage is necessary to obtain a-C films with a high hardness. In contrast, the mid-frequency does not have a significant impact on the mechanical properties. In conclusion, the Central Composite Design has proven to be a suitable method to investigate the cause-effects of the sputtering parameters on the properties of the a-C film.

Acknowledgments

The authors gratefully acknowledge the financial support of the German Research Foundation (DFG) within the project Ti 343/109-1. M. Bayer, H. Moldenhauer, and J. Debus acknowledge Toptica for providing the 266 nm TopWave laser. In addition, the authors thank the DELTA machine group for providing synchrotron radiation within BL11.

References

1. Wolfgang Tillmann, Nelson Filipe Lopes Dias, Dominic Stangier, Manfred Bayer, Henning Moldenhauer, Jörg Debus, Marie Schmitz, Ulf Berges, Carsten Westphal, *Interaction effects of cathode power, bias voltage, and mid-frequency on the structural and mechanical properties of sputtered amorphous carbon films*, In: Applied Surface Science 487 (2019) S. 857-867

XPS-/XPD-studies on the low-dimensional formation of self-assembled germanium on Ag(110)

L. Kesper[1,2,*], **C. Kohlmann**[1,2], **M. Schmitz**[1,2], **P. Roese**[1,2], **M. Schulte**[1,2], **U. Berges**[1,2], **and C. Westphal**[1,2]

[1] Experimentelle Physik I - Technische Universität Dortmund, Otto-Hahn-Str. 4a, D-44221 Dortmund
[2] DELTA - Technische Universität Dortmund, Maria-Goeppert-Mayer-Str. 2, D-44221 Dortmund
[*] corresponding author: lukas.kesper@tu-dortmund.de

Since the breakthrough of graphene in 2004 the novel field of two-dimensional materials in solid state physics has expanded massively. So-called Dirac-materials beyond graphene, like silicene and germanene, for instance, exhibit similar properties in a two-dimensional structure [1]. According to the report of the first synthesis of silicene [2], even one-dimensional silicon nanoribbons [3] were produced on different substrates. While growing epitaxially thin layers of silicon on Ag(111) silicene can be formed, the same approach of silicon on a Ag(110) substrate leads to one-dimensional silicon nanoribbons [4]. Withal, germanene impresses enormously by its stronger buckling and spin-orbit coupling, that might attain the observation of the quantum spin Hall effect [5]. In addition to its tunable bandgap outside the magnitude of room temperature excitation germanene is predestined for the realization of topological field effect transistors. [6] Here we report on a structural investigation of low-dimensional germanium on Ag(110) using photoelectron spectroscopy (XPS) and photoelectron diffraction (XPD).

The surface of the silver sample is prepared by several cycles of Argon-ion sputtering with $E_{\mathrm{Ar+}} = 800\,\mathrm{eV}$ and annealing to 720 K. All preparation and measurement steps are performed in an ultra-high vacuum chamber at beamline 11 with a base pressure of $p = 1 \times 10^{-10}$ mbar. The cleanness and reconstruction of the surface is checked by LEED measurements, shown in figure 1a). The vectors $\vec{a}$ and $\vec{b}$ represent the reciprocal basis vectors of the (1×1) reconstruction.

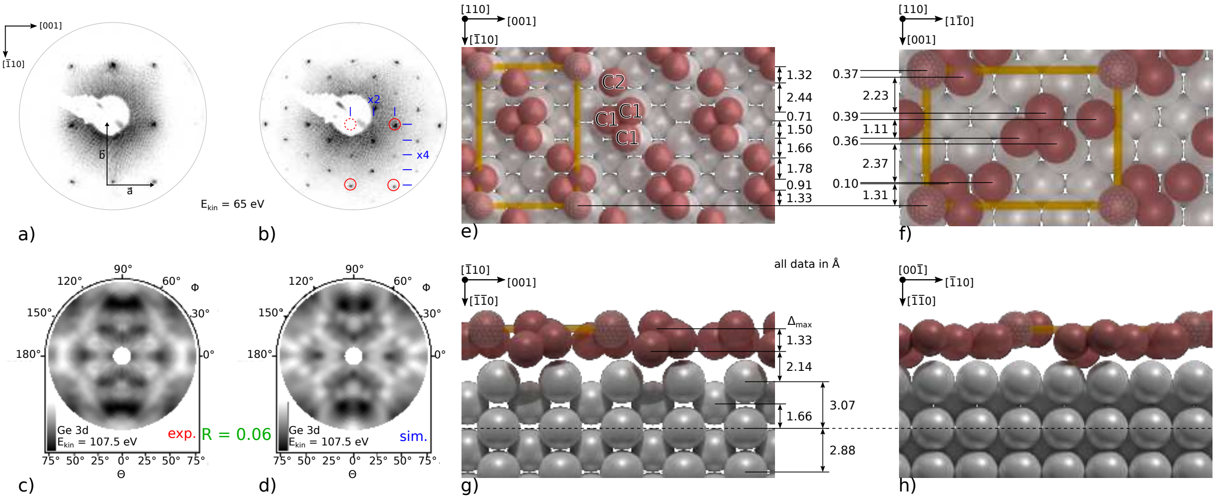

Figure 1: LEED pattern, recorded at a kinetic energy of $E_{\mathrm{kin}} = 65\,\mathrm{eV}$, of a clean Ag(110) sample a) and after the deposition of 0.7 ML germanium b). The measured XPD-pattern c) of Ge $3d$ signal, excited by h$\nu = 140\,\mathrm{eV}$, and the simulated pattern d) exhibit a consistency with an R-factor of R = 0.06. The simulation determines the structure shown in e)-h).

XPS-spectra in high energy resolution are used to study the bonding structure of the emitting atoms. Figure 2a) shows the 6 eV spin-orbit splitted Ag $3d$ signal, fitted by only one Voigt-like component and a Shirley-background. Features of surface plasmons appear next to the Ag $3d$ signals showing an increase of intensity for higher polar angle. Surface plasmons are indicators for well prepared surfaces preparation.

Using an electron-beam evaporator 0.7 ML of germanium can be grown epitaxially on the slightly heated Ag(110) surface. The self-assembled superstructure of the germanium reveals a $c(4{\times}2)$ periodicity, which can be observed in the LEED-pattern shown in figure 1b). Based on the XPS-analysis the germanium layer thickness can be determined, which agrees with micro quartz balance measurements, as well as with outcomes from literature [7]. Again high resolution XPS-spectra of the Ag $3d$ signal are performed after the deposition of 0.7 ML germanium, shown in figure 2b). Comparing these spectra to the clean sample, shown in figure 2a), no change in peak shape is noticeable. The germanium thin film is chemically isolated from the silver substrate. Moreover XPS-spectra in high resolution of the Ge $3d$ signal, shown in figure 2c), is recorded at a photon energy of hν = 140 eV. Due to the spin-orbit coupling the peak is splitted by $E_{\mathrm{SOC}} = 0.56\,\mathrm{eV}$ and it reveals two different chemical environments in terms of two components, shifted by $E_{\mathrm{chem}} = 0.19\,\mathrm{eV}$. Concerning various polar angles no surface effects can be observed, which displays the common behaviour of 2D-materials.

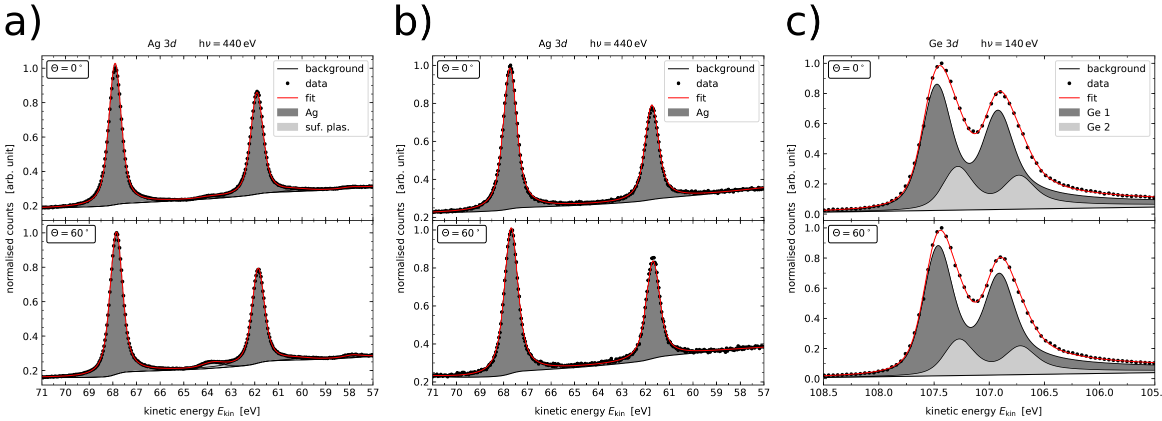

Figure 2: High resolution XPS-measurement, recorded at polar angles of $\Theta = 0°$ and $\Theta = 60°$. a) Ag $3d$ orbital of the clean Ag-sample with an excitation energy of $h\nu = 440\,\mathrm{eV}$. b) Ag $3d$ orbital after the deposition of 0.7 ML germanium. c) Ge $3d$ orbital of the same Ge/Ag-system with an excitation energy of $h\nu = 140\,\mathrm{eV}$.

Figure 1c) shows the experimental diffraction pattern yielded by XPD-measurements of the Ge $3d$ signal. The emitted photoelectrons with kinetic energies of $E_{\mathrm{kin}} = 107.5\,\mathrm{eV}$ interfere constructively and destructively resulting in diffraction pattern. Using the *EDAC* simulation-package combined with a genetic algorithm the pattern, shown in figure 1d) can be simulated. The consistency of the experimental XPD pattern and the simulation is judged by a R-factor of R = 0.06. The simulation determines the structure of low-dimensional germanium on Ag(110), displayed in figure 1e)-h). The chemical isolation of substrate and adsorbate, as well as the presence of two different chemical environments, marked by C1 and C2 in figure 1e), has been proven.

References

[1] M. Ezawa *et al.*, La Rivista del Nuovo Cimento **41**, 175 (2018).

[2] P. Vogt *et al.*, Physical Review Letters **108**, 155501 (2012).

[3] C. Leandri *et al.*, Surface Science **574**, L9 (2005).

[4] G. Prévot *et al.*, Physical Review Letters **117**, 276102 (2016).

[5] C.-C. Liu *et al.*, Physical Review Letters **107**, 076802 (2011).

[6] A. Molle *et al.*, Nature materials **16**, 163 (2017).

[7] C. Leandri *et al.*, Surface Science **573**, L369 (2004).

X-ray Scattering

DELTA user report 2019

PECVD Ti-Si-B-C-N nanocomposite coatings for tribological high temperature applications

Alexander Nienhaus

IOT TU Braunschweig

Field office DOC Dortmund

Eberhardstr. 12

44145 Dortmund

a.nienhaus@tu-bs.de

Phone: 0213 / 844 - 3937

Abstract

With increasing demand for longer service lifetimes of tools in hot forming applications, e.g. extrusion molding, surface modifications of hot working steels play an important role to improve the tribological properties under thermal load conditions. Especially the machining of copper and brass is challenging, considering their tendency to stick at the tool surface, which is increasingly problematic at machining temperatures up to 1000 °C. Nanocomposite coatings of the transition metal Titanium are an alternative to often-used Al_2O_3 coatings. Ti-Si-B-C-N is such a coating system with Ti(N,C) grains of nanometer size (3-10 nm), embedded in an amorphous matrix. These coatings show promising results regarding mechanical properties, like hardness and fracture toughness, and thermal stability and oxidation resistance.

State of the Art

The Ti-Si-N coating system a quasi-binary coating of nanocrystalline nc-TiN embedded in an amorphous a-SiN_x matrix (Zhang et al. 2004). The Ti-Si-N coating system shows high thermal stability, because of the dense structure of a-SiN_x and strong interface bonds between a-SiN_x and TiN, thus hindering oxygen diffusion along the TiN grain boundaries (Veprek et al. 2005). Si-based nitrides or oxides are immiscible with titanium ones, so a-SiN_x hinders the growth of TiO_2 grains, slowing down the oxidization process (Pilloud et al. 2008). On the base of these results, Ma et. al. (Ma et al. 2007) synthesized Ti-Si-C-N with a carbon for a better wear resistance and lower coefficients of friction (CoF). The Ti-Si-B-C-N coating system has not been part of the extensive research on nanocomposite coatings, yet. Park et. al. (Park et al. 2007) showed promising results comparing Ti-B-C-N and Ti-Si-B-C-N coatings in wear test applications, reducing the coefficient of friction by half.

Experimental Details

Ti-Si-B-C-N coatings were deposited on AISI H11 and AISI H13 tool steel substrates with a Ruebig PECVD device. Plasma etching, plasma nitriding and PECVD coating deposition are the three steps carried out in the vacuum process. The deposition details are given in Table 1.

Table 1: Process details for coating deposition

Auxiliary Gases and Precursor						Voltage	Temperature	Duration	Pressure
H_2	Ar	$TiCl_4$	BCl_3	$Si(CH_3)_4$	N_2	480-600 V	520-530 °C	6-8 h	200-240 Pa

The coatings were characterized by Electron Probe Micro Analysis (EPMA), Nanoindenation and in-situ X-Ray Diffraction (XRD) at elevated temperatures. The XRD investigations were carried-out at DELTA TU Dortmund, Beamline 9.

Results

Out of many deposited coating systems, the one with the lowest impurities and best mechanical properties is given in table 2.

Table 2: chemical composition, hardness and Young's modulus of a Ti-Si-B-C-N coating

Coating elements [at.-%]					**Impurities [at.-%]**		**Hardness**	**Young's modulus**
Ti	**Si**	**B**	**C**	**N**	**O**	**Cl**		
32.0	9.3	17.5	33.0	4.4	1.4	2.3	31.3 ± 2.6 GPa	250.9 ± 6.5 GPa

The diffraction patterns of TiN, Ti-B-N, Ti-B-C-N and Ti-Si-B-C-N under a thermal load of 750 °C are given in Fig. 1 a. The Si-containing Ti-Si-B-C-N coating is the only one that shows no signs of oxidation. TiN, Ti-B-N and Ti-Si-B-C-N show TiO_2 phases marked with lines and Δ. The five different characteristic TiO_2 reflexes clearly indicate heavy oxidation in all three films. The Ti-B-N coating is missing a sharp TiN reflex, indicating that many nc-TiN grains were converted into TiO_2. In contrast, the Ti-Si-B-C-N coating is not only stable up to 750 °C (see Fig. 1 a), but even up to 800 °C (see Fig. 1 b). At 900 °C, the Ti-Si-B-C-N coating shows heavy oxidation, leading to the conclusion that the oxidation resistance is given between 800 – 900 °C.

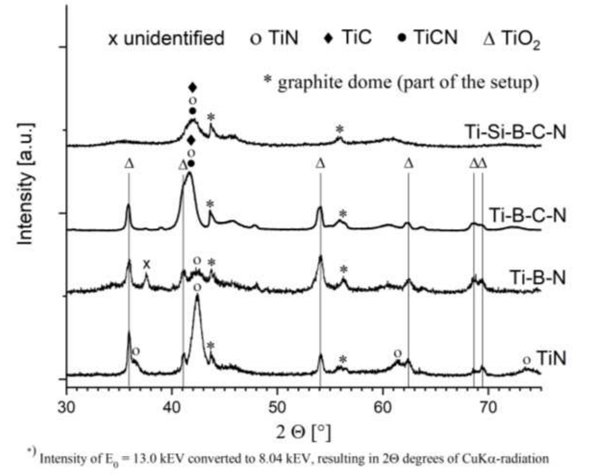

Fig. 1 a: XRD diffraction patterns at 750 °C of TiN, Ti-B-N, Ti-B-C-N and Ti-Si-B-C-N

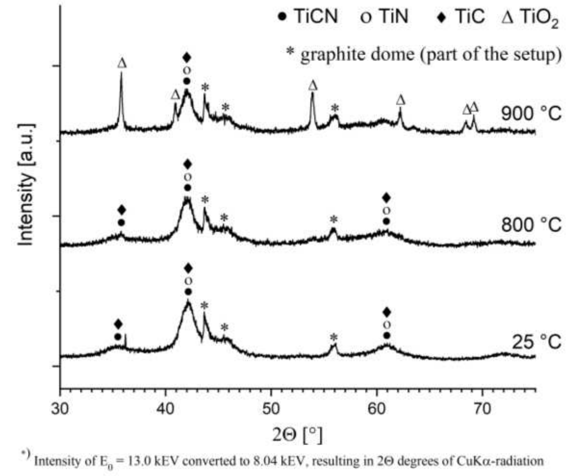

Fig. 1 b: XRD diffraction patterns of Ti-Si-B-C-N at 25 °C, 800 °C and 900 °C

Conclusions

- Coatings with even lower impurities and higher N-content could show higher hardness (>40 GPa) and higher oxidation resistance.
- The Si-containing Ti-Si-B-C-N coating is the only investigated coating with a thermal stability and oxidation resistance above 750 °C.
- Further work should focus on the gap between intact coating at 800 °C and oxidized coating at 900 °C.

Literature

Ma, S. L.; Ma, D. Y.; Guo, Y.; Xu, B.; Wu, G. Z.; Xu, K. W.; Chu, Paul K. (2007): Synthesis and characterization of super hard, self-lubricating Ti–Si–C–N nanocomposite coatings. In: *Acta Materialia* 55 (18), S. 6350–6355. DOI: 10.1016/j.actamat.2007.07.046.

Park, In Wook; Mishra, Brajendra; Kim, Kwang Ho; Moore, John J. (2007): Multifunctional Ti-Si-B-C-N Tribological Nanocomposite Coatings for Aerospace Applications. In: *MSF* 539-543, S. 173–180. DOI: 10.4028/www.scientific.net/MSF.539-543.173.

Pilloud, D.; Pierson, J. F.; Marco de Lucas, M. C.; Cavaleiro, A. (2008): Study of the structural changes induced by air oxidation in Ti–Si–N hard coatings. In: *Surface and Coatings Technology* 202 (11), S. 2413–2417. DOI: 10.1016/j.surfcoat.2007.09.017.

Veprek, Stan; Veprek-Heijman, Maritza G.J.; Karvankova, Pavla; Prochazka, Jan (2005): Different approaches to superhard coatings and nanocomposites. In: *Thin Solid Films* 476 (1), S. 1–29. DOI: 10.1016/j.tsf.2004.10.053.

Zhang, Sam; Sun, Deen; Fu, Yongqing; Du, Hejun (2004): Effect of sputtering target power on microstructure and mechanical properties of nanocomposite nc-TiN/a-SiNx thin films. In: *Thin Solid Films* 447-448, S. 462–467. DOI: 10.1016/S0040-6090(03)01125-8.

Influence of bias potential on texture and thermal resilience of CrAl(Si)N coatings

Jan Latarius[1], Dominic Stangier[2], Kristina Berger[1], Juri Forov[1], Christopher Weis[1], Michael Paulus[1], Wolfgang Tillmann[2], and Metin Tolan[1]

[1]Fakultät Physik / DELTA, TU Dortmund, University, Germany 44221
[2]Institute of Materials Engineering, TU Dortmund, Germany 44227 Dortmund, Leonhard-Euler-Straße 2

Modern production is in need for efficient, high performance coatings to increase resilience against wear, fatigue and corrosion for tools and products [1]. Possible candidates are transition metal ceramics applied to the surface via physical vapor deposition (PVD). Our experiments employ X-ray diffraction (XRD) and CrAlSiN coatings applied to a WCCo substrate and corresponding CrAlN coatings as benchmark, as the latter has been previously examined, see Deng et al. [2], and the former is a possible candidate for succession due to positive influences of the incorporation of silicone, see Diserens et al. [3]. The coatings had a thickness of approximately 3 μm. In the course of the experiment at beamline 9, the samples were heated *ex-situ* from room temperature up to 1200 °C.

These samples experienced different bias potentials during the deposition process ranging from -80 to -200 V. As a result the higher impact energy at deposition presumably leads to varying conditions regarding stress/strain, crystallite size, texture and density within the coating. This impacts the microscopic structure and thus the gathered diffractograms.

The XRD setup employing the MAR345-detector has been used and the beam energy was set to 25 keV. Two different incident angles have been used: 0.5 ° and 5.0 °.

Looking at the caked diffractograms in figure 2, one can easily make out the speckled appearance of the (Cr, Al)N main Bragg reflection (200) in wurtzite conformation. This results from the relatively big domains of the WC η-phase in the substrate. For further processing these will need to be addressed to avoid alteration of the true (Cr, Al)N peak shape.

In addition to this the (Cr, Al)N phase appears to be increasingly textured towards the (200) orientation indicated by its symmetrical regions of higher intensities. This might be due to growth effects during the deposition process induced by the bias potential leading to big domains of similarly oriented crystallites, as was reported by Romero et al. [4].

Besides the main peak of the (Cr, Al)N phase only the (111) and the (220) feature are easily accessible, as can be seen in figure 1. Higher order reflections are vanishingly small compared to the WC reflexes with high intensities. Gathering information on these reflections is crucial in order to determine structural parameters of the coating.

These aforementioned impediments require further investigation via methods of image analysis to obtain detailed information on these coatings and to achieve deeper understanding of the influence of bias potential in the course of the deposition process.

Acknowledgment: We kindly acknowledge the support of the DELTA machine group and the provided synchrotron radiation.

References

[1] B Navinšek, P Panjan, and I Milošev. Industrial applications of CrN (PVD) coatings, deposited at high and low temperatures. *Surface and Coatings Technology*, 97(1):182 – 191, 1997.

[2] Jianxin Deng, Fengfang Wu, Yunsong Lian, Youqiang Xing, and Shipeng Li. Erosion wear of crn, tin, craln, and tialn pvd nitride coatings. *International Journal of Refractory Metals and Hard Materials*, 35:10 – 16, 2012.

[3] M Diserens, J Patscheider, and F Lévy. Improving the properties of titanium nitride by incorporation of silicon. *Surface and Coatings Technology*, 108-109:241 – 246, 1998.

[4] J. Romero, M.A. Gómez, J. Esteve, F. Montalà, L. Carreras, M. Grifol, and A. Lousa. Craln coatings deposited by cathodic arc evaporation at different substrate bias. *Thin Solid Films*, 515(1):113 – 117, 2006. International Conference On Surfaces, Coatings And Nanostructured Materials.

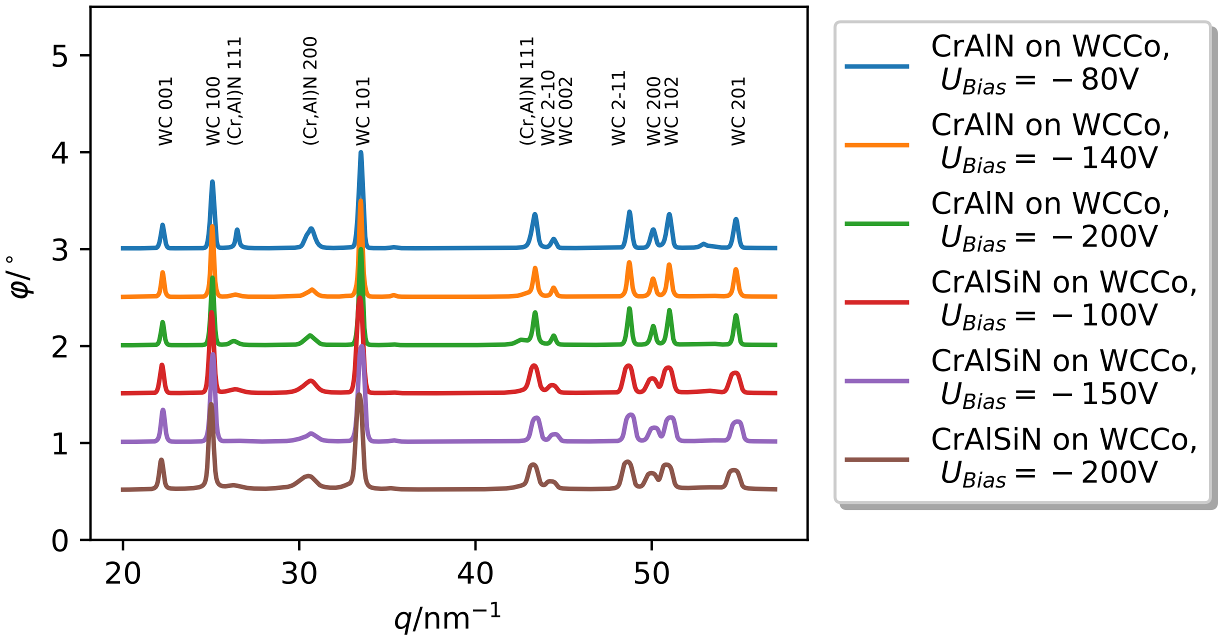

Figure 1: Overview over integrated diffractograms of CrAl(Si)N coatings on WCCo substrate produced with different bias potentials, taken at an incident angle of 5 °.

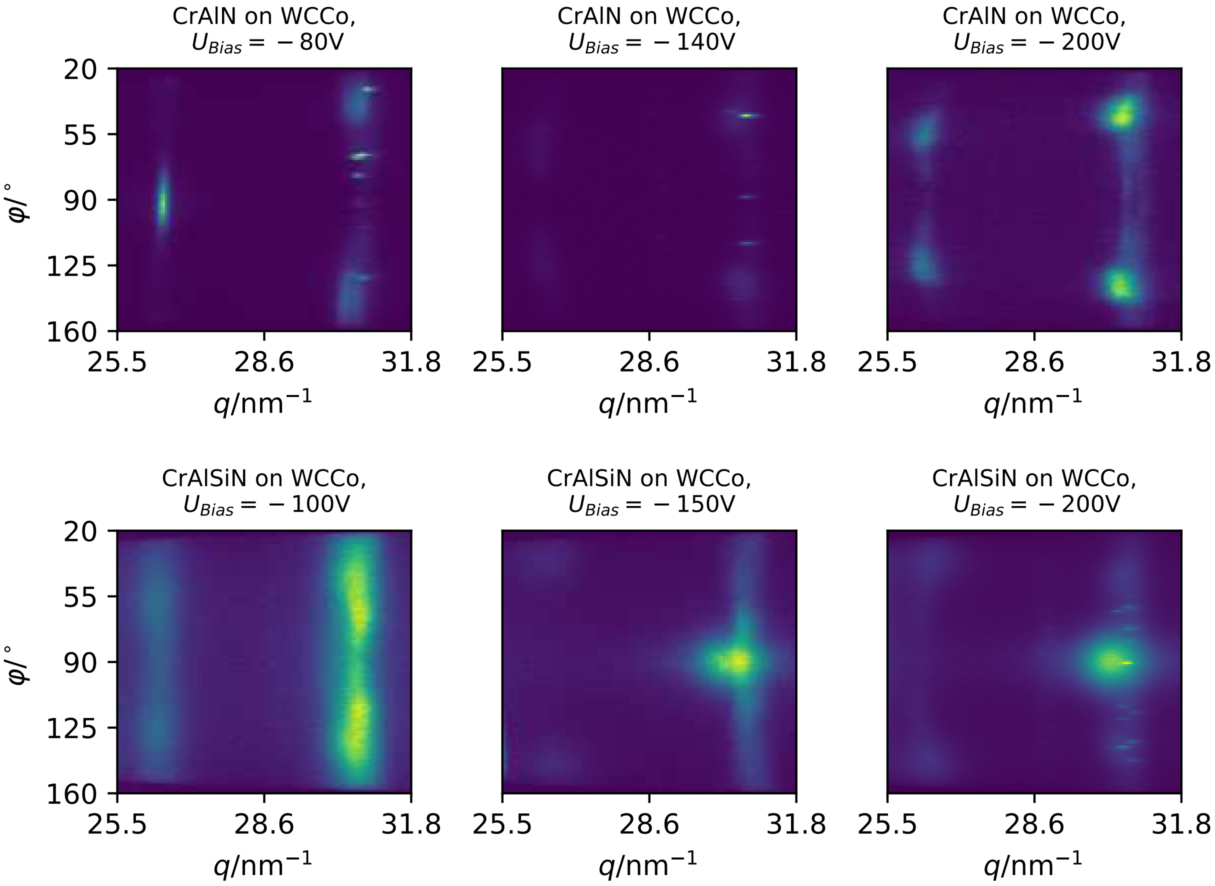

Figure 2: Sections of caked diffractograms of CrAl(Si)N coatings on WCCo substrate produced with different bias potentials, taken at an incident angle of 5 °. The sections contain the (Cr, Al)N (111) and (200) reflexes, as well speckles originating from WC η-phase.

Studying the feasibility of depositing alumina reinforced Sn-Sb-Cu based composite coatings by means of low pressure cold spraying

W. Tillmann[1], L. Hagen[1], M. Abdulgader[1], D. Kokalj[1], D. Stangier[1], M. Paulus[2], M. Tolan[2]

[1]Institute of Materials Engineering, TU Dortmund University, Germany
[2]Fakultät Physik / DELTA, TU Dortmund University, Germany

Introduction

Tin based Babbitt, also called white metal, represents a group of alloys that contain different grades based on Sn with the addition of Cu and Sb. The strength of the materials is substantially determined by the addition of Cu and Sb. Thus, the microstructure of conventional Sn-Sb-Cu-based Babbitt alloys mainly consists of SnSb and Cu_6Sn_5 intermetallic phases dispersed in a soft solid solution matrix [1]. Babbitt coatings are widely used in industrial bearings, serving as sacrificial surface. Nevertheless, sufficient hardness and load carrying capacity must be provided. The babbitting of bearing surfaces can be accomplished by casting, however, this implies some disadvantages. Thermal spraying represents a promising method to overcome these challenges. Although Sn-Sb-Cu-based feedstocks are widely available, to date no studies on Babbitt coatings deposited by means of low pressure cold spraying (LPCS) are available in the literature. Within this study, a first attempt is made to produce a Sn-Sb-Cu-based Babbitt composite coating by means of LPCS which enables the coating of internal diameters (IDs) of cylindrical components.

Experimental

A powder mixture which contains 84.0 wt.% of Sn, 8.0 wt.% of Sb and 8.0 wt.% of Cu served as feedstock. Afterward, the feedstock was mixed with alumina using a volumetric ratio of 80:20 to minimize the risk of nozzle-clogging during spraying. A round specimen made of C45 (1.0503) with a diameter of 40 mm and a thickness of 6 mm served as substrate. Prior to the coating deposition, the substrate was grit blasted and cleaned in an ultrasonic ethanol bath. The coating deposition was carried out using the DYMET 413 spraying system (Fa. Dycomet, Netherlands). The spray gun was equipped with an inhouse-made extension and modified nozzle attachment to enable the ID coating (Fig. 1). Due to the technical changes it is possible to coat cylindrical components with an ID of 140 mm. The spray gun was mounted on a three-axis CNC linear drive (Fa. Antriebtechnik Carl Rehfuss Albstadt, Germany). The spray parameters used within this study are listed in Table 1. The spraying experiments were conducted using compressed air. The phase composition was investigated by means of X-ray diffraction (XRD) at the beamline BL9 of the synchrotron light source DELTA (Dortmund, Germany). The photon energy was set to 25 keV ($\lambda = 0.496$ Å). A MAR345 image plate detector was used for photon detection. The beam size was set to 1.0 x 0.1 mm² and the angle of the incidence was 5°. The software MATCH! in conjunction with a reference database (i.e. Crystallography Open Database) was used to identify the phase composition. To assess the mechanical response of the produced alumina reinforced Sn-Sb-Cu based composite coating, Vickers microhardness measurements were carried out with a load of 2.49 N (300gf) using a Duramin-40 microhardness tester (Struers, Germany). A minimum of five indents were conducted for the microhardness measurement.

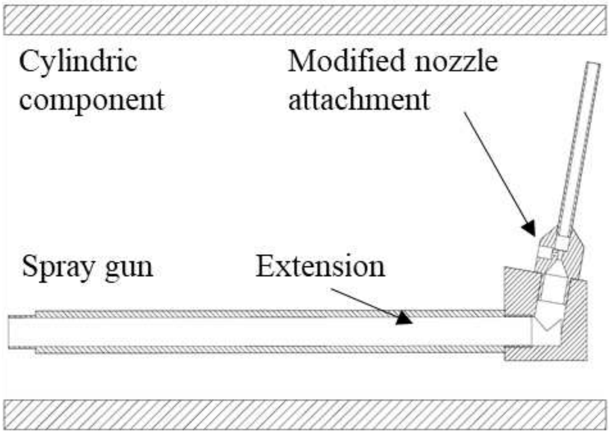

Fig. 1: Schematic drawing of the custom-made extension and nozzle attachment

Parameters	Value
Gas medium	Air
Gas temperature [°C]	~ 400
Gas pressure [bar]	5.0
Stand-off distance [mm]	10
Spray angle [°]	100
Transverse speed [mm/s]	100
Overruns [passes]	6

Table 1: Spray parameter settings

Results

First metallographic investigations reveal that the produced coating exhibits a dense microstructure, and good bonding to the substrate. Hence, cross-section analyses preclude the presence of macroscopic defects, evaluating the feasibility of a cost-saving method to deposit alumina reinforced Sn-Sb-Cu composite coatings by means of LPCS. The XRD analysis (Fig. 2) shows that the coating mainly consists of Sn, SnSb (rock-salt structure) and Cu. Interestingly, the XRD pattern does not show Bragg reflections for alumina. Furthermore, the XRD pattern indicates the absence of intermetallic compounds such as Cu_3Sn and Cu_6Sn_5 within the experimental resolution. The inset of Fig. 2 depicts parts of the two-dimensional diffraction patterns of the feedstock (left) and the coating (right). While on the left side a Debye-Scherrer ring of Sb (102) reflection is visible besides speckles caused by relatively large Sn crystals ((020), (011), (220), and (121) reflections), on the right side the Sb reflection is replaced by the reflection of SnSb ((200) and (202) reflection). The spackle pattern of Sn has changed to homogenous rings with a slight texture. Based on the findings, it can be assumed that large fractions of Sn crystals were melted during the coating process and recrystallized on the substrate yielding nearly an ideal, powder-like crystallite distribution. As opposed to that, the inhomogeneous intensity distribution for SnSb, as shown by the Debye-Scherrer rings, points to relatively large crystallites. In terms of the mechanical properties, Vickers microhardness measurement reveals a microhardness of 15.1±3.0 HV0.3 at the coating surface. Thus, the microhardness is found to be significantly lower compared to those obtained from Babbitt coatings deposited by conventional manufacturing techniques [2]. It is stated that the absence of Cu_3Sn and Cu_6Sn_5 causes the low microhardness. Instead, the formation of SnSb intermetallic phases dispersed in the soft Sn-Sb rich matrix predominantly determine the microhardness of the alumina reinforced Sn-Sb-Cu composite coating.

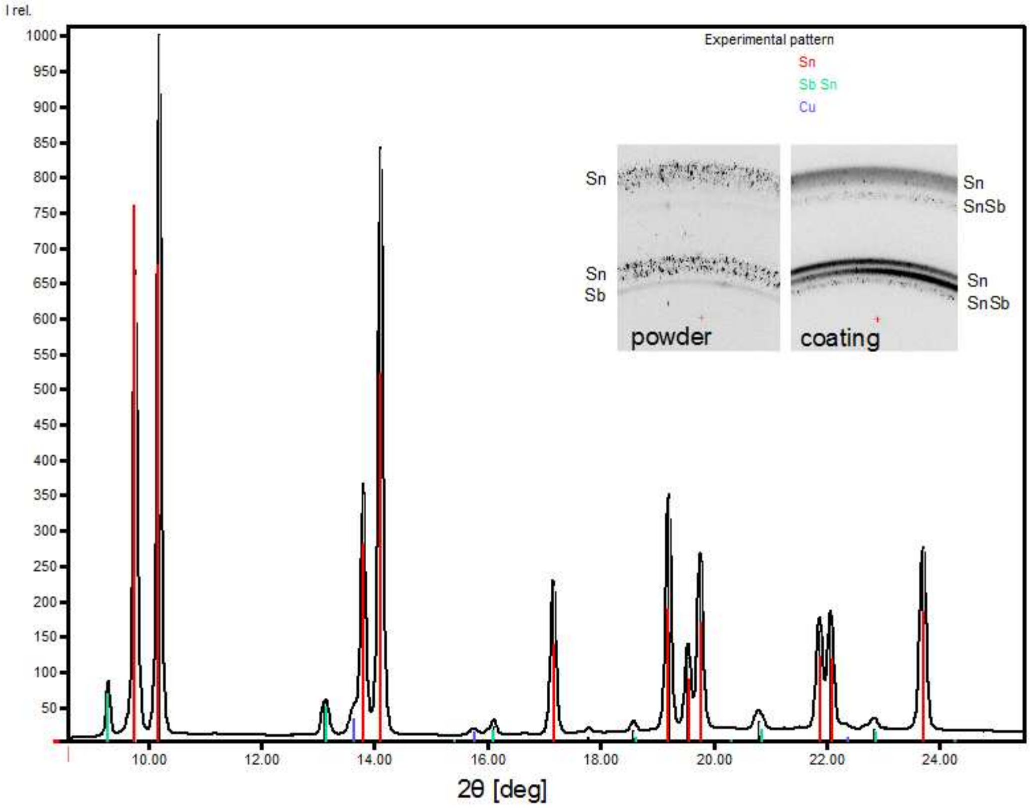

Fig. 2: XRD-patterns of the produced alumina reinforced Sn-Sb-Cu composite coating and starting powder mixture (feedstock)

Acknowledgement

The authors thank the DELTA machine group for providing the synchrotron radiation.

References

1. Nascimento, A. R. C., Ettouil, F. B., Moreau, C., Savoie, S., & Schulz, R. (2017). Production of Babbitt Coatings by High Velocity Oxygen Fuel (HVOF) Spraying. *Journal of Thermal Spray Technology*, *26*(7), 1732-1740.
2. Junior, P. R. C. A., & Pukasiewicz, A. G. M. (2019). Evaluation of microstructure, mechanical and tribological properties of a Babbitt alloy deposited by arc and flame spray processes. *Tribology International*, *131*, 148-157.

X-Ray diffraction on heat-treated metal foils

F. Eckelt, B. Bornmann, R. Wagner, D. Lützenkirchen-Hecht, R. Frahm

Fakultät 4-Physik, Bergische Universität Wuppertal, Gaußstr. 20, 42097 Wuppertal, Germany

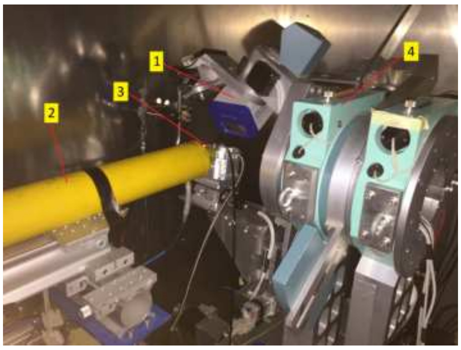

Figure 1: Rear end of Beamline BL10 with Pilatus detector (1), beam tube (heliumfilled) (2), DHS 1100 (3) and goniometer (4).

Within the scope of this work, diffraction images of different metals with different structures were to be measured during a heat treatment using a surface detector and X-rays from storage rings in order to experimentally capture possible texturing phenomena. The metal foils may already show texturing in their initial state due to the rolling process in the manufacturing process. The measurements were carried out on beamline 10 of the DELTA using the Si(111) monochromator. The metal foils were heated with a Anton Paar DHS 1100, which is a special heating device for X-ray diffractometry, allowing the samples to be heated up to 1100 °C. The diffraction images were recorded with a Pilatus 100K-S detector, which allows the entire diffraction image to be recorded simultaneously. Figure 1 shows the complete experimental setup, with which the samples to be examined can be measured in transmission. The detector and the heating chamber were attached to a goniometer so that they could be rotated in order to be able to record a large range of the diffraction pattern. With this geometry, concentric diffraction rings are formed on the detector by polycrystalline samples, which have an ideally homogeneous intensity distribution. A deviation from this indicates the presence of a texture. For the measurements, the samples are slowly heated and examined with a photon energy of $E_{\text{Photon}} = 16\,\text{keV}$, with 30 s exposure time per measurement.

For the analysis of the diffraction images, each diffraction ring is characterized by the inner and outer radius and a polar angle α is introduced, which is defined as in Figure 2.

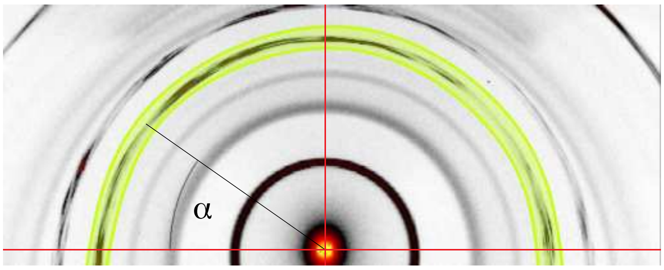

Figure 2: Example of the interesting range of a copper sample at room temperature.

For the analysis of the intensity distribution, the intensity is added up in 1 °- steps and plotted against the heating temperature and the polar angle. In addition, the total intensity of the recorded part of the diffraction ring was considered, for which the intensity of the entire ring was added up.

The following diagrams resulted for the {111} - reflection of an examined copper foil:

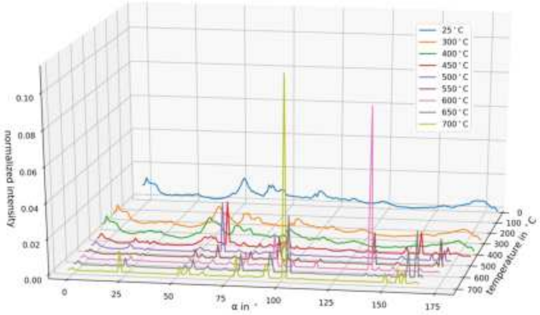

Figure 3: Intensity distribution of the {111} - diffraction ring of the copper sample plotted against the heater temperature

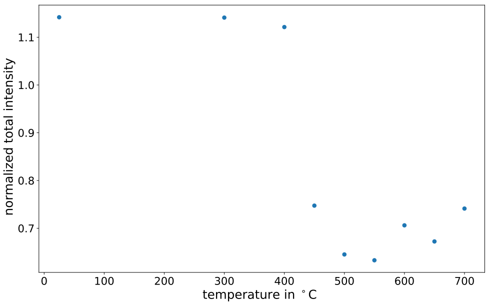

Figure 4: Total intensity of the {111} - diffraction ring of the copper sample applied against the heating temperature

It is easy to see that the radial intensity distribution is largely constant for low sample temperatures. From the exceeding of a material-dependent transition temperature, clear peaks are visible in the intensity distribution, which vary in intensity with increasing temperature. Also in the total intensity a change is visible after exceeding the transition temperature as the intensity decreases. This can be explained by the texturing of the sample. The same alignment of several grains results in sharp peaks with high intensity and larger areas that lose intensity. Since energy in the form of thermal energy is required for this process, this process only begins when a material-dependent transition temperature is exceeded.

The same measurements were performed on titanium and vanadium at DELTA and on silver and platinum at Petra III (DESY) in addition to copper. In Figure 5, the melting temperatures are plotted against the determined transition temperatures.

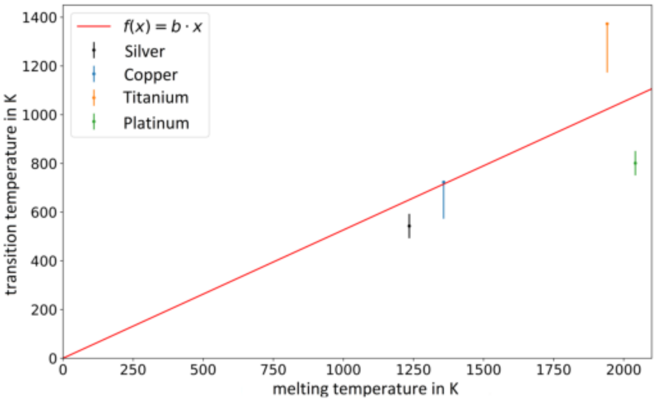

Figure 5: Melting temperature applied against the transition temperature with a linear fit.

A linear relationship between melting temperature and transition temperature is visible, with the transition temperature being about 52 % of the melting temperature.

Acknowledgements

We gratefully acknowledge the DELTA machine group for providing synchrotron radiation reliably.

Role of microstructure and surface morphology on charge carrier transport in organic semiconductor

Hanna Makowska[1], Mateusz Brzezinski[1], Okan Yildiz[2], Wojciech Pisula[1,2,*] and Tomasz Marszalek[1,2,*]

[1] Department of Molecular Physics, Faculty of Chemistry Lodz University of Technology, Zeromskiego 116, 90-924 Lodz (Poland)
[2] Max Planck Institute for Polymer Research, Ackermannweg 10, 55128 Mainz, Germany
* Email: marszalek @mpip-mainz.mpg.de, pisula@mpip-mainz.mpg.de

Semiconducting molecules show great potential for applications in organic field-effect transistors (OFETs) due to their advantages in lightweight, mechanical flexibility and solution processability compared with inorganic semiconductors. Their non-covalent molecular interactions result in the self-assembly into different functional superstructures over various length scales. The charge transport in these structures is determined by the molecular organization and thin film morphology so that the molecules need to be closely packed and highly long-range ordered in the conductive channel of a transistor. Solution processing, as the only possibility for thin film deposition of conjugated polymers, offers opportunities to affect the charge carrier mobility in OFET devices, because of its fine control over the semiconductor microstructure and molecular ordering that play a critical role in the charge carrier transport. Besides methods for solution processing, the solvent that is utilized to dissolve the conjugated polymer is another key element for the resultant film microstructure and subsequent device performance. From one hand, the control of polymer aggregation and surface orientation can be performed by solvent tuning. From the other hand, polymorphism of the aggregated phases of a low-bandgap conjugated polymer, can be additionally identified in solution and in the solid state.

During our beam time at the BL9 of the DELTA electron storage ring in Dortmund in 2018-2019 we performed investigations to efficiently tune the polymorphism of conjugated polymers in aggregated, semi-crystalline phases due to their conformational freedom and anisotropic nature. Two distinctly different semi-crystalline polymorphs (β1 and β2) of a low-bandgap diketopyrrolopyrrole polymer are formed through controlling the solvent quality, as evidenced by spectroscopic, structural, thermal and charge transport studies. Compared to β1, the β2 polymorph exhibits a lower optical band gap, an enhanced photoluminescence, a reduced π-stacking distance, a higher hole mobility in field-effect transistors and improved photocurrent generation in polymer solar cells. The β1 and β2 polymorphs provide insights into the control of polymer self-organization for plastic electronics and hold potential for developing programmable ink formulations for next-generation electronic devices.[1]

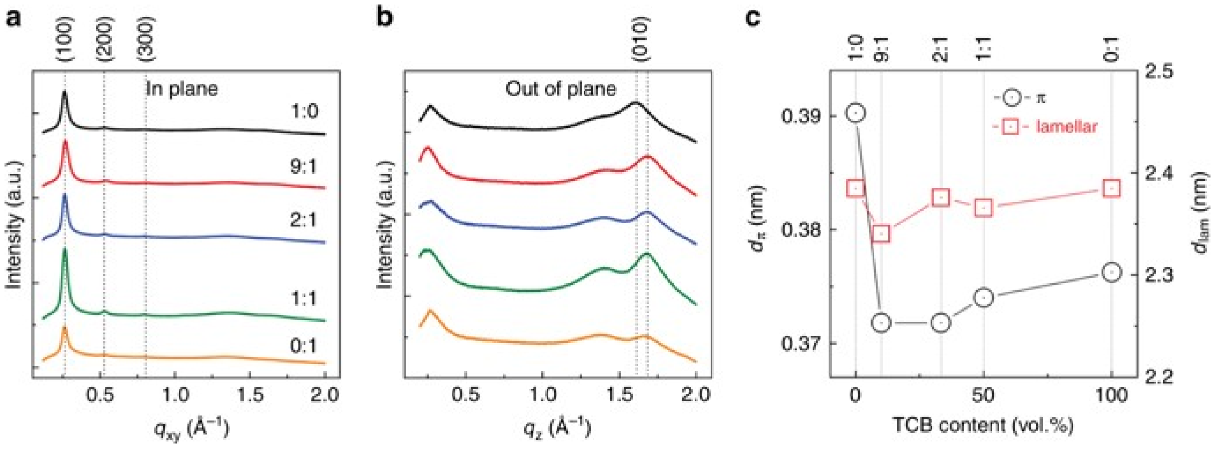

Figure 1. Grazing incidence wide-angle X-ray scattering (GIWAXS) of thin films. GIWAXS of D-PDPP4T-HD thin films cast from different chloroform:1,2,4- trichlorobenzene (CF:TCB) solutions. **a** In-plane profile. **b** Out-of-plane profile. **c** Lamellar spacing (d_{lam}) and π-stacking distance (d_π). Note that the scale in panel **c** is different for d_π and d_{lam} [Figure taken from ref. 1]

In parallel to the investigation for the high molecular weight semiconductor, the conductivity of poly(3,4-ethylenedioxythiophene):poly(styrene sulfonic acid) (PEDOT:PSS) was controlled by treatment with high boiling solvents as dimethyl sulfoxide (DMSO). The effect of various DMSO solvent treatment methods on the performance of organic electrochemical transistors (OECTs) based on PEDOT:PSS is studied. In OECT configuration, the PEDOT:PSS conductivity is typically reduced by one order of magnitude by incorporation of an electrolyte due to swelling effects. The proposed method gives rise to the highest transconductance and on/off ratio as compared to the typical method described in literature. The enhanced conductivity originates from an increased charge carrier mobility due to phase segregation in PEDOT:PSS-rich and PSS-rich domains and exhibit enhanced structural order.[2]

Acknowledgement

This work was partially prepared as part of the „*Self-standing, flexible and solution processable organic field effect transistors for complementary inverter applications*" project that is carried out within the First Team programme of the Foundation for Polish Science co-financed by the European Union under the European Regional Development Fund (*First TEAM/2017-3/26*). W.P. acknowledges the National Science Centre, Poland, through the grant UMO-2015/18/E/ST3/00322. The researchers involved in these projects express their gratitude to Dr. Christian Sternemann and Dr. Michael Paulus for their help in the experiments.

References

1) M. Li, A. H. Balawi, P. J. Leenaers, L. Ning, G. H. L. Heintges, **T. Marszalek**, **W. Pisula**, M. M. Wienk, S. C. J. Meskers, Y. Yi, F. Laquai & R. A. J. Janssen, "Impact of polymorphism on the optoelectronic properties of a low-bandgap semiconducting polymer", *Nature Communications*, **2019**, 10:2867.

2) L. V. Lingstedt, M. Ghittorelli, H. Lu, D. A. Koutsouras, **T. Marszalek**, F. Torricelli, N. Irina Cra˘ciun, P. Gkoupidenis, and P. W. M. Blom, "Effect of DMSO Solvent Treatments on the Performance of PEDOT:PSS Based Organic Electrochemical Transistors", *Adv. Electron.Mater.*, **2019**, 5, 1800804.

Supramolecular structure of n-octanol

Jennifer Bolle, Christian Sternemann, Michael Paulus, Christian Albers, Göran Surmeier, Susanne Dogan and Metin Tolan
Fakultät Physik/DELTA, Technische Universität Dortmund, 44221 Dortmund, Germany

Hydrogen bonds are important for the structure formation and dynamics of monohydroxy alcohols (MAs) and thus they are the key for the understanding of the microscopic structure of alcohols and alcohol/water mixtures [1]. The dominant structures formed by the MAs are intermolecular ring and chain arrangements. In this study we have examined n-octanol isomers (n=1,2,3,4) in order to understand the role of the position of the hydroxy group for structure formation. Stephenson et al. investigated pure n-octanol with MD simulations and discovered that straight chain and branched networks dominate in 1-octanol. If the OH group is placed further towards the center of the molecule, as with 3- and 4-octanol, the number of ring-like arrangements increases and the number of chains decreases. A dielectric study by Shinomiya et al. shows that the formation of rings and chains structures can be influenced by temperature variations [4]. This temperature induced structural change of octanol isomers was investigated by X-ray diffraction (XRD) at beamline BL9 of the synchrotron light source DELTA (TU Dortmund, Dortmund, Germany). The MAs 1-octanol (purity $\geq 99.7\,\%$), 2-octanol ($\geq 99.5\,\%$), 3-octanol ($\geq 99.5\,\%$) and 4-octanol ($\geq 97\,\%$) are provided from Sigma Aldrich and are used without further treatment. The MAs were filled in borosilacate capillaries with 2 mm and 3.5 mm diameter. A 700 Series Cryosteam Cooler adjusts the temperature of the capillary in 10K steps in a temperature range from 238 K to 377 K. The diffraction patterns of the measured samples can be seen in figure 1. These were recorded using a MAR345 image plate scanner at photon energies of 20 keV and 27 keV with a detector distance between 350 mm and 650 mm. These patterns exhibit two distinct peaks. The mainpeak at higher momentum transfer (q) is predominantly due to the carbon-carbon correlations in the liquid. The prepeak at lower q originates from formation of supramolecular arrangements with typical length scales larger than a single molecule. Its position reflects typical distances owing to oxygen-oxygen correlations. For a detailed analysis of the main- and prepeak a linear background was subtracted. Then the peak was fitted with a pearson VII-function. The prepeak analysis is shown in figure 2. For comparison the maximum positions, intensity and FWHM were normalized to the values determined at the highest temperature.

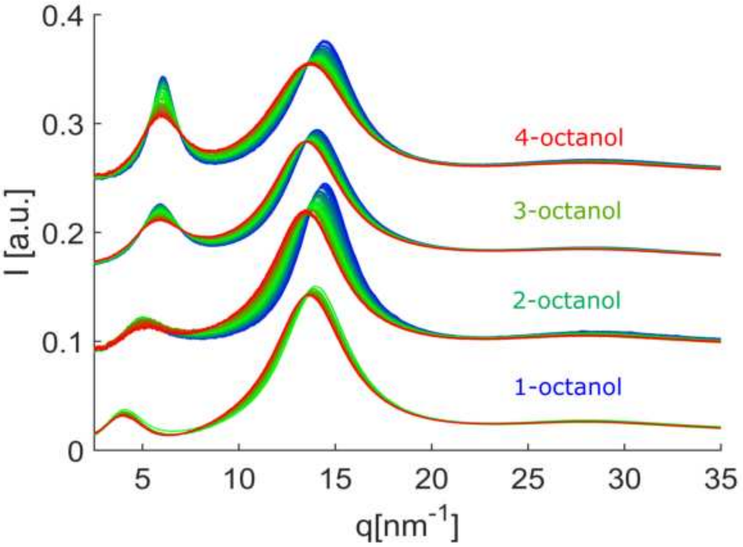

Figure 1: Diffraction patterns of n-Octanol (n=1,2,3,4) with the characteristic pre-and mainpeak

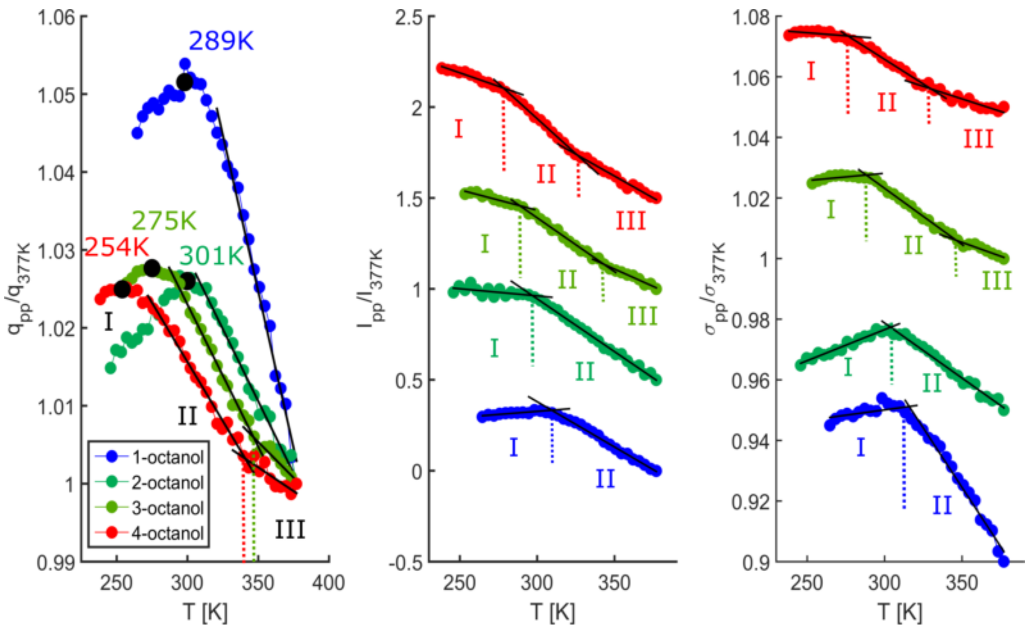

Figure 2: Prepeak position (q_{pp}) , intensity (I) and FWMH (σ_{pp}) of n-octanol at temperatures from 238 K to 377 K, black dot mark the transition point

The peak position increases with decreasing temperature (II) indicating a decrease of intermolecular distances, then exhibits a maximum and starts to decrease with further cooling (I). The decrease of the course is stronger for 1- and 2-octanol than for 3- and 4-octanol. This cross over can only be explained by a structural change and shifts with increasing branching to lower temperatures. For 3- and 4-octanol we observe an additionally change in slope for highest temperatures (III). This suggest that monomers predominantly occur. Based on the MD simulation it can be assumed that the dominant structure of 3- and 4-octanol consists of ring-like arrangements at room temperature [3]. Our results, indicate a change in the predominant species from rings to chains at low temperature. The increasing distance is in agreement with the chain formation. 1- and 2-octanol does not only consist of chain-like arrangements, but also of branched structures [3] and behaves differently at low temperatures. The structure of these MAs becomes more defined at low temperatures and the distance increase. Further investigations must show which structural changes take place at low temperatures with alcohols such as 1- and 2-octanol.

Reference

[1] Kaatze, U., Behrends, R., & Pottel, R. (2002). Hydrogen network fluctuations and dielectric spectrometry of liquids. Journal of Non-Crystalline Solids, 305(1), 19-28.
[2] Palombo, F., Sassi, P., Paolantoni, M., Morresi, A., & Cataliotti, R. S. (2006). Comparison of hydrogen bonding in 1-octanol and 2-octanol as probed by spectroscopic techniques. The Journal of Physical Chemistry B, 110(36), 18017-18025.
[3]Stephenson, S. K., Offeman, R. D., Robertson, G. H.,& Orts, W. J. (2006). Ethanol and water capacities of alcohols: a molecular dynamics study. Chemical engineering science, 61(17), 5834-5840. [4] Shinomiya, T. (1989). Dielectric Behavior and Intermolecular Association for Octanol Isomers. Existence and Transformation of a Nonpolar Cyclic Polymer. Bulletin of the Chemical Society of Japan, 62(11), 3643-3647.

Acknowledgement

CA, and GS thank the Deutsche Forschungsgemeinschaft for financial support via STE1079/4-1 and FOR1979, respectively and we would like to thank DELTA for providing synchrotron radiation and technical support.

In-situ synchrotron powder diffraction on tetraethynylozincates and –cadmates upon heating

M. Werker and U. Ruschewitz*

Department für Chemie, Universität zu Köln, 50939 Köln, Germany

**email: uwe.ruschewitz@uni-koeln.de*

One of our long-term research interests focuses on the synthesis and characterisation of ternary acetylides.[1] Numerous ternary alkali metal transition metal acetylides have been reported by our group for d^{10} configured metals like Pd(0)[2,3,4], Pt(0)[2,3,4], Cu^{+}[5], Ag^{+}[6] and Au^{+}[7]. All these compounds were only obtained as microcrystalline powders, so that X-ray powder diffraction data of high quality are needed to solve and refine their crystal structures unambiguously.

In all these compounds the acetylide anions coordinate end-on to the d^{10} metal resulting in a linear coordination and polymeric chains as structural fragment. By replacing these transition metals by Cd^{2+} or Zn^{2+} cations a tetrahedral coordination sphere is expected and the formation of 3D networks seems to be conceivable.[8]

Referring to the postulated reactions for the syntheses of some of the group 11 acetylides,[5,6,7] the literature known alkali metal tetraethynylozincates and –cadmates[9] were used as precursors for the synthesis of the respective ternary alkali metal zinc and cadmium acetylides. By heating $Cs_2Cd(C_2H)_4$ in an inert atmosphere at 200 °C we were able to obtain $Cs_2Cd(C_2H)_2(C_2)$ as a microcrystalline powder, whose crystal structure was solved and refined from synchrotron powder diffraction data recorded at BL9 (DELTA).[10] $Cs_2Cd(C_2H)_2(C_2)$ consists of tetrahedral $[Cd(C_2H)_2(C_2)_{2/2}]^{2-}$ units with terminating C_2H^- and bridging C_2^{2-} groups (Figure 1, left).

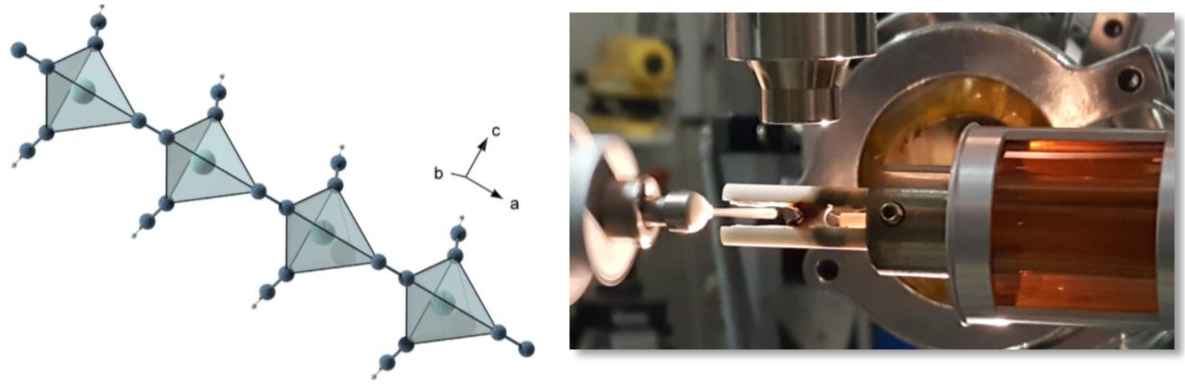

Figure 1: left: polymeric ${}^{1}_{\infty}[Cd(C_2H)_2(C_2)_{2/2}{}^{2-}]$ chains in the crystal structure of $Cs_2Cd(C_2H)_2(C_2)$; right: experimental setup of the *in-situ* heating experiments at Delta (BL9).

To follow the proposed formation according to $Cs_2Cd(C_2H)_4 \rightarrow Cs_2Cd(C_2H)_2(C_2) + C_2H_2$ by *in-situ* experiments, a specific experimental set-up was developed for beamline BL9 to account for the high sensitivity of the starting material and the product as well as the release of gaseous

C_2H_2 during the reaction (Figure 1, right). In this set-up the cryostreamer was only used as a source of N_2 gas to maintain inert conditions after opening the capillary with a glass cutter.

Surprisingly, using this set-up the formation of $Cs_2Cd(C_2H)_2(C_2)$ was not observed, but instead new reflections appeared. They could be assigned to elemental cadmium and a new compound, for which an orthorhombic unit cell and space group *Pnma* (no. 62) were ascertained. A structure model was developed, which showed that obviously Cs_2C_4 with $^-C{\equiv}C\text{-}C{\equiv}C^-$ units had formed.[11] This points to an oxidative coupling of C_2H^- units according to

$$Cs_2Cd(C_2H)_4 \rightarrow Cs_2C_4 + Cd + 2\ C_2H_2.$$

Attempts to reproduce this compound in lab experiments failed, but the observed formation of elemental cadmium corroborates the proposed reaction. Furthermore, in one experiment at DELTA the capillary could be sealed with picein tar after heating so that a Raman spectrum of the product was recorded, which showed the expected signals of a C_4^{2-} unit.

To investigate the influence of the synchrotron beam on this reaction one experiment with a closed shutter using the same set-up (Figure 1, right) was conducted, which also showed the formation of Cs_2C_4 and elemental cadmium. As similar observations were made upon heating $K_2Cd(C_2H)_4$ and $Rb_2Zn(C_2H)_4$, resp. we think that this reaction seems to be of general importance and further investigations in this field shall be performed in the near future.

[1] U. Ruschewitz, *Z. Anorg. Allg. Chem.* **2006**, *632*, 705.

[2] M. Weiß, U. Ruschewitz, *Z. Anorg. Allg. Chem.* **1997**, *623*, 1208.

[3] S. Hemmersbach, B. Zibrowius, W. Kockelmann, U. Ruschewitz, *Chem. Eur. J.* **2001**, *7*, 1952.

[4] U. Ruschewitz, *Z. Anorg. Allg. Chem.* **2001**, *627*, 1231.

[5] U. Cremer, U. Ruschewitz, *Solid State Sci.* **2002**, *4*, 247.

[6] W. Kockelmann, U. Ruschewitz, *Angew. Chem.* **1999**, *111*, 3697.

[7] J. Offermanns, U. Ruschewitz, *Z. Anorg. Allg. Chem.* **2000**, *626*, 649.

[8] M. Werker, U. Ruschewitz, *Z. Anorg. Allg. Chem.* **2016**, *642*, 1060.

[9] U. Cremer, U. Ruschewitz, *Z. Anorg. Allg. Chem.* **2004**, *630*, 337.

[10] M. Werker, U. Ruschewitz, *Inorg. Chem.* **2019**, doi: 10.1021/acs.inorgchem.9b02730.

[11] M. Werker, U. Ruschewitz, „Oxidative C-C Coupling in Solids", Poster at the 19. Vortragstagung für Anorganische Chemie der Fachgruppen Wöhler-Vereinigung und Festkörperchemie und Materialforschung, 24. – 27.9.2018, Regensburg.

BL9-Publications U. Ruschewitz and Co-workers

Articles

[1] V. K. Gramm, D. Smets, I. Grzesiak, T. Block, R. Pöttgen, M. Suta, C. Wickleder, T. Lorenz, U. Ruschewitz
$\text{Eu}(\text{O}_2\text{C-C}\equiv\text{C-CO}_2)$: An Eu^{II} Containing Anhydrous Coordination Polymer with High Stability and Negative Thermal Expansion
Chem. Eur. J. **2019**, submitted.

[2] M. Werker, U. Ruschewitz
$\text{Cs}_2\text{Cd}(\text{C}_2\text{H})_2(\text{C}_2)$: A Crystalline Acetylide with Bridging C_2 Units
Inorg. Chem. **2019**, doi: 10.1021/acs.inorgchem.9b02730.

[3] D. Hermann, H. A. Schwartz, M. Werker, D. Schaniel, U. Ruschewitz
Metal-Organic Frameworks as Hosts for Fluorinated Azobenzenes: A Path Towards Quantitative Photoswitching with Visible Light
Chem. Eur. J. **2019**, *25*, 3606-3616.

[4] M. Hetzert, M. Werker, U. Ruschewitz
$\text{A}^{\text{I}}\text{SeC}_2\text{H}$ with A^{I} = K, Rb, Cs: crystalline compounds with the elusive $^{-}\text{Se-C}\equiv\text{C-H}$ anion
Angew. Chem. Int. Ed. **2018**, *57*, 16475-16479; *Angew. Chem.* **2018**, *130*, 16713-16717.

[5] C. Stastny, B. Dolfus, C. T. Brombach, D. Dresen, S. Disch, R. Glaum, U. Ruschewitz
New 2D and 3D Coordination Polymers by Dehydration of $^{1}_{\infty}[\text{M}^{\text{II}}(t F\text{-BDC})(\text{H}_2\text{O})_4]$ with $\text{M}^{\text{II}} = \text{Zn}^{2+}$, Co^{2+}, Ni^{2+} and $tF\text{-BDC}^{2-}$ = tetrafluoroterephthalate
Z. Anorg. Allg. Chem. **2018**, *644*, 1423-1430.

Doctoral thesis

[1] M. Werker, *Reaktionen von Alkalimetallacetyliden mit Zink- und Cadmiumverbindungen*, Köln **2019**.

Master thesis

[1] H. Laurenzen, *Investigation of Host-Guest Interactions in Photoswitch@MOF Systems*, Köln **2019**.

Crystalline and highly oriented growth of SCO Hofmann-type coordination polymers over MoS_2 flakes

Alejandro Núñez-López,[1] Ramón Torres-Cavanilles,[1] Victor Rubio-Giménez[1]
Alicia Forment-Aliaga,[1] and Eugenio Coronado[1]

[1]Instituto de Ciencia Molecular, Universitat de València, Catedrático José Beltrán 2, 46980 Paterna, Spain.

Transition metal dichalcogenides (TMDs) are a well-known class of 2D Van der Walls materials that excel in their electrical and optic properties at the 2D limit that evolve from the quantum confinement and surface effects.[1] These properties are ready to be tuned by external stimuli applying strain.[2]

In this work, we have used a network of MoS_2 flakes as the starting point of growing a 2D Hoffman-type coordination polymer (HCP): $[Fe(py)_2\{Pt(CN)_4\}]$ (py=pyridine). Previous work in our group showed that the spin-crossover (SCO) properties of the bulk material are preserved in thin films of these material grown by Layer-by-Layer (LbL) onto Au substrate.[3] We expected that the strain applied to the MoS_2 layers as a result of the spin transition could modulate its electrical and optic response.

Prior to the beamtime, MoS_2/HCP heteroestructures were prepared onto Si substrates and characterized by several techniques: AFM, XPS, IRRAS in both 2H and 1T MoS_2 polytopes. Furthermore, the SCO properties of the HCP were studied by XAS measurements in DEIMOS beamtime at SOLEIL, showing that the SCO phenomena can still be detected in nanometric MoS_2/HCP heterostructures. However, the crystallinity of the heterostructure needed to be studied through powerful characterization techniques like synchrotron XRD due to the low electronic density and nanometric thickness of the HCP.

We prepared samples before and after the growth of 30 layers of HCP over 2H and 1T MoS_2 and measured surface XRD at BL9 using the two-dimensional image-plate detector (MARCCD) at a wavelength of 0.82 Å (15 keV). Figure 1 shows the results obtained in the out-of-plane and in-plane profiles of the 2H MoS_2 samples which matches with the simulated spectra of 2H MoS_2 and HCP. This result proves the oriented and crystalline growth of the HCP over the 2H MoS_2 flakes.

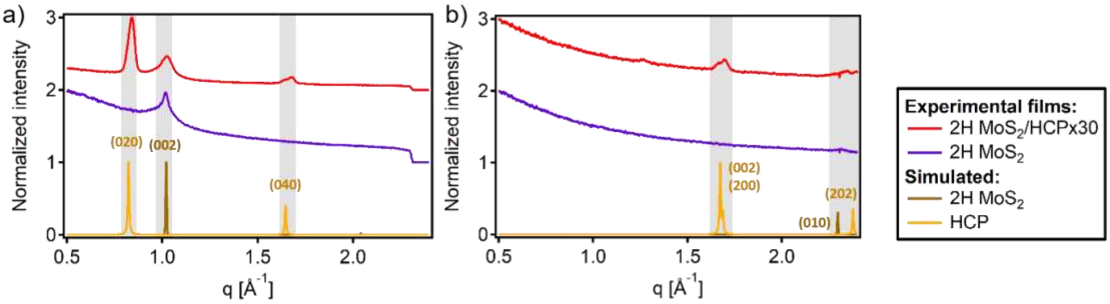

Figure 1. Out-of-plane (a) and in-plane (b) profiles of $[Fe(py)_2\{Pt(CN)_4\}]$ 30 layers-thick grown onto 2H MoS_2 (red) and bare MoS_2 2H (blue). The brown and yellow patterns show the simulated profile of 2H MoS_2 and $[Fe(py)_2\{Pt(CN)_4\}]$ respectively.

The same procedure was followed for the 1T MoS_2 samples. A similar result was obtained though it should be pointed the presence of a new peak in the 1T MoS_2 out-of-plane spectra while the intensity of the (001) peak decreases, as a result of the intercalation of solvent molecules between the MoS_2 layers during the deposition of 1T MoS_2 onto the substrate in solution, which increases the interlayer distance.

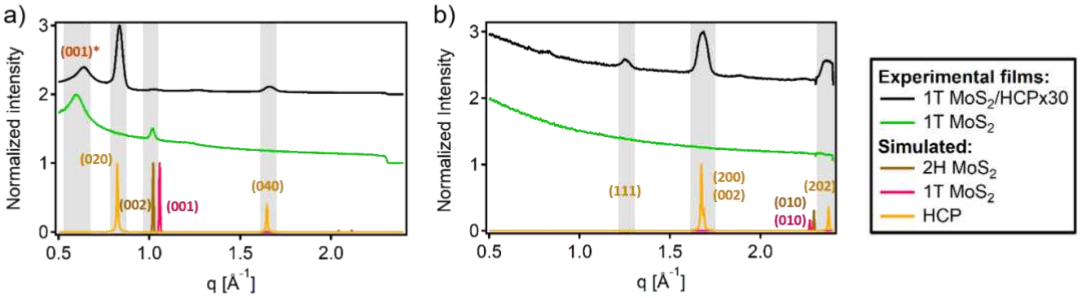

Figure 2. Out-of-plane (a) and in-plane (b) profiles of $[Fe(py)_2\{Pt(CN)_4\}]$ 30 layers-thick grown onto 1T MoS_2 (black) and bare MoS_2 1T (green). The brown and pink patterns show the simulated profile of 2H and 1T MoS_2 while the yellow pattern represent the simulated profile of $[Fe(py)_2\{Pt(CN)_4\}]$.

These results confirmed not only the crystallinity of the both components of the MoS_2/HCP heterostructure, but also the oriented growth of the HCP over the MoS_2 flakes. The HCP $[Fe(py)_2\{Pt(CN)_4\}]$ 2D layers grow parallel to the ones of MoS_2 and parallel to the surface of the bottom Si substrate (Figure 3).

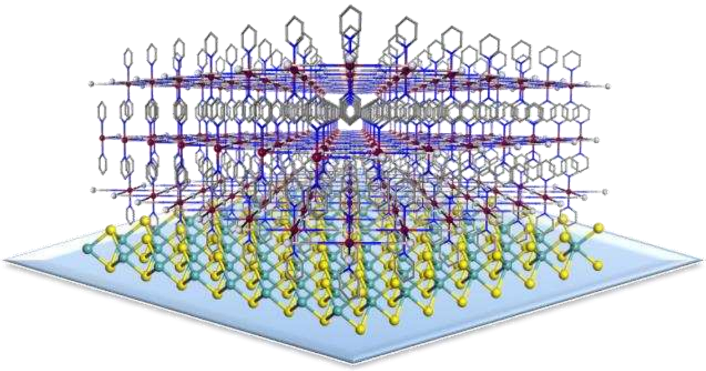

Figure 3. Schematic representation of the oriented growth of the HCP $[Fe(py)_2\{Pt(CN)_4\}]$ over MoS_2 flakes. Both 2D materials have parallel orientations of their respective 2D layers.

---

[1] W. Choi, N. Choudhary, G. H. Han, J. Park, D. Akinwande, Y. H. Lee, *Mater. Today* **2017**, *20*, 116–130.

[2] S. Manzeli, A. Allain, A. Ghadimi, A. Kis, *Nano Lett.* **2015**, *15*, 5330–5335.

[3] V. Rubio-Giménez, C. Bartual-Murgui, M. Galbiati, A. Núñez-López, J. Castells-Gil, B. Quinard, P. Seneor, E. Otero, P. Ohresser, A. Cantarero, et al., *Chem. Sci.* **2019**, *10*, 4038–4047.

Crystallinity of swollen PMMA composite films with various GNP and CNT contents

O. Ozturk[a], *G. Akin Evingur*[b], *U. Pietsch*[a]

[a]*Department of Physics, Siegen University, Siegen, Germany*
[b]*Department of Industrial Engineering, Piri Reis University, Istanbul, Turkey*

ABSTRACT

Copolymer based on cross-linked Poly (methyl methacrylate) (PMMA) doped by graphene nanopallets (GNP) and carbon nanotube (CNT) were prepared with various amounts of GNP and CNT varying in the range between 0 wt.% and 30 wt.%. Crystallinity of these composites were investigated by X-ray diffraction measurements before and after swelling of the samples. It is observed that the crystallinity of the samples are increasing with the CNT and GNP amount before swelling. After the swelling a decrease in interlattice spacing is determined.

INTRODUCTION

Due to their physical and chemical properties,the responsive smart polymers have been evaluated in different fields particularly biosensors, medical diagnostics and drug delivery systems [1]. PMMA is a member of thermoplastic polymers family with amorphous structure, linear chain, low production cost and wide industrial applications (biomedical applications, optics, vehicle industry, electrical engineering, medicine, etc.). Graphene-doped PMMA composites have the advantage related to the hardness, toughness, dimensional and heat balance [2]. Studies have shown that the microstructure and viscoelastic properties of the PMMA are significantly improved by the addition of a low amount of graphene nanopaletes (GNP) and carbon nanotubes (CNT). It is still a challenge to have mechanically strong PMMA composites. It was previously determined that the mechanical modulus of such composites depends on the crystallinity [3]. Therefore we are trying to optimize the mechanical strength of PMMA copolymers by modifiying the nanofiller content.

EXPERIMENT

PMMA, which is in powder form were combined with nanofillers by using a magnetic stirrer for 48 hours and were kept in ultrasonic bath for 1 hour. Afterwards the composite films are prepared by drop casting method. Ammonium persulfate and $N, N\prime-$methylenebis (acrylamide) (BIS) were used as a free radical initiator and a crosslinker.

During the experiment done at DELTA, BL 10, the X-ray diffraction measurements were performed with a beam of energy, $12keV$ and Pilatus 2D detector. The experiments were performed at room temperature while a flight tube is used to have a higher intensity. For the swelling process, the samples were kept in ethanol for different times and the measurements were performed immediately. The angular values and the background of raw data have been calibrated with respect to the distance and beam centre position in x and y coordinates using silicon powder as a reference material. Radial line scans were extracted by azimuth averaging the Debye Scherrer rings using the software Fit2D.

RESULTS

After calibration of the raw data, the diffraction patterns of PMMA-GNP and PMMA-CNT composites have been obtained as shown in Figure 1. The relatively small degree of crystallinity together with the large amount of diffuse scattering is typical for such copolymers. The peaks at $0.9A^{-1}$ and at $2.2A^{-1}$ are the characteristic PMMA peaks. As the nanofiller amount in the composite increases, the peaks become more pronounced and their intensities increase, this indicates that the crystallinity of the composite increases as a function of nanofiller content.The FWHM values of the peaks also increase with the nanofiller concentration, pointing the increase in the average size of the crystalline domains. This is consistent with the

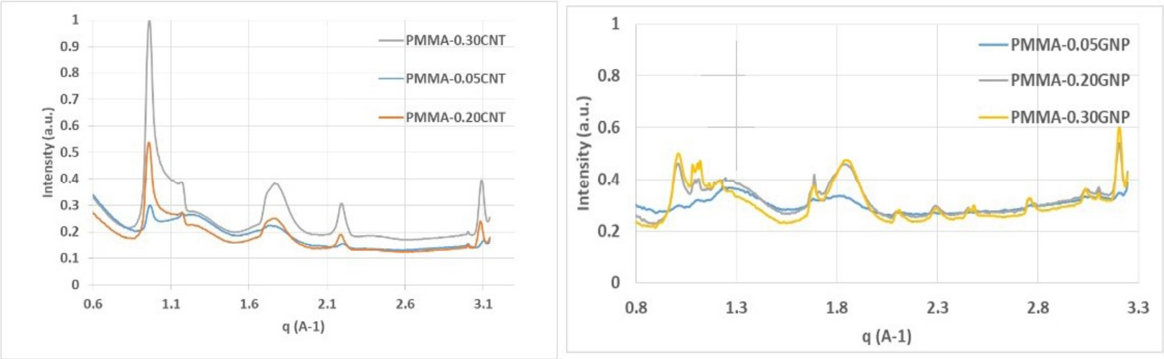

Figure 1. The diffraction patterns of PMMA-CNT and PMMA-GNP composites with different CNT and GNP amounts by weight before swelling.

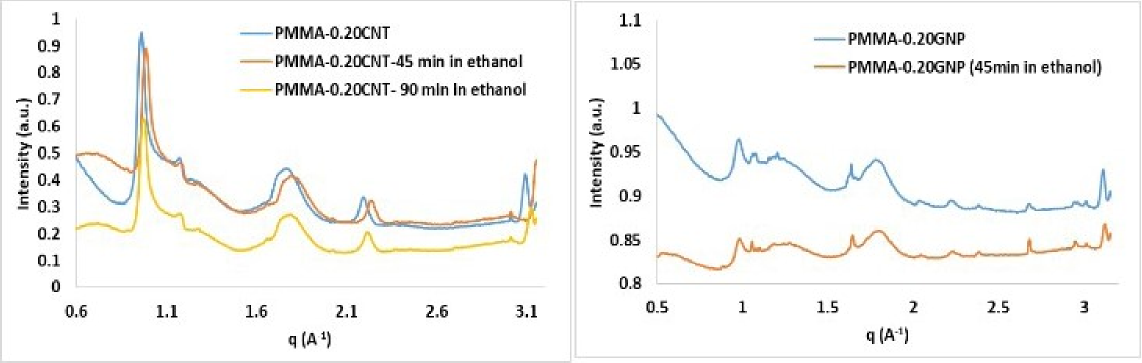

Figure 2. The diffraction patterns of PMMA-0.20CNT and PMMA-0.20GNP composites after swelling in ethanol.

decrease of the average distance between the adjacent crystalline domains with the increase of nanofiller concentration as the growth of crystalline domains consumes the interstitial polymer chains.

Swelling degree of such composites is determined by their cross-link density and the number of crystalline domains act as physical cross-link. PMMA-CNT composites which has higher crystallinity shows an observable response to swelling [4]. After the swelling, the PMMA-CNT composites were determined to have a slight shift to the higher q values as can be seen in Figure 2. This decrease in the interlattice spacing is meaningful, because swelling of the interstitial polymer chains decreases the average distance between the lattices.The PMMA-GNP composites have showed no pronounced change after the swelling.

CONCLUSIONS

In thi study, it was shown that the crystal structure of the PMMA composites show a dependence on the nanofiller and the nanofiller concentration, while the swelling of the PMMA-CNT composites affects the lattice spacing of the composites. Increase in crystallinity with GNP and CNT reinforcement can be related to the nucleation effects of the nanofillers causing the growth of new crystalline domains around them. These structural and morphological changes might enhance the mechanical strength of the polymers and make it possible to design anti-fatigue-fracture copolymers.

REFERENCES

1. A. Darumas Putri et.al., *Scientific Reports* 9, 7873 (2019).
2. K.Shi et.al., *Applied Materials and Interfaces* 7, 27289 (2015).
3. N.S.DeLong et.al., *Macromolecules* 39, 1308 (2006).
4. C.Bilici et.al., *Polymer* 151 (2018).

Supramolecular structure of n-octanol/water mixtures

Jennifer Bolle, Christian Sternemann, Michael Paulus, Eric Schneider and Metin Tolan
Fakultät Physik/DELTA, Technische Universität Dortmund, 44221 Dortmund, Germany

Monohydroxyalcohols (MAs) were investigated as models for hydrogen-bound liquids. Hydrogen bonds are essential for understanding the microscopic structure of water, aqueous solutions and alcohols [1]. Mediated by hydrogen bonds, the MAs can generate ring-like or chain-like supramolecular structures. 1-octanol water mixtures are often used experimentally as membrane mimetics. It serves as a model for predicting pharmacokinetic properties of drug molecules. Computer simulations studies show that 1-octanol forms long thin chains. With the addition of water, the chains become longer and more bended [2]. Stephenson et al. investigated pure n-octanol with MD simulations and discovered that ring formation is favored with stronger shielding of the OH group [3].

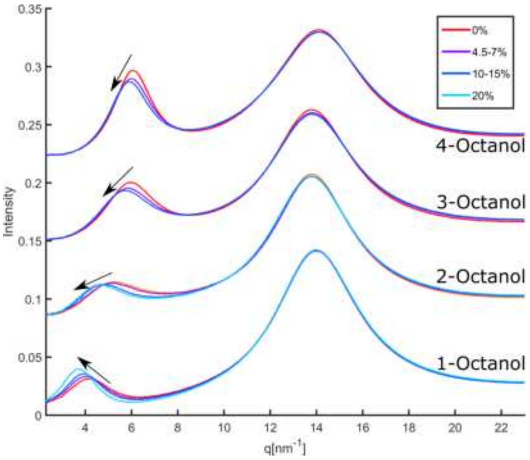

Figure 1: Diffraction patterns of n-octanol/water mixtures (n=1,2,3,4) with the characteristic pre-and main-peak

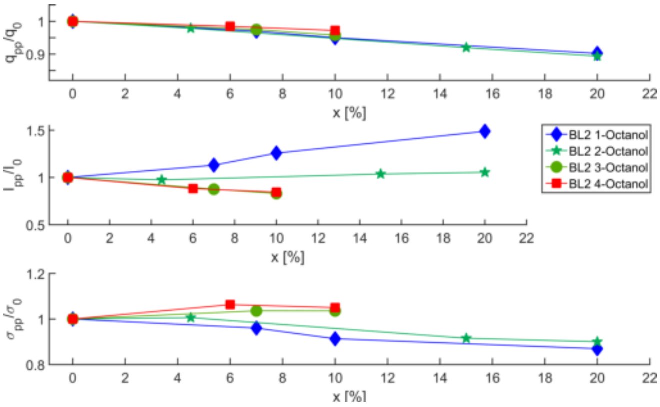

Figure 2: Position q_{pp}, intensity I_{pp} and FWHM σ_{pp} of the prepeak for (n-octanol)$_{x-1}$(water)$_x$ with the concentrations x. All results are normalized to the values of the pure substances.

We study the influence of water on the ring-like and chain-like structure of n-octanol (n=1,2,3,4). Mixtures with up to a molar fraction of 20% water were investigated by X-ray diffraction (XRD) at beamline BL2 of the synchrotron light source DELTA (TU Dortmund, Dortmund, Germany). The MAs were filled in borosilicate capillaries with 3.5 mm diameter and were measured at an photon energy of 12 keV. The corresponding diffraction patterns are shown in figure 1. The main peak occurs at higher momentum transfer (q) and is predominant due to the carbon-carbon correlations in the liquid. The prepeak at lower q reflects typical distances owing to oxygen-oxygen correlations. For a detailed analysis of the main- and prepeak a linear background was subtracted. Then the peak was fitted with a pearson VII-function. The addition of water to the MAs results in a shift to smaller peak positions. The water has hardly any influence on the carbon-carbon correlation. The exact results of the prepeak analysis can be found in figure 2. All results were normalized to the values of the pure substances for better comparability. The results clearly show that 1-octanol and to some extent 2-octanol behave differently than the other MAs. The intensity of the prepeak increases or is constant and more defined structures are formed with the addition of water. The prepeak intensity of 3- and 4-octanol decreases with increasing concentration and the peak width increases, due to a more disordered mixture. The dominant structure of 1-octanol consists of chains. As the shielding increases, more and more rings are formed. For 3- and 4-octanol rings are the dominant structure. Our results show that water extends the chains and promotes the structure, this leads to a more defined peak width. In alcohols with dominant ring structures, water disturbs the structure.

Reference

[1] Kaatze, U., Behrends, R., & Pottel, R. (2002). Hydrogen network fluctuations and dielectric spectrometry of liquids. Journal of Non-Crystalline Solids, 305(1), 19-28.
[2] MacCallum, J. L., & Tieleman, D. P. (2002). Structures of neat and hydrated 1-octanol from computer simulations. Journal of the American Chemical Society, 124(50), 15085-15093.
[3]Stephenson, S. K., Offeman, R. D., Robertson, G. H.,& Orts, W. J. (2006). Ethanol and water capacities of alcohols: a molecular dynamics study. Chemical engineering science, 61(17), 5834-5840. [4] Shinomiya, T. (1989). Dielectric Behavior and Intermolecular Association for Octanol Isomers. Existence and Transformation of a Nonpolar Cyclic Polymer. Bulletin of the Chemical Society of Japan, 62(11), 3643-3647.

Acknowledgement

GS thank the Deutsche Forschungsgemeinschaft for financial support via FOR1979, respectively and we would like to thank DELTA for providing synchrotron radiation and technical support.

The effect of viral fusion peptides on the lamellar to cubic transition dynamics of monoolein in excess water

Göran Surmeier, Michael Paulus, Christian Sternemann, Mirko Elbers, Christian Albers, Jennifer Bolle, Marc Moron, Mike Moron, Marvin Kowalski, Christopher Cewe, and Julia Nase

Fakultät Physik/DELTA, TU Dortmund, 44221 Dortmund, Germany

Email: goeran.surmeier@tu-dortmund.de

Fusion peptides (FP) are segments of viral fusion proteins which drive the fusion process of viral envelope and cell membrane that occurs when a virus enters a host cell. They are located in the ectodomain and their insertion into the target membrane leads to destabilization and initiates the formation of fusion pores. Former studies led to a classification of fusion proteins upon specific structural features into three different classes, with different properties and thus different interaction mechanisms with target membranes. In our study, we investigated the FPs of the fusion proteins influenza virus hemagglutinin 2 (HA2) (class I), tick-borne encephalitis virus (TBEV) glycoprotein E (class II), and vesicular stomatitis virus (VSV) G protein (class III). The membrane perturbing properties of FPs are reflected in a modified p-T-diagram of mesophases formed by lipids in an aqueous environment [1]. As the structure of cubic mesophases resembles intermediate states that occur during fusion pore formation, the role of FPs in viral membrane fusion can be examined by studying their effect on the lamellar to cubic transition.

In this experiment, we induced the lamellar crystalline L_c to cubic Pn3m phase transition of monoolein in excess water by conducting pressure jumps in a high hydrostatic pressure sample cell [2]. After the pressure jump, we monitored the sample structure with SAXS every three minutes for several hours. The phase and the corresponding lattice constant a can be determined from the scattering angles of diffraction fringes that occur in the SAXS patterns. The scattering angle α is connected to the momentum transfer $q = \frac{4\pi}{\lambda} \sin\frac{\alpha}{2}$. The fringes occur at specific multiples of the reciprocal lattice constant $\frac{2\pi}{a}$ that are characteristic for every given phase, e.g., $\sqrt{2}$, $\sqrt{3}$, $\sqrt{4}$, $\sqrt{6}$ ... for the cubic Pn3m phase, and 1, 2, 3, 4 ... for lamellar phases. The experiment was performed at beamline BL9 at a photon energy of 13 keV.

Figure 1 illustrates the measuring procedure. In order to determine the equilibrium lattice constant, we recorded a reference SAXS image at 50 bar before we induced the cubic to lamellar phase transition by increasing the pressure. Then, we conducted a pressure jump from 1 kbar down to 50 bar and we observed that the cubic Pn3m structure was formed with a much larger lattice constant than observed in the reference measurement and decreased slowly to an equilibrium value over time. Figure 2 depicts how the integrated SAXS curves were fitted. We subtracted an interpolated background and fitted seven gaussian distributions with a fixed ratio between their positions to the first seven Bragg reflections in order to determine the lattice constant. The relaxation of the lattice constant in absence and presence of the three FPs can be seen in figure 3. We observed that HA2-FP accelerates the relaxation, while TBEV-FP and VSV-FP slow it down. A detailed data analysis is still in progress.

Acknowledgments: This work is supported by the Forschergruppe 1979 (**DFG-FOR1979**). We also acknowledge the Delta machine group for providing synchrotron radiation and technical support. CA thanks the DFG for financial support via STE1079/4-1. Gefördert durch die Deutsche Forschungsgemeinschaft (DFG) im Rahmen der Exzellenzstrategie des Bundes und der Länder – EXC 2033 – Projektnummer 390677874.

References: [1] Artem Levin, Christoph Jeworrek, Roland Winter, Katrin Weise, and Claus Czeslik, *J. Phys. Chem. B* **121** (2017) 8492. [2] C. Krywka, C. Sternemann, M. Paulus, M. Tolan, C. Royer and R. Winter, *ChemPhysChem* **9** (2008) 2809–2815.

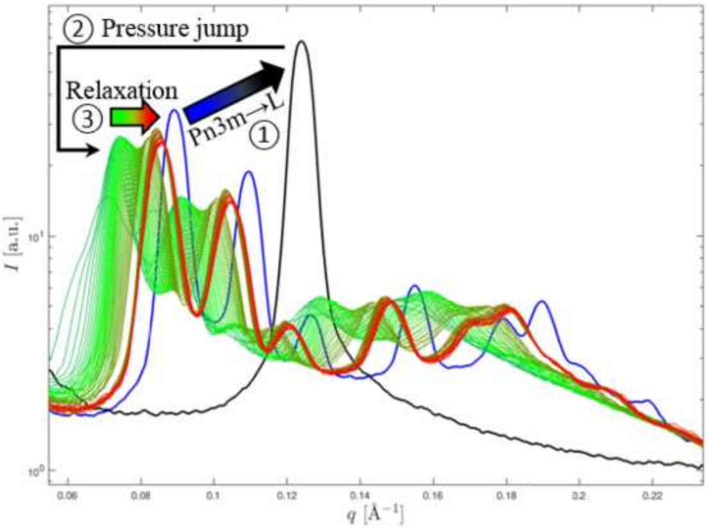

Figure 1: Integrated SAXS patterns of monoolein in the Pn3m phase at 50 bar at equilibrium (*blue curve*), in the lamellar phase at 1000 bar just before the pressure jump (*black curve*), and after the pressure jump down to 50 bar slowly approaching the initial state again (*green to red*).

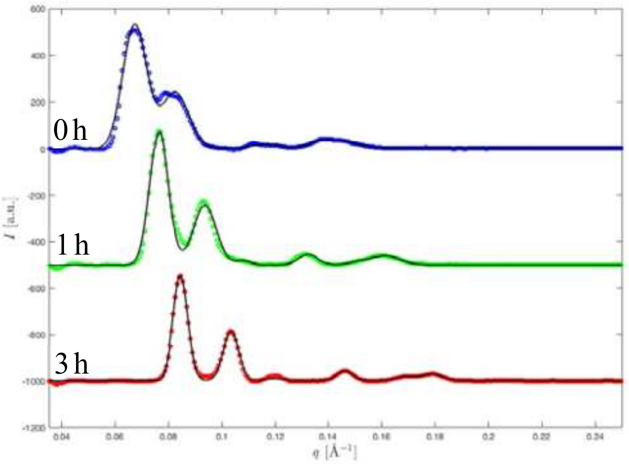

Figure 2: Integrated SAXS patterns of monoolein in the Pn3m phase at 50 bar at different times after the pressure jump (*colored circles*) and the obtained fits (*black*). The curves are vertically shifted for clarity.

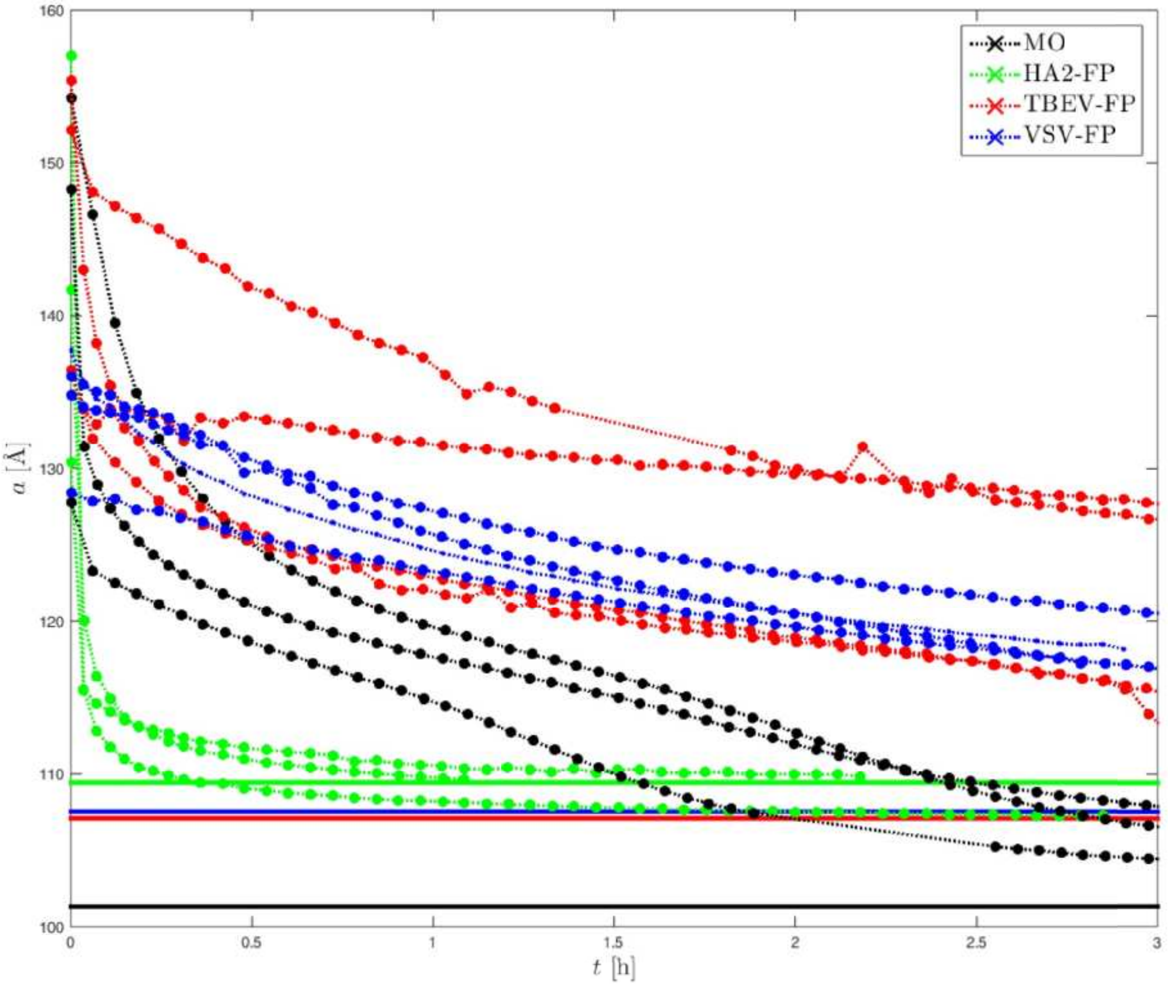

Figure 3: Relaxation of the Pn3m lattice constant *a* after a pressure jump from 1000 to 50 bar. The dashed lines connect data points that belong to the same sample. The solid lines mark the mean values of the lattice constants at equilibrium. Note that the equilibrium lattice constant can vary by a few angströms from sample to sample due to small variations of the peptide concentration.

Gas adsorption on hydrophobic surfaces near the critical point

Mike Moron, Göran Surmeier, Jennifer Bolle, Marc Moron, Julia Nase, Michael Paulus, and Metin Tolan

Fakultät Physik/DELTA, TU Dortmund, 44221 Dortmund, Germany

We investigated the pressure-dependent gas adsorption on hydrophobically coated silicon wafers. The silicon wafers were hydrophobized by coating them with a self-assembled octadecyltrichlorsilane(OTS) monolayer. OTS molecules bind covalently with their polar head group to the wafers surface. Thus, the nonpolar alkyl chains form a stable, hydrophobic surface. The gases under investigation were CO_2 ($p_{\mathrm{crit}}^{\mathrm{CO_2}} = 73.75\,\mathrm{bar}$, $T_{\mathrm{crit}}^{\mathrm{CO_2}} = 30.98\,°\mathrm{C}$) and argon ($p_{\mathrm{crit}}^{\mathrm{Ar}} = 48.96\,\mathrm{bar}$, $T_{\mathrm{crit}}^{\mathrm{Ar}} = -122.29\,°\mathrm{C}$) at different gas pressures up to $60\,\mathrm{bar}$. The sample cell can sustain gas pressures of up to 100 bar. Since the gas adsorption layers are on the atomic scale, we performed an x-ray-reflectivity (XRR) experiment with a photon beam energy of 27 keV at the beamline BL9 at DELTA. With the XRR technique we obtain direct insight into the vertical electron density profile of the substrate and the adsorbed gas layers. The recorded reflectivity curves for the CO_2 measurements are shown in figure 1. The reflectivities were recorded at a temperature of $8\,°\mathrm{C}$, thus below T_{crit}. The curves are shifted vertically for clarity. The dashed, vertical line makes the position of the first minimum of the reference measurement of the solid-air interface and serves as guide to the eye. With higher gas pressure, the first minima of the reflectivity curves shift to lower momentum transfers q_z. This shift indicates the adsorption of a CO_2 layer. Figure 2 shows the electron density profiles of the layer system perpendicular to the surface, depending on the CO_2 pressure. The electron density profiles were obtained by fitting a model system to the data using the Parratt algorithm in combination with the Effecive density model. The first layer visible in figure 2 characterizes the silicon substrate. The second layer represents the SiO_2 layer that is formed when the wafer is exposed to air. The next two layers represent the head group and the tail group of the OTS molecules. The OTS monolayer seems not to be affected by CO_2. The top layer in the electron density profiles describe the adsorbed CO_2 layer. From a pressure of 4 bar a CO_2 layer is formed whose thickness slightly decreases with increasing pressure. The electron density of the CO2 layer increases with higher gas pressure. However, the observed densities are significantly lower, compared to the bulk value of liquid carbon dioxide, which is around 0.28 $e^-/Å^3$. Such a decreased electron density seems to be a characteristic of gas adsorption on hydrophobic surfaces and differs for the adsorption on hydrophilic surfaces. The reflectivity curves and the corresponding electron density profiles for the argon measurements are shown in figure 3 and figure 4 respectively. Note that in this reflectivity series the critical point is passed. At the given conditions, Argon shows a weaker adsorption behavior compared to CO_2. An argon layer can first be observed at a pressure of $10\,\mathrm{bar}$. The density of the argon layer is very low. The electron density of the argon layer increases, just like with CO_2, with increasing gas pressure.

Further measurements will be performed using hexafluorethane (C_2F_6) as a model gas to investigate the effect of different gas phases more detailed.

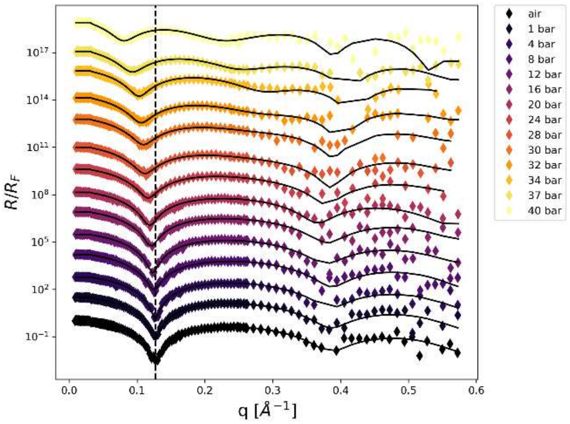

Figure 1: Reflectivity curves of the CO_2 measurements

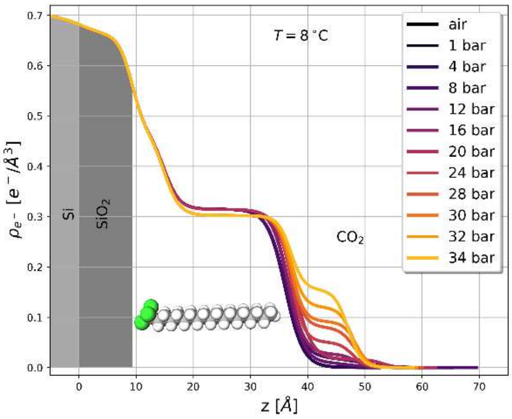

Figure 2: Electron density profiles of the CO_2-measurements

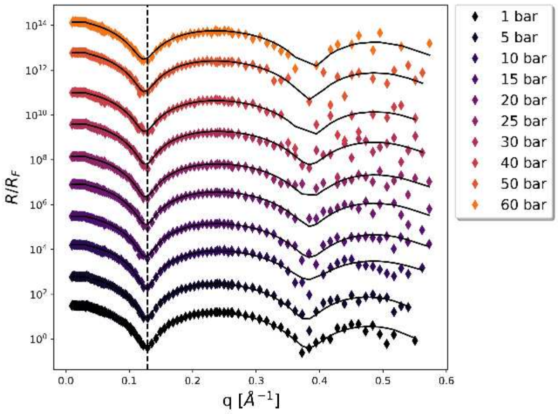

Figure 3: Reflectivity curves for the argon measurements

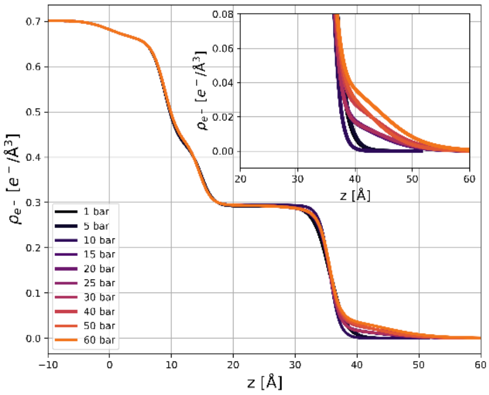

Figure 4: Electron density profiles for the argon measurements

Acknowledgements: This work is supported by the Federal Ministry of Education and Research (BMBF project number: 05K19PEA) and by the Forschergruppe 1979 (**DFG-FOR1979**). We also acknowledge the Delta machine group for providing synchrotron radiation and technical support.

Exploring the breathing behaviour of functionalized flexible metal-organic frameworks during *n*-butane sorption via *in situ* PXRD

Roman Pallach, Louis Frentzel-Beyme, Sebastian Henke*

Anorganische Chemie – TU Dortmund, Otto-Hahn-Str. 6, 44227 Dortmund

Flexible metal-organic frameworks (MOFs) undergo reversible structural transitions, if exposed to external stimuli, such as adsorption of gas or solvent molecules or changes in temperature and mechanical pressure. This exceptional property makes these materials a fruitful target of research, aiming at future technological applications within the scope of sensing, gas separation/storage and heat storage or transfer.[1,2] In this context, we investigated the phase behaviour of novel flexible derivatives of the dabco-MOF (DMOF) and isoreticular MOF (IRMOF) families as a function of *n*-butane pressure by powder X-ray diffraction (PXRD) at DELTA.

This study was realized at DELTA beamline BL9 by use of a diamond-windowed high-pressure gas cell. Since the experiments were carried out at ambient temperature, *n*-butane pressures of up to ~2.8 bar were applied to achieve coverage of the entire relative pressure range of *n*-butane ($0 < p/p_0 < 1$, p_0 for *n*-butane at ambient temperature is ~2.5 bar). The chosen pressure-resolution (Δp) was 500 mbar. An X-ray beam with an energy of 22 keV, a beamsize of 0.2 x 1.0 mm^2 and the MAR345 detector were used.

1. dabco-MOFs

The series of DMOFs under investigation is characterized by a *ethyl*-, *propyl*- or *butyl*-functionalization of the organic building block, therefore resulting in a general chemical composition of $Zn_2(R_2\text{-bdc})_2(\text{dabco})$ (with $R_2\text{-bdc}^{2-}$ = 2,5-*dialkyl*-functionalized 1,4-benzenedicarboxylate; R = *Et* (**C2**), *ⁿPr* (**C3**), *ⁿBu* (**C4**); dabco = 1,4-diazabicyclo[2.2.2]-octane). These materials transform from a guest-containing large pore (***lp***) phase to a contracted narrow pore (***np***) phase upon removal of the solvent guest molecules (Fig. 1). A similar behaviour was observed for related DMOFs bearing a *dialkoxy*-functionalization.[3–5]

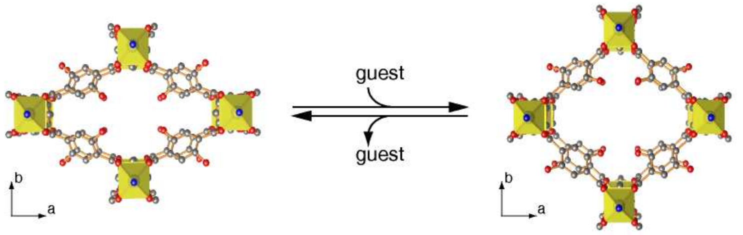

Fig. 1. Graphical representation of the reversible guest-induced narrow pore (***np***) to large pore (***lp***) transition of $Zn_2(R_2\text{-bdc})_2(\text{dabco})$ (R = linear alkyl group) DMOF materials. Zn, O, N and C atoms are shown in yellow, red, blue and grey. H atoms are omitted for clarity. The positions of the alkyl side chains are indicated as red spheres pointing into the pores.

We were able to observe the guest-adsorption-driven ***np***-to-***lp*** transition of these materials via *in situ* PXRD experiments under variable *n*-butane pressure at DELTA. The **C2**- and **C3**-functionalized DMOFs readily transform to the ***lp***-phase upon addition of the first dose of *n*-butane at a pressure of 500 mbar (Fig. 2a and b). Remarkably, upon re-evacuation these two compounds do not retransform to the ***np***-phase. In contrast to this, DMOF-**C4** transforms from the ***np***- to the ***lp***-phase at a higher *n*-butane pressure of 1000 mbar and retransforms to the ***np***-phase when the sample is evacuated (Fig. 2c).

In general, these data nicely reflect the trends, we obtained from volumetric gas physisorption measurements and we will now evaluate the detailed crystallographic structures of the individual ***np*** and ***lp*** phases of these DMOFs. The results will be published as part of a comprehensive work containing further analytical data from methods, such as variable temperature PXRD (previously also collected at BL9 of DELTA), DSC, IR and isothermal gas sorption measurements.

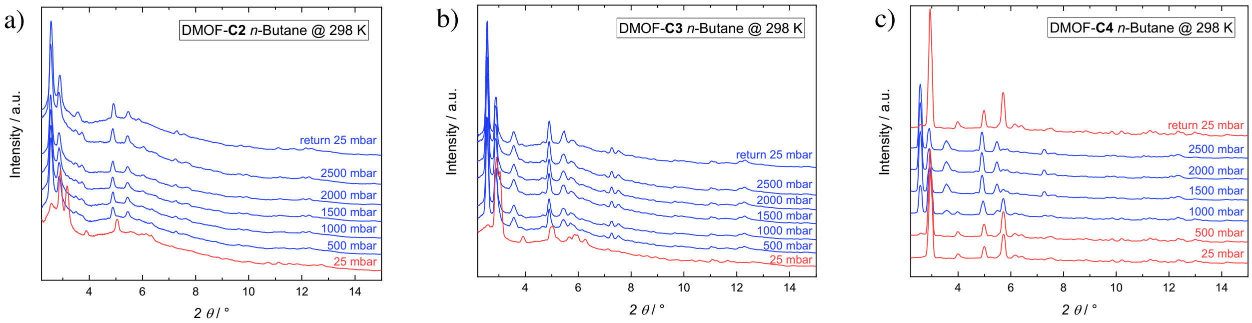

Fig. 2. PXRD patterns of *alkyl*-functionalized DMOFs collected at different *n*-butane pressures at BL9 of DELTA. Red colour indicates the presence of the ***np***-phase, blue colour indicates the presence of the ***lp***-phase.

2. Isoreticular MOFs

We also studied the guest-dependent phase behaviour of a series of ether-functionalised derivatives of MOF-5[6] (IRMOFs; MOF-5-**CX**; chemical composition: $Zn_4O(2,5\text{-}(\mathbf{OC_XH_{2X+1}})bdc)_3$; bdc^{2-} = 1,4-benzenedicarboxylate) via *PXRD* at variable *n*-butane pressure. Even though MOF-5 is known for its structural rigidity and non-responsiveness,[7,8] these compounds undergo reversible structural transitions from its cubic phase to a rhombohedral or an X-ray amorphous phase, depending on the lengths of the alkoxy substituent **CX** (Fig. 3). The transitions between the different phases (Fig. 3b) can be triggered by ad- or desorption of guest molecules, such as *N,N*-dimethylformamide or *n*-octane, but also by temperature changes. X-ray total scatting experiments and pair distribution function analysis suggest that the X-ray amorphous phase originates from a *random* distortion of the $Zn_4O(O_2C)_6$ building units, while in the rhombohedral phase all of these building units distort in a *concerted* fashion.

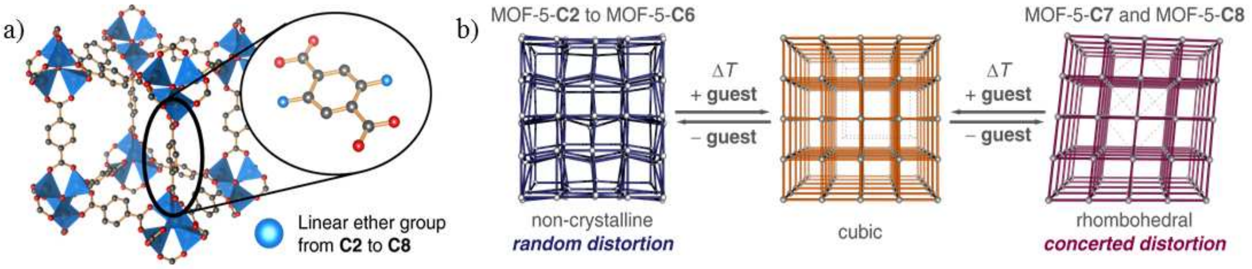

Fig. 3. a) Schematic representation of the crystal structure of the prototypical MOF-5 and the chemical structure of the utilized ether-functionalised bdc^{2-} linkers. Zn, O and C atoms are shown in grey, red and black. b) Illustration of the guest- or temperature-induced structural flexibility of the MOF-5-**CX** derivatives. Spheres and sticks resemble $Zn_4O(O_2C)_6$ nodes and linker-backbones.

The PXRD data as a function of *n*-butane pressure suggest that the short-chained, X-ray amorphous MOFs, such as MOF-5-**C3**, undergo a significant expansion of their distorted framework, as visible in the continuous shift of the diffuse scattering peaks with increasing *n*-butane pressure (Fig. 4a). However, a full transition to the highly crystalline cubic phase was not observed for the compounds with short chained substituents. Interestingly, by increasing the length of the alkyl chain up to **C6**, a continuous increase in the intensity and decrease of the line width of the Bragg reflections with increasing *n*-butane pressure is apparent, indicating a transition from the X-ray amorphous to the cubic phase (Fig. 4b). In accordance with volumetric gas sorption data, MOF-5-**C7** shows a discrete transition from the rhombohedral to the cubic phase between 500 and 1000 mbar *n*-butane pressure. This transition is fully reversible upon re-evacuation of the sample (Fig. 4c).

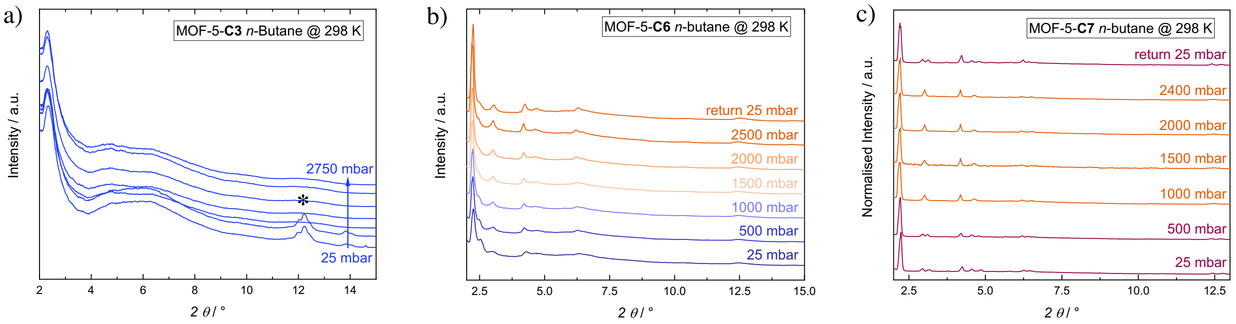

Fig. 4: PXRD patterns of the alkoxy-functionalized MOF-5-**C3** (a), MOF-5-**C6** (b) and MOF-5-**C7** (c) at different *n*-butane pressures collected at BL9 of DELTA. The colour code indicates the phases present: blue - amorphous, orange - cubic and magenta - rhombohedral. Marked reflections (*) stem from the sample holder.

These PXRD data greatly help us to improve our understanding of the unusual phase behaviour of the alkoxy-functionalised MOF-5 derivatives and will be published alongside other data from previous beamtimes at DELTA (variable temperature PXRD) and other light sources (i.e. X-ray total scattering at Diamond Light Source, PXRD under variable CO_2 pressure at DESY). The manuscript is currently under preparation and will be submitted shortly.

The authors thank the DELTA group for granting beamtime and the beamline scientists of BL9, Dr. C. Sternemann and Dr. M. Paulus, for their valuable support during these experiments.

References

[1] A. Schneemann, V. Bon, I. Schwedler, I. Senkovska, S. Kaskel, R. A. Fischer, *Chem. Soc. Rev.* **2014**, *43*, 6062.
[2] Z. Chang, D. H. Yang, J. Xu, T. L. Hu, X. H. Bu, *Adv. Mater.* **2015**, *27*, 5432.
[3] S. Henke, A. Schneemann, A. Wütscher, R. A. Fischer, *J. Am. Chem. Soc.* **2012**, *134*, 9464.
[4] I. Schwedler, S. Henke, M. T. Wharmby, S. R. Bajpe, A. K. Cheetham, R. A. Fischer, *Dalt. Trans.* **2016**, *45*, 4230.
[5] A. Schneemann, P. Vervoorts, I. Hante, M. Tu, S. Wannapaiboon, C. Sternemann, M. Paulus, D. C. F. Wieland, S. Henke, R. A. Fischer, *Chem. Mater.* **2018**, *30*, 1667.
[6] S. Henke, R. Schmid, J. D. Grunwaldt, R. A. Fischer, *Chem. - A Eur. J.* **2010**, *16*, 14296.
[7] G. Férey, C. Serre, *Chem. Soc. Rev.* **2009**, *38*, 1380.
[8] L. Sarkisov, R. L. Martin, M. Haranczyk, B. Smit, *J. Am. Chem. Soc.* **2014***,* *136*, 2228.

Temperature-dependent Behaviour of Oligomer Thin Films

Eduard Mikayelyan[1]*, Linda Grodd*[1]*, Viachaslau Ksianzou*[2]*,*
Daniel Wesner[1]*, Alexander I. Rodygin*[3,4]*, Holger Schönherr*[1]*,*
Yuriy Luponosov[5]*, Sergei Ponomarenko*[3,5]*, Ullrich Pietsch*[1]*, Dimitri A. Ivanov*[3,4,7]*, and Souren Grigorian*[1]
[1] *University of Siegen, Germany*
[2] *Technische Hochschule Wildau, Germany*
[3] *Lomonosov Moscow State University, Russia*
[4] *Moscow Institute of Physics and Technology, Russia*
[5] *Enikolopov Institute of Synthetic Polymeric Materials RAS, Russia*
[6] *Institut de Sciences des Matériaux de Mulhouse, France*

A combination of in-situ electrical and Grazing-Incidence X-ray Diffraction (GIXD) is a powerful tool for studies of correlations between the microstructure and charge transport in thin organic films. The information provided by such experimental approach can help optimizing the performance of the films as active layers of organic electronic devices.

In this work [1], we have investigated the phase transitions in vacuum-deposited thin films of a common organic semiconductor dihexyl-quarterthiophene (DH4T) [2]. The initial crystalline structure exhibits a large number of Bragg reflections allowing assigning it to a monoclinic phase (see Figure). A transition from the initial highly-crystalline phase to a mesophase was detected upon heating, while only a partial backward transition was observed upon cooling to room temperature.

In-situ electrical conductivity measurements revealed the impact of both transitions on charge transport. This is partly accounted for by the fact that the initial crystalline phase is characterized by inclination of molecules in the plane perpendicular to the π-π stacking direction whereas the mesophase is built of molecules tilted in the direction of π-π stacking. Importantly, in addition to the two phases of DH4T characteristic of the bulk, a third interfacial substrate-stabilized monolayer-type phase was observed. The existence of such interfacial structure can have important implications for the charge mobility, being especially favorable for lateral two-dimensional charge transport in the OFET geometry.

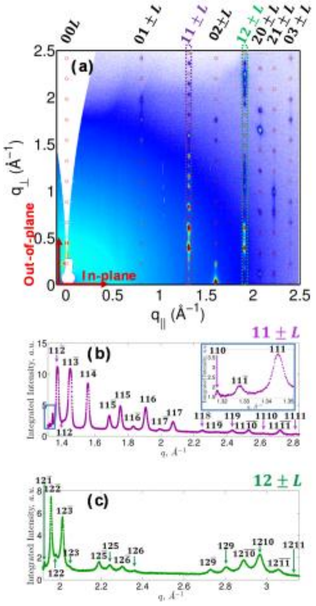

Figure: GIXD patterns of the highly crystalline vacuum deposited DH4T film with overlaid simulated Bragg reflections (red circles) for a monoclinic unit cell. Intensity line profiles measured along $q_\perp$ of 11 ± L (b) and 12 ± L (c) reflection families are given in purple and green color, respectively

1. Mikayelyan, E., Grodd, L., Ksianzau, V., et. al., Phase Transitions and Formation of a Monolayer-Type Structure in Thin Oligothiophene Films: Exploration with a Combined In Situ X-ray Diffraction and Electrical Measurements. Nanoscale Research Letters, 2019. 14:185.
2. Ponomarenko, S. and S. Kirchmeyer, Synthesis and thermal behaviour of α,α'-didecyloligothiophenes. Journal of Materials Chemistry, 2003. 13(2): p. 197-202.

DELTA User Report

Adsorption of ions at OTS-coated surfaces under an electric potential field

Alina Sparenberg, Michael Paulus, Susanne Dogan*, Göran Surmeier, Christian Albers, Juri Forov, Christian Sternemann, Metin Tolan

Fakultät Physik/DELTA, TU Dortmund, 44221 Dortmund, Germany
*corresponding author: susanne.dogan@tu-dortmund.de

Solid-liqud interfaces are highly relevant in nanotechnology, technical applications in chemistry, biomedicine and materials science [1, 2]. Such systems with a hydrophobic interface in contact with an aqueous medium serve as model systems for the characterization of deposition of substances, especially ions [3, 4]. An often used self-assembly molecule is octadecyltrichlorosilane (OTS). To study the ion adsorption at OTS in aqueous solutions x-ray reflectivity (XRR) experiments were performed at the beamline BL9 at DELTA using the 27 keV x-ray reflectivity setup [5]. Figure 1 shows a schematic sketch of the sample system and the corresponding density profile extracted from the measurement presented in the inset. The XRR patterns were detected with the PILATUS 100-K detector. Reflectivity curves from the water-OTS interfaces without salt were recorded as a reference. In the following, the salt concentration in the sample system was varied by adding consecutively salt solution from a stock solution.

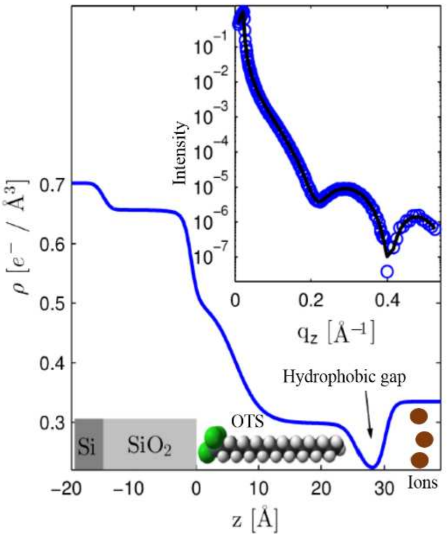

Figure 1: Electron density profile and reflectivity curve of a solid-liquid interface consisting of an OTS coated silicon wafer [8].

Despite various studies and simulations on the so-called hydrophobic gap and the influence of ions on a hydrophobic interface, the adsorption processes are not fully understood and are strongly discussed [6]. To investigate the binding properties, we consider salts with different cation sizes and apply an electric field during adsorption. The silicon wafer with a native silicon dioxide layer on top is negatively charged at a pH-value of 7. Previous studies showed an ion adsorption on the SiO_2-layer that reflects in an increasing OTS-tail group thickness and electron density [7]. This effect is limited on the size of the OTS-layer itself. With large cations, the behaviour can be observed only at higher concentrations. Additionally, the hydrophobic gap shows an increased electron density and altered shape which is not correlated with the cation size. By using 1-butyl-3-methylimid-azolium bromide (BMIM Br) with a large cation and the salts NaBr and CsCl with a small and a large cation (see table 1), we aim for a deeper understanding of both, insights to the penetration and the adsorption mechanism at temporarily changed electrical field. For this purpose a special designed sample cell was used.

Table 1: Used ions and ion sizes.

Ion	**Ion size / Å**
Na^+	1.02
Cs^+	1.67
$BMIM^+$	9
Br^-	1.96
Cl^-	1.81

First, the adsorption pathway on OTS-coated wafer was examined by using a range of different cation sizes in order to verify the previously collected data. The concentration was varied between 0 M and 0.5 M for the BMIM Br^-, up to 0.2 M for the NaBr and 0.1 M for CsCl measurements. In the next step, the adsorption behaviour under an electrical field was tested. Figure 2 inset 1a shows representative Fresnel-normalised XRR-curves of the measurements of BMIM Br^-, the corresponding electron density profiles are presented in inset 1b. As shown here, the electron density increases due to an ion adsorption with increasing concentration in the region of the hydrophobic gap and especially on the top of it. Furthermore, the shape of the gap change significantly and the tailgroup's thickness and density increase slightly.

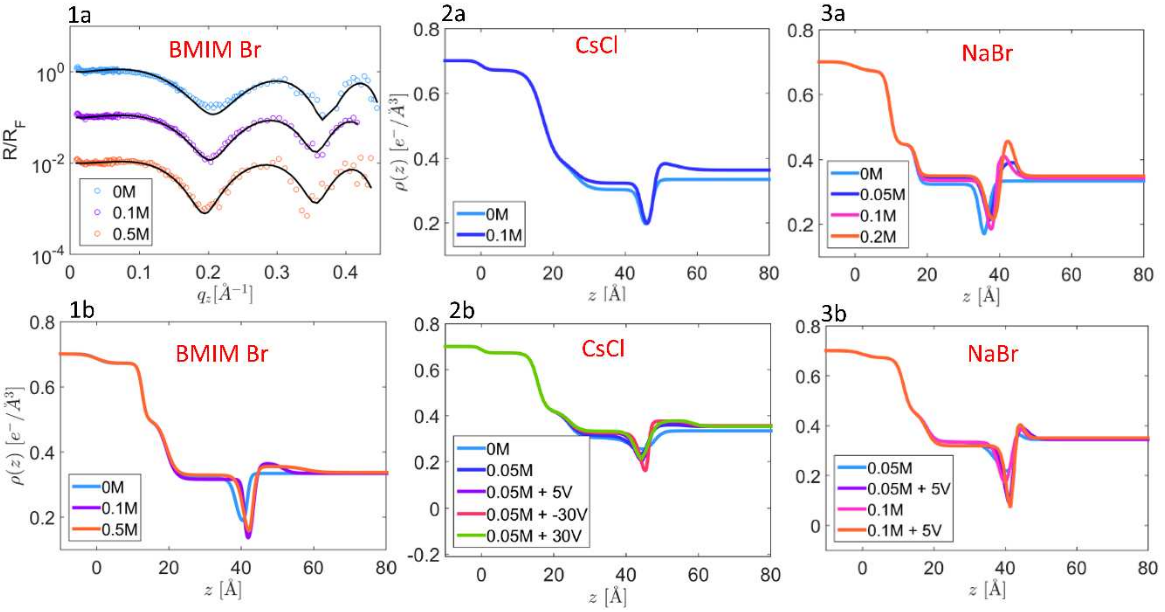

Figure 2: Fresnel-normalized XRR-curves with corresponding electron density profiles and selected electron density profiles of different ions at OTS-coated SiO2-wafer with and without an external electric field.

The influence of NaBr with the smallest monovalent cation Na^+ shows the highest impact on the OTS layer, see figure 2, 3a. With increasing NaBr concentration the amount of adsorbed ion layer increases and the hydrophobic gap sharpens. Moreover, the OTS-tailgroup thickness increases with a simultaneous increase of electron density.

The electron density profiles of OTS-coated silicon wafers in contact with the highest concentration of CsCl are shown in part 2a in figure 2. The smaller concentrations showed the same tendency, which is however less pronounced. The electron density slightly increases in the tail region and on the top of the OTS-layer. An influence on the hydrophobic gap is hardly observed in strength.

We conclude that with the increasing cation size the insertion and penetration into the OTS-layer and thus the line-up of the OTS-molecules is hindered and therefore the changes of the OTS-layer are weak. This concerns the increase of the electron density within the tails and the hydrophobic gap, as well as its shape-change and the deposition as top layer above the OTS-layer. The ion adsorption behaviour as suggested earlier was confirmed.

At all three CsCl concentrations from 0.005 to 0.1 M, the ion deposition at the hydrophobic interface increases with increasing potential and the depth of the hydrophobic gap is reduced. The influence of the electric field on the adsorption of NaBr is shown in part 3b of figure 2. With an electric potential of +5 V the electron density of the OTS-tailgroup at concentrations of 0.05 M and 0.1 M solution decreases and the thickness increases. The electron density of the hydrophobic gap and of the ion adsorbate layer also rises. Although the measured values suggest that the adsorption behaviour changes due to an applied electric field, the processes have not been clarified yet. Thus, it is necessary to confirm the data and to study time effects in more detail.

References

[1] D. Chandler. *Nature* (2005). [2] A. R. Hirst. *Angew. Chem.* (2008). [3] X. Wang. *Nature* (2005). [4] B. Dong. *Langmuir* (2007). [5] M.Paulus *J. Synchrotron Radiat. (2008).* [6] S. H. Donaldson. *Langmuir* (2014). [7] J. Forov Dissertation (2019), TU Dortmund, Dortmund. [8] P.Salmen Dissertation (2017), TU Dortmund, Dortmund.

Acknowledgments

Göran Surmeier (DFG-FOR1979) and Christian Albers (DFG STE 1079/4-1) are funded by the Deutsche Forschungsgemeinschaft (DFG, German Research Foundation). Juri Forov is funded by the Deutsche Forschungsgemeinschaft (DFG, German Research Foundation) under Germany´s Excellence Strategy – EXC 2033 – Projektnummer 390677874. Gefördert durch die Deutsche Forschungsgemeinschaft (DFG) im Rahmen der Exzellenzstrategie des Bundes und der Länder – EXC 2033 – Projektnummer 390677874.

We want to thank the DELTA machine group for providing synchrotron radiation.

Hard X-ray spectroscopy

XANES and EXAFS absorption spectroscopy on cobalt valence tautomers and reference compounds at beamline BL8

Florian Otte[1,2], Christian Sternemann[1], Ralph Wagner[3], Frederico Alves Lima[2], Christian Bressler[2] and Metin Tolan[1]

[1] Fakultät Physik/DELTA, TU Dortmund, 44221 Dortmund, Germany
[2] FXE Instrument, European XFEL GmbH, 22869 Schenefeld, Germany
[3] Materialwissenschaften Fachgruppe Physik Fachbereich C, Bergische Universität Wuppertal, 42119 Wuppertal, Germany

Cobalt-based valence tautomers and reference compounds were studied at BL8 using X-ray absorption spectroscopy (XAS) both in the XANES and EXAFS region. Valence tautomeric (VT) transitions are characterized by stimulated intramolecular charge transfer and single-site spincrossover.[1,2] VT transitions were induced by cooling with an LN2-operated cryojet, which was mounted at a nozzle-distance of approximately 3 mm from the sample position. Fig. 1 shows the setup, with sample pellet, TFY-diode and cryo-nozzle. The incoming photon energy was scanned with an Si(111) monochromator in the range of 7700 eV – 7850 eV at the Co K-edge with an overall energy resolution of 1 eV. Samples were tightly pressed into pellets and glued onto a polymer sample holder. Spectra were measured with the BL8 ionization chamber setup (I0, I1) as well as with the closely mounted large solid angle TFY-diode.

A set of 3 cobalt-based samples was measured. Two compounds served as high-spin (*hs*) and low-spin (*ls*) reference, i.e. the Co^{II} and Co^{III} derivates of Tris(2,2'-bipyridine). The tautomer sample is of general form [$Co(DTB)_2$ X], where the central Co atom is coordinated to three ligands, one ancillary (non-innocent) ligand (denoted by X) and two dioxolene ligands. For the investigated sample, the ancillary ligand was either 2,2'-Bipyridine (bpy).

The current measurement campaign had two goals: (I) collect cobalt reference XAS data and (II) collect temperature dependent XAS spectra of cobalt valence tautomers. A pellet of 300 µm – 500 µm thickness with pure sample was found to give proper absorption in transmission when slightly pressed. Cobalt K-edge XAS reference spectra were collected on the Co^{II} and Co^{III} derivates of Tris(2,2'-bipyridine) and acetylacetonate (c.f. Fig. 2.). The edge-shift and the shape of the metal pre-edge are rationalized by the different charge- and spin-states of the compounds, further analysis is currently pending. Temperature dependent XANES spectra of the tautomer sample show comparable behavior in the post-edge XANES region. The sample did not interconvert back to the original state after heating, reasons for that are und investigation as well as the assessment of the metal pre-edge by DFT-calculations and fitting.

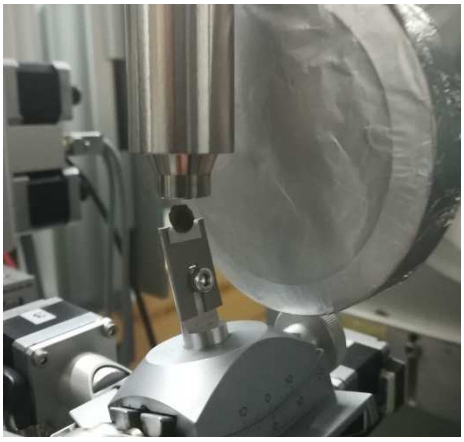

Fig. 1. *Sample enviroment for XANES/EXAFS measurements, showing the cryo-nozzle (top), a mounted pellet and the TFY-diode (right).*

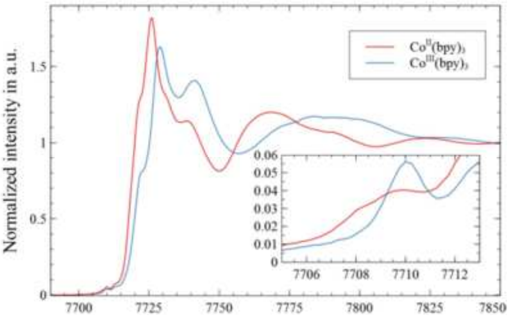

Fig. 2. *Co K-edge XANES spectra for $Co^{II/III}(bpy)_3$, indicating electronic and geometric ls- and hs-fingerprints both in the metal pre-edge as well as the post-edge region.*

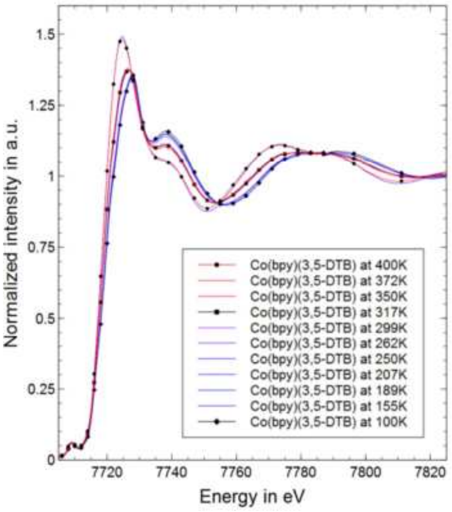

Fig. 3. *Co K-edge XANES spectra for $Co(bpy)(DTB)_2$. Temperature dependent changes in the post-edge XANES region are observable, indicating a geometric change in the measured temperature range. Pre-edge analysis is ongoing.*

References:

1. Shultz, D. A. in Magnetism: Molecules to Materials II 281–306 (Wiley-VCH Verlag GmbH & Co. KGaA, 2003).
2. Hendrickson, D. N. & Pierpont, C. G. in 1, 63–95 (2004).

Acknowledgments:

We would like to thank the DELTA machine group for providing synchrotron radiation and technical support. FO acknowledges funding via BMBF (05K16PE1).

Density determination of liquids in the pressure range up to 5000 bar

Julia Nase, Paul Salmen, Michael Paulus, Christian Sternemann, and Metin Tolan

Fakultät Physik/DELTA, TU Dortmund, D-44221 Dortmund

The knowledge of the density of liquids is of high importance in many fields of research. Densities need to be known e.g., for the exact analysis of Terahertz spectroscopy data or X-ray scattering data. Exact values are also needed to verify theoretical density models and as parameter for Molecular Dynamics simulations of liquids. Densities of liquids are typically measured in a vibrating tube densitometer (VTD) with high accuracy, however limited to a small range of temperature and pressure. Notably, the pressure can be increased to several 100 bar only. Owing to the relevance of high hydrostatic pressure conditions for many fields of research in the last years, the need for density data in the kbar regime was arising. We present a setup to determine densities of liquid samples from X-ray absorption measurements at pressures up to 5000 bar. Comparing to numerical simulations and data from a VTD, we show that relative density changes can be determined reliably in the whole pressure range. Aqueous Trimethylamine-N-oxide solutions were examined. Experiments were performed at beamline BL8 of DELTA (Dortmund, Germany).

Lambert-Beer's law states that the intensity of radiation with energy E is attenuated over the distance d by matter with absorption coefficient (p, E) following $I(d, p, E) = I_0 \exp(-\mu(p, E)\, d)$, where I_0 is the intensity before and I the intensity behind the sample at pressure p. Thus, relative density changes can be determined in one pressure series on the same sample.

Experiments were perfomed at beamline BL8 of DELTA, in an energy range between 16.81 keV and 16.91 keV. The samples consisted of approximately 1 mL of degassed liquids in a dedicated high-pressure cell. The incident and transmitted intensity were measured via ionization chambers. A line was fitted to $\ln(I_0/I)$ and integrated, giving $\mu d_{\mathrm{mean}}(p)$. The data was normalized to the value at 500 bar and set to the density of the corresponding liquid determined in an independent method (VTD). Trimethylamine *N*-oxide (TMAO) solutions with

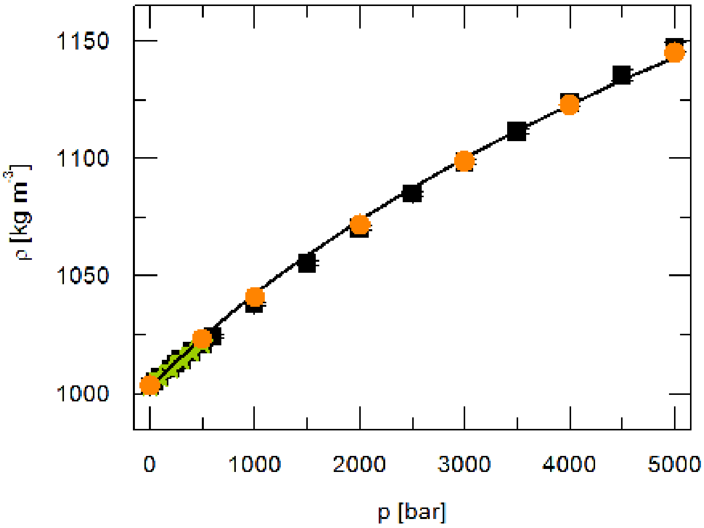

Figure 1: Density of 2 mol/L aqueous TMAO solutions plotted against pressure at 298.15 K. Stars: experimental results from the vibrating-tube density meter, black squares: experimental results from the X-ray absorption measurements, orange circles: MD simulations, line: PC SAFT modeling results using parameters. [1]

c = 2 mol/L were prepared by weighing the appropriate amount TMAO and adding water (MilliQ, resistivity R = 18.2 MΩcm) to the desired volume. The temperature was set to 298.15 K. The pressure stability was better than 1 %. Results of the density measurements are shown in figure 1.

The results agree very well with Molecular Dynamics simulations and theoretical calculations from PC-SAFT theory [1]. While the density of TMAO with c = 2 mol/L is higher than the density of water up to 2000 bar, the opposite is the case above 2000 bar and up to 5000 bar. This result indicates that the compressibility decreases with the TMAO content and can be linked to the stabilizing effect of TMAO on the local H-bond network of water. [1]

Acknowledgements
The authors thank the team of DELTA for providing synchrotron radiation, Dipl.-Phys. Ing. Ralph Wagner for beamline support. The authors acknowledge the DFG (FOR 1979) and RESOLV (EXC 1069) for financial support.

References:

M. Knierbein, C. Held, C. Hölzl, D. Horinek, M. Paulus, G. Sadowski, C. Sternemann, and J. Nase, Density variations of TMAO solutions in the kilobar range: Experiments, PCSAFT predictions, and molecular dynamics simulations. *Biophysical Chemistry* **253** (2019) 106222

Effect of cultivation conditions on the electrochemical activity of metal reducing bacteria (MRB) on stainless steel surfaces

Nina Wurzler[a], Jan David Schütter[a], Ralph Wagner[b],
Dirk Lützenkirchen-Hecht[b], Ozlem Ozcan[a]

[a] *Federal Institute for Materials Research and Testing, Berlin, Germany*
[b] *Bergische Universität Wuppertal, Wuppertal, Germany*

Stainless steel is protecting itself against the onset of corrosion by forming a stable oxide layer composed of iron and chromium oxides [1]. Metal reducing bacteria are known to play a major role in the onset of pitting corrosion due to the ability to use various metallic compounds as electron acceptors. Reducing the stable metal oxides in the protective film to more soluble species may lead to an alteration and weakening of the corrosion resistance of stainless steels [2-5]. To understand the metabolic pathways of metal reduction the bacteria *Shewanella putrefaciens CN32* have been grown with and without the presence of Fe3+ species to examine the adaptation of the bacteria to use iron.

Therefore, ex situ experiments at the Fe K-edge and the Cr K-edge have been performed to elucidate the changes in oxide chemistry after incubation with the bacterial cultures. In an three electrode set-up stainless steel 304 (grind to P1200) was connected as working electrode. A 60 min. mild polarization to +50 mV vs. Ag/AgCl in 20 mM $NaClO_4$ with a gold counter electrode was performed. The steel coupons were then incubated with different solutions. The bacterial cultures regularly grown, in the following named CN32centrif., and grown with iron (Fe(III)-citrate, 16 g/l), named FeCi, as well as the filtered growth medium only with the secreted molecules and EPS (FeCi-filtrate) and the killed bacteria (FeCi-autoclaved) were tested. After 20 h of incubation, the X-ray absorption spectra were obtained.

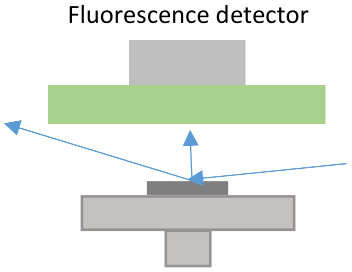

Figure 1: schematics of the ex situ experimental setup.

All the XANES experiments have been performed at DELTA beamline 8 in the grazing incidence mode and the data was collected in total reflection and fluorescence mode using a channel cut Si(111) monochromator and gas-filled ionization chambers as detectors. The samples were placed parallel to the x-ray beam and positioned with a transmission detector. Fluorescence spectra in grazing incidence were analyzed at the Fe and Cr edges after pre-conditioning and after 20 h incubation with different microbial electrolytes.

The XANES spectra at Fe K-edge are presented in Figure 2. The filtrated growth medium as well as the dead/ autoclaved bacterial culture act as control samples. The spectra do not show any changes which can conclude, that neither the secreted substances of the bacteria and their EPS, nor the molecules and compounds of the bacteria itself are actively changing the surface oxide chemistry. The changes that are visible in the spectra after incubation with the two bacterial cultures stem definitively from the active electron transport between bacteria and steel coupon. The CN32centrif samples show a slight increase in absorption in the energy range of oxidic peaks and decrease in the metallic shoulder. Especially the second peak, roughly at 7140 eV, gives hint to the formation of iron oxides. The shift of the peak position to higher energies is accounting for a Fe(III)-oxide or hydroxide species. For the iron grown bacteria (FeCi) this phenomenon seems to be more drastic. An increase of Fe(III)-oxides would act as a protective barrier and helps hindering the onset of corrosion. The reducing activity would on the other hand not give an explanation for the Fe3+ formation – the only reason could be the previously reduced iron species from the bacteria are being reoxidized during the drying process of the sample before recording the spectra.

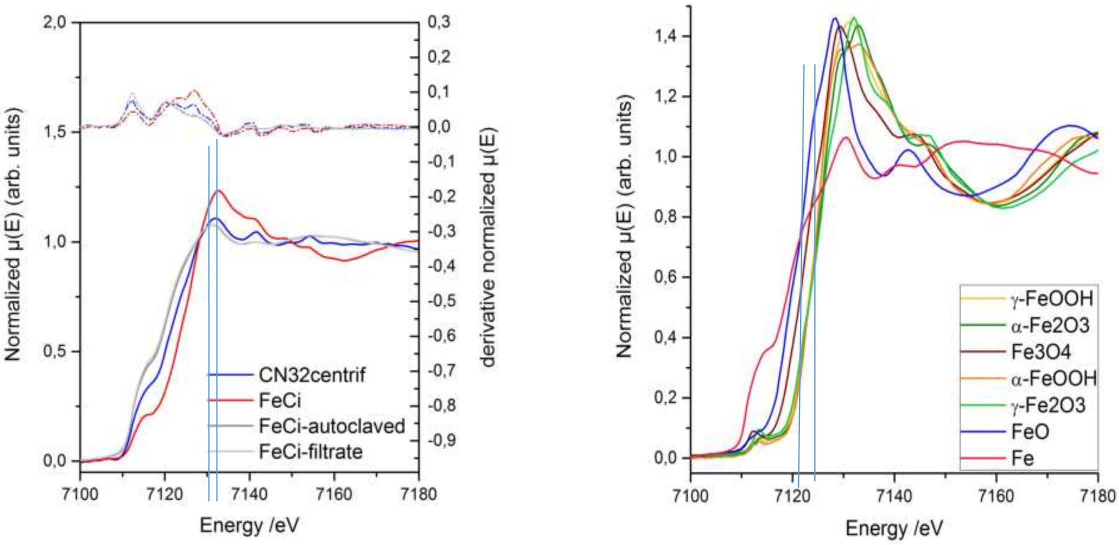

Figure 3: ex situ XANES spectra at Fe K-edge conducted at DELTA beamline 8, left: stainless steel coupons incubated in organic solutions with and without bacteria, spectra taken in grazing incidence detecting reflectivity and fluorescence signal, right: standard reference samples measured in transmission mode.

These findings make in situ measurements mandatory and an in situ cell was designed to study the electroactivity of the bacteria by means of following the open circuit potential (OCP) simultaneously with recording XANES spectra, that help understanding the changes in oxide chemistry (see Figure 3). A model iron thin film (80 nm) was deposited onto a Kapton window facing the interior of the measurement cell and allowing bacterial activity and settlement as well as connecting the iron film as a working electrode to a potentiostat. The cell has a second Kapton window on the opposing site to allow X-ray beam alignment and positioning of the cell via the transmission signal. Once set, the cell can be filled with the bacterial solution and the backwards excited fluorescence emission signals can be detected following the rearrangement of the oxide chemistry due to bacterial activity. The in situ cell was tested and first results could be obtained giving prove to the reduction of iron 3+ species to a mixed Fe2+ oxide / hydroxide which reoxidized in ex-situ experiments.

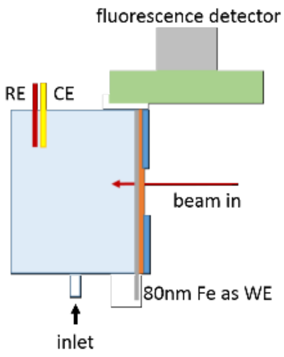

Figure 2: schematics of the in situ cell with a 80 nm Fe film vapor deposited onto Kapton foil and measuring the fluorescence radiation emitted backwards.

Acknowledgement

We gratefully acknowledge the DELTA machine group for providing synchrotron radiation reliably.

References:

[1] H. A. Videla, L. K. Herrera, *International Microbiology* **2005**, *8*, 169-180.
[2] P. Jogdeo, R. Chai, S. Shuyang, M. Saballus, F. Constancias, S. L. Wijesinghe, D. Thierry, D. J. Blackwood, D. McDougald, S. A. Rice, E. Marsili, *Journal of The Electrochemical Society* **2017**, *164*, C532-C538.
[3] E. Marsili, D. B. Baron, I. D. Shikhare, D. Coursolle, J. A. Gralnick, D. R. Bond, *PNAS, Proceedings of the National Academy of Sciences* **2008**, *105*, 3968-3973.
[4] J. K. Fredrickson, J. M. Zachara, D. K. Kennedy, M. C. Duff, Y. A. Gorby, S.-M. Li, K. M. Krupka, *Geochimica et Cosmochimica Acta* **2000**, *64*, 3085-3098; dD. R. Lovley, *Curr Opin Biotechnol* **2008**, *19*, 564-571.
[5] A. A. Carmona-Martínez, F. Harnisch, U. Kuhlicke, T. R. Neu, U. Schröder, *Bioelectrochemistry* **2013**, *93*, 23-29.

Unravelling the local structure of $(Ca/Sr)F_2 \cdot (Eu/Tb)F_3$ luminescent nanoparticles

Ana Guilherme Buzanich [a], Anke Kabelitz [a], Kirill Yusenko [a], Ralph Wagner [b]

[a] *Federal Institute for Materials Research and Testing, Berlin, Germany*

[b] *Bergische Universität Wuppertal, Wuppertal, Germany*

We collected room temperature EXAFS data of $SrF_2/xEuF_3$, $x = 0\text{-}0.4$ nanocolloids at two parallel beamlines. Sr K-edge (EXAFS, BL8) and Eu L_3-edge (XANES, BL10) were measured in parallel from identical samples. All data have been collected using our custom flow-cell for liquid samples. Based on our experience during the experiment, a novel in situ reactor has been designed for further time-resolved experiments. In total, 16 liquid samples at two edges and 16 solid samples (powders diluted with BN) at a single edge were measured.

Our EXAFS and XANES data suggest regularities in compositional dependence of local structure. The local surrounding of Sr atoms systematically changes with Eu concentration (see Fig. 1 below). We correlated data for two sets of samples: i) 0.2-0.3 M colloidal solutions of nanoparticles in ethylene glycol prepared at room temperature and ii) tempered samples after a heat treatment (4 h, 175 °C).

The main difference has been detected for the second coordination sphere of Sr. Distances above 4 Å correspond to Sr-Sr distances in the fluorite structure. At the same time, relatively high coordination numbers of the first coordination sphere (Sr-F distances) correspond to a formation of extra-sites occupied by interstitial fluorides.

Such findings correlate with structural data obtained using complementary X-ray diffraction and pair distribution functions data obtained in June 2019 at the P02.1 beamline at the PETRA III facility.

We are now drafting two publications where we are going to summarize all experimental data obtained so far [1].

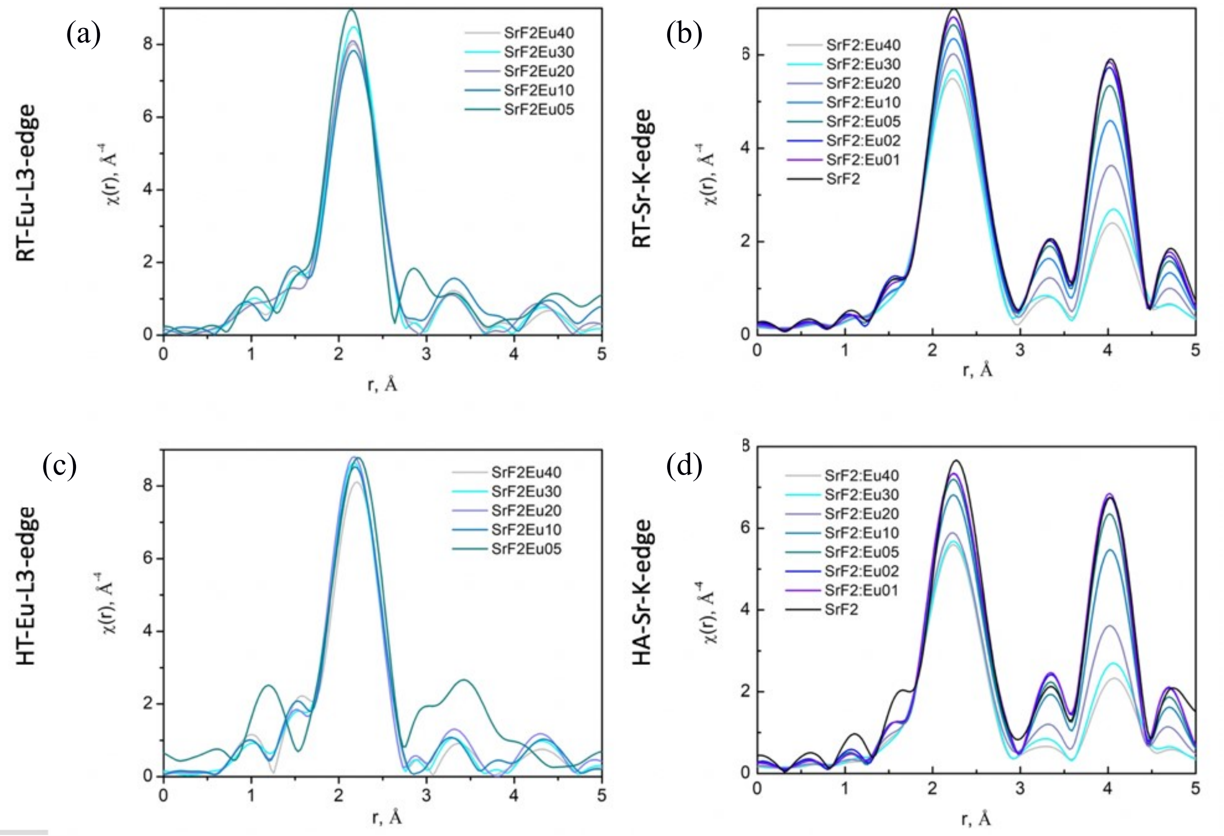

Fig. 1: Magnitude of the Fourier-transform $|FT(\chi(k)*k^3)|$ for the k^3-weighted EXAFS fine structures $\chi(k)$ measured at the Eu L_3-edge (DELTA beamline 10, (a), (c)) and the Sr K-edge (DELTA beamline 8, (b), (d)) of colloidal $SrF_2/x EuF_3$ ($0 \leq x \leq 0.4$) solutions of nanoparticles in ethylene glycol prepared at room temperature ((a), (b)) and after annealing at 175 °C for 4 h ((c), (d)).

References:

[1] K. Yusenko, A. Kabelitz, R. Wagner, T. Krahl, Ana Guilherme Buzanich (2020): Real structure of SrF_2 luminescent nanoparticles, J. Mater. Chem., in preparation.

Von Hamos spectrometer commissioning and Kα X-ray emission spectroscopy on cobalt valence tautomers at beamline BL9

Florian Otte[1,2], Kevin Lehninger[1], Sergio Jannuzzi[3], Christian Sternemann[1], Robin Sakrowski[1], Mirko Elbers[1], Frederico Alves Lima[2], Christian Bressler[2] and Metin Tolan[1]

[1] Fakultät Physik/DELTA, TU Dortmund, 44221 Dortmund, Germany
[2] FXE Instrument, European XFEL GmbH, 22869 Schenefeld, Germany
[3] MPI for Chemical Energy Conversion, Mülheim, Germany

In continuation of earlier commissioning campaigns on the wavelength-dispersive von Hamos spectrometer assembly at BL9, a newly designed support frame was tested and aligned. Following this, Kα X-ray emission spectroscopy (XES) measurements on cobalt complexes were performed.

The support stage offers precise and fast positioning of 2 analyzer-crystal modules and corresponding X-ray detectors with respect to the sample and will allow a fully motorized spectrometer operation at BL9 once completely commissioned. Briefly, one support stage consists of a motorized vertical stage that carries the 4-crystal JJ X-ray von Hamos spectrometer module, which is mounted at a fixed radial distance from the sample position. Variation of the analyzer-array's vertical position changes the incident Bragg-angle onto the analyzers, thus tuning the analyzed energy window of the spectrometer. Bragg-reflected photons from the analyzers are collected onto a PILATUS 100K-S detector (a 2D and spatially resolved silicon-based detector). Its vertical position can be adjusted by means of a second motorized stage. A third, manual, degree of freedom allows for azimuthal rotation of both analyzer module and detector around the sample position (access of forward or backward scattering geometries). For simultaneous use (e.g. "two-color" XES measurements) or for combined XES and X-ray Raman scattering experiments, the spectrometer support frame offers the possibility to mount and position two detector-analyzer pairs at the same time (Fig. 1.).

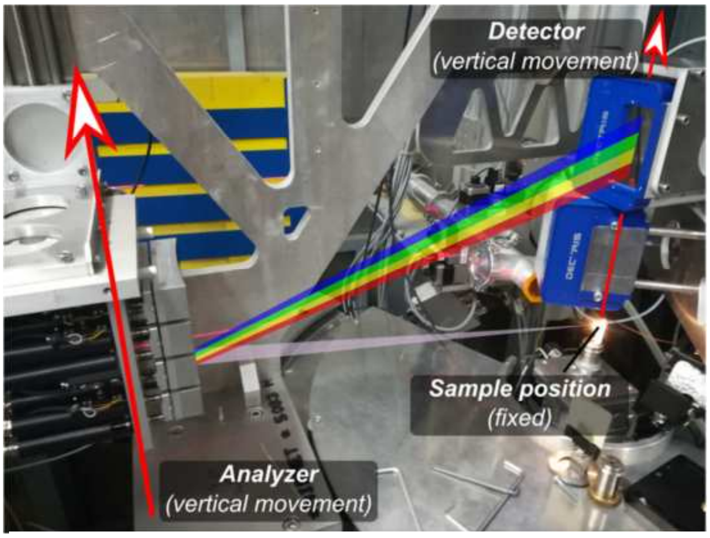

Fig. 1. *Newly installed von Hamos spectrometer. A scheme shows the dispersive working principle of the spectrometer. The disc-shaped bottom-plate can be removed to give greater accessibility.*

The movable vertical stages of the spectrometer eased the optical alignment process and especially all necessary adjustments with X-rays considerably. Advantageous are also the improvements in reproducibility of aligned setups and stability, the decrease of time for setup-changes and the possibility of the dual-spectrometer setup.

A second goal of this experiment was the collection of Kα XES of cobalt valence tautomers. Valence tautomeric (VT) transitions are characterized by stimulated intramolecular charge transfer and single-site spincrossover.[1,2] VT transitions were induced by cooling with an LN2-operated cryojet, which was mounted at a nozzle-distance of approximately 5 mm from the sample position. For the spectrometer, four Si(531) crystals were used in 1st order reflection, using a Bragg-angle of 77.01 degree. In this configuration, both emission lines (Co $K\alpha_1$ at 7615.30 eV and Co $K\alpha_2$ at 7630.32 eV) easily fit onto the PILATUS detector sensitive area. The incoming photon beam was tuned to an energy of 8000 eV with a Si(311)-monochromator, and cropped down to a beam size of 1.5 x 0.6 mm^2 (V x H) with slits in front of the sample. To reduce unwanted scattered background, extensive shielding around the sample was put into place. A helium-filled bag was used in between detector, spectrometer and sample to reduce air-scattering and -absorption. In this configuration, typical integration times to collect an emission spectrum were around 5400 s – 7200 s per sample. For installation of the shielding segments and optical alignment, a battery-powered lightbulb at the sample position proved to be very useful. This could be further improved by using a smaller light source, thus giving sharper lines on the detector during focus optimization.

A set of six cobalt-based samples were measured. Four compounds do not undergo any VT transitions and served as high-spin (*hs*) and low-spin (*ls*) reference (Co^{II} and Co^{III} derivates of Tris(2,2'-bipyridine) and acetylacetonate). The tautomer samples are of general form [Co(DTB) 2 X], where the central Co atom is coordinated to three ligands, one ancillary (non-innocent) ligand (denoted by X) and two dioxolene ligands. For the investigated samples, the ancillary ligand was either 2,2'-bipyridine (bpy) or 4,4'-diphenyl-2,2'-bipyridine (dpbpy). The dpbpy-sample did not show any transition and is not further discussed here.

For Co(bpy)(DTB)$_2$, a strong temperature dependence of the Kα emission line shape was found. For two temperatures the Kα XES spectra are shown in Fig. 2., amongst *hs*- and *ls*- reference data. While the Kβ emission line is commonly used to track spin-state characteristics of transition metal complexes due to its sensitivity towards the 3d orbitals via 3p-3d orbital interactions, here, the Kα emission line spectral changes hint towards the possibility of serving as a suitable footprint for the VT transition. This is of special importance for future time-resolved measurements on those compounds, where the tenfold stronger Kα emission lines are attractive as first experimental indicator of the VT transition.

Kα XES was recorded at a series of temperature points. In a first approach, two fitting-techniques were used to track the spectral changes over temperature in the recorded XES data. As seen in Fig. 3., the experimental data show a clear trend with temperature, going from *ls*-character or lower Kα$_1$ -FWHM values at low temperatures below 200K to hs-character or larger Kα$_1$ -FWHM values at high temperatures above 350 K. Further analysis is pending. The temperature control via the cryojet proved challenging. This might also be reflected in the scattering of the recorded data points, as the true sample temperature was not always precisely known. An improvement here would be to use a different type of cryostat or use secondary precise thermometers at the sample position to monitor true sample temperature.

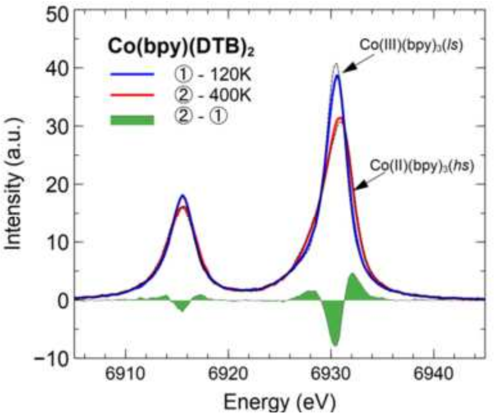

Fig. 2. *Co Kα emission spectra of Co(bpy)(DTB)2 at high and low temperatures. For comparison a* hs- *and* ls-*reference is shown as thin black solid lines.*

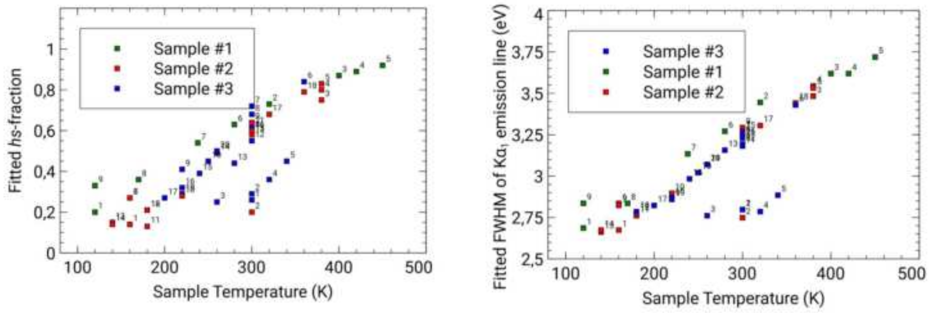

Fig. 3. *Fitted XES Kα data showing a transition over temperature for Co(bpy)(DTB)$_2$. Samples #1-#3 are the same compound, measured for different temperature ramping. Left: Kα spectra were fitted as a linear combination of Co(II)(bpy)$_3$ (a hs reference) and Co(III)(bpy)$_3$ (ls reference). Right: FWHM-value extracted from a double pseudo-Voigt fit to the Kα$_1$ emission line. Visible are outliers at the beginning of the measurements, hinting towards an annealing behavior of the samples.*

References:

1. Shultz, D. A. in Magnetism: Molecules to Materials II 281–306 (Wiley-VCH Verlag GmbH & Co. KGaA, 2003).
2. Hendrickson, D. N. & Pierpont, C. G. in 1, 63–95 (2004).

Acknowledgments:

We would like to thank the DELTA machine group for providing synchrotron radiation and technical support. FO and ME acknowledge funding via BMBF (05K16PE1) and RS via DFG (STE 1079/2-1).

Kβ X-ray emission spectroscopy on cobalt valence tautomers at beamline BL9

Florian Otte[1,2], Kevin Lehninger[1], Christian Sternemann[1], Christian Albers[1], Jennifer Bolle[1], Robin Sakrowski[1], Frederico Alves Lima[2], Christian Bressler[2] and Metin Tolan[1]

[1] Fakultät Physik/DELTA, TU Dortmund, 44221 Dortmund, Germany
[2] FXE Instrument, European XFEL GmbH, 22869 Schenefeld, Germany

In this experiment, K$\beta_{1,3}$ X-ray emission spectra of cobalt valence tautomers were measured using a 4-crystal von Hamos spectrometer available at beamline BL9 of DELTA. Valence tautomeric (VT) transitions are characterized by stimulated intramolecular charge transfer and single-site spincrossover.[1,2] VT transitions were induced by cooling with an LN2-operated cryojet, which was mounted at a nozzle-distance of approximately 5 mm from the sample position. For the spectrometer, four Ge(111) crystals were used in 4th order reflection, yielding a Bragg-angle of 82.91 degree. The incoming photon beam was tuned to an energy of 8300 eV with a Si(311)-monochromator, and cropped down to a beam size of 1.5 x 0.3 mm^2 (V x H) with slits in front of the sample. Shielding around the sample was put into place. A helium-filled bag was placed in between detector, spectrometer and sample to reduce air-scattering. In this configuration, typical integration times were around 5400 s – 8400 s per sample.

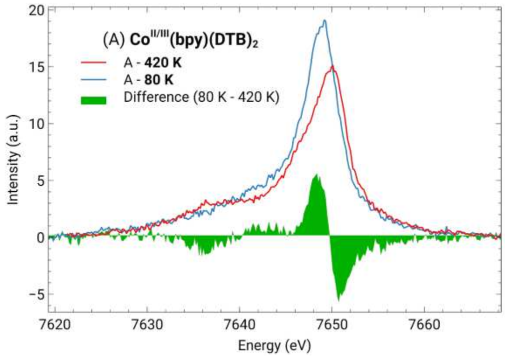

***Fig.1**. Co Kβ emission spectra of Co(bpy)(DTB)$_2$ at high and low temperatures.*

A set of six cobalt-based samples was measured. Four compounds do not undergo any VT transitions and served as high-spin (*hs*) and low-spin (*ls*) reference (Co^{II} and Co^{III} derivates of Tris(2,2'-bipyridine) and acetylacetonate). The tautomer samples are of general form [Co(DTB) 2 X], where the central Co atom is coordinated to three ligands, one ancillary (non-innocent) ligand (denoted by X) and two dioxolene ligands. For the investigated samples, the ancillary ligand was either 2,2'-Bipyridine (bpy) or 1,10-Phenanthroline (phen). The phen-sample did not show any transition and is not further discussed here. For Co(bpy)(DTB)$_2$, a strong temperature dependence of the Kβ emission line shape was found. For two temperatures the Kβ XES spectra are shown in Fig. 1. The reference compounds' Kβ spectra are shown in Fig. 2 and Fig. 3.

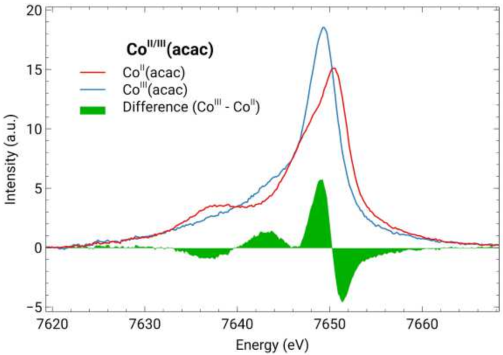

***Fig.2**. Co Kβ emission spectra of Co$^{II/III}$(acac) references.*

Kβ XES for the tautomer sample was recorded at a series of temperature points, further analysis regarding the spin-state as a function of temperature is pending.

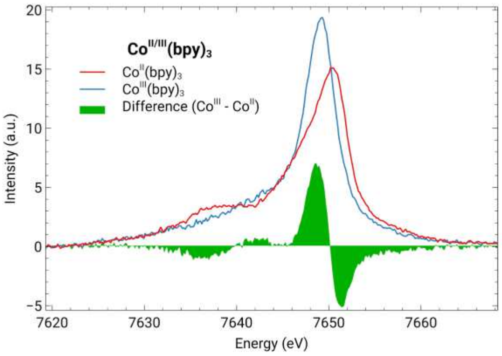

***Fig.3**. Co Kβ emission spectra of Co$^{II/III}$(bpy) references.*

References:

1. Shultz, D. A. in Magnetism: Molecules to Materials II 281–306 (Wiley-VCH Verlag GmbH & Co. KGaA, 2003).
2. Hendrickson, D. N. & Pierpont, C. G. in 1, 63–95 (2004).

Acknowledgment

We would like to thank the DELTA machine group for providing synchrotron radiation and technical support. FO, RS, CA acknowledge funding via BMBF (05K16PE1), DFG (STE 1079/2-1) and DFG (STE 1079/4-1), respectively.

Cobalt-doping of barium aluminate ($BaAl_2O_4$) as investigated by XANES

M. Vrankić[a], A. Šarić[a], S. Bosnar[a], D. Lützenkirchen-Hecht[b], R. Wagner[b]

a) Ruđer Bošković Institute, Division of Materials Physics, Bijenička 54, 10000 Zagreb, Croatia.
b) Bergische Universität Wuppertal – Fakultät für Mathematik und Naturwissenschaften, Gauß-Str. 20, 42097 Wuppertal, Germany.

Barium aluminate $BaAl_2O_4$ exhibits interesting luminescence properties when it is doped with cations such as Eu, Ce, Cr and other elements [1-4]. Despite the actual use of doped barium aluminate in optoelectronic devices e.g. for optical communication technologies [5], structural investigations have not yet been precisely performed so far. In previous studies, we have investigated the structural modifications of $BaAl_2O_4$ induced by doping with Cr [6] and Eu [7]. Here we will focus on investigations of Co-doped barium aluminate as a continuation of those experiments. Powder samples of Co-doped $BaAl_2O_4$ and pure $BaAl_2O_4$ were prepared by a hydrothermal method and subsequent annealing in air at 1100 °C for 4 h. The Co K-edge X-ray absorption experiments described here have been performed at DELTA beamline 10, using a Si (111) channel-cut monochromator [8]. N_2-gas-filled ionization chambers were used for the incident intensities, while an Ar-filled ionization chamber was used for the beam transmitted through the sample. Fluorescence radiation was detected by a silicon drift diode with a multichannel analyzer and a large area passivated implanted planar silicon (PIPS) detector, respectively. Repeated scans each of typically 1 h acquisition time were performed and averaged in order to improve the data statistics. For comparison, reference spectra of a Co-metal foil and several cobalt oxides of different chemical valences and compositions (i.e. CoO, Co^{2+}, with 6-coordinated Co-O, Co_3O_4 with equal amounts of 4-coordinated Co^{2+} and 6-coordinated Co^{3+}, and Co_2O_3 with pure Co^{3+} and 6 oxygen neighbors) were measured. From the X-ray absorption spectra measured at the Ba L-edges and the Co K-edge, the total concentration of Co within the sample was estimated. Assuming the presence of stoichiometric $BaAl_2O_4$ with a density of 3.94 g/cm^3, the concentration of the Co within the sample was calculated (1.55 ± 0.26) % Co per formula unit.

In Fig. 1, Co K-edge XANES spectra of $BaAl_2O_4$ doped with 1.5 at.% Co are compared to those of the Co reference compounds. As can be seen, the edge position in the spectrum of the Co-doped $BaAl_2O_4$ - sample is substantially different from that of metallic Co and CoO, so that the presence of pure Co^{2+} in the doped barium aluminate can be excluded. However, the edge positions determined for Co_3O_4 and Co_2O_3 are very similar, so that the discrimination of both samples solely from the edge position appears difficult (see inset of Fig. 1). However, according to a linear regression fit of the edge positions of the reference spectra, the edge position obtained for the Co-doped sample (7718.2 eV) is larger than that obtained for Co_2O_3 and is located ideally on the linear regression, indicating that a formal Co – valence of 3+ is very likely.

Pure $BaAl_2O_4$ obeys a hexagonal crystal structure in the space group $P6_3$ at room temperature, with two structurally inequivalent Ba^{2+}-sites and four different Al^{3+}-sites [9, 10]. While barium atoms are 9-fold coordinated with Ba-O distances in the range from 2.69-3.00 Å, aluminum atoms are 4-fold coordinated with Al-O distances in the range of 1.71-1.83 Å. Co^{3+} - ions exhibit an ionic radius of 60 pm [11]. Thus, a substitution of Al^{3+} with an ionic radius of 53 pm [11] by Co^{3+} in the doped sample appears much more likely in contrast to a substitution on regular, 9-coordinated Ba^{2+}-sites with substantially larger ionic radii.

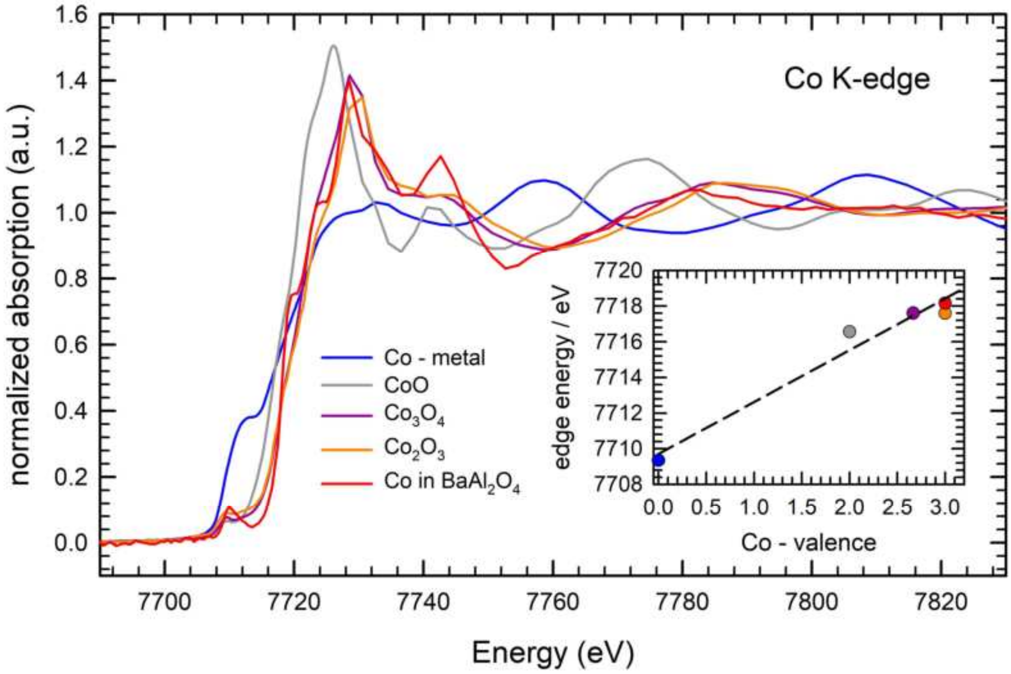

Fig. 1: Comparison of background-subtracted and normalized XANES spectra of Co-metal (—), CoO (—), Co_3O_4 (—), Co_2O_3 (—) and Co-doped $BaAl_2O_4$ (—). In the inset, the edge position determined as the first inflexion point of the spectra is shown as a function of the formal valence of the reference samples, together with a linear regression of the data points. From the edge position measured for the Co-doped $BaAl_2O_4$ sample, a valence of +3 can be determined.

However, much more structural information is required to prove such an interpretation. Therefore ongoing research will consider (i) the refinement of X-ray diffraction data and (ii) measurements and fitting of the extended X-ray absorption fine structure to confirm the present results.

References

[1] Z. Lou, J. Hao, M. Cocivera, J. Phys. D: Appl. Phys. 35 (2002) 2841.
[2] V. Singh, V. Natarajan, J.-J. Zhu, Opt. Mater. 29 (2007) 1447.
[3] T. Nakamura, K. Kaiya, N. Takahashi, T. Matsuzawa, C.C. Rowlands, V. Beltrán-López, G.M. Smith, P.C. Riedi, Phys. Chem. Chem. Phys. 1 (1999) 4011.
[4] M. Peng, G. Hong, J. Lumin. 127 (2007) 735.
[5] C. Kim, I. Kwon, C. Park, Y. Hwang, H. Bae, B. Yu, C. Pyun, G. Hong. J. Alloys Compounds 311 (2000) 33.
[6] M. Vrankić, B. Gržeta, D. Lützenkirchen-Hecht, S. Bosnar, A. Šarić, Inorg. Chem. 54 (2015) 11127.
[7] B. Gržeta, D. Lützenkirchen-Hecht, M. Vrankić, S. Bosnar, A. Šarić, M. Takahashi, D. Petrov, M. Biščan, Inorg. Chem. 57 (2018) 1744.
[8] D. Lützenkirchen-Hecht, R. Wagner, S. Szillat, A.K. Hüsecken, K. Istomin, U. Pietsch, R. Frahm. J. Synchrotron Rad. 21 (2014) 819.
[9] W. Hörkner, H.K. Müller-Buschbaum. Z. Anorg. Allg. Chem. 451 (1979) 40.
[10] S.-Y. Huang, R. von der Mühll, J. Ravez, J.P. Chaminade, P. Hagenmüller, M. Couzi. J. Solid State Chem. 109 (1994) 97.
[11] http://www.wiredchemist.com/chemistry/data/metallic-radii

EXAFS investigations of a noblegas treatment of Nb at elevated temperatures

P. Rothweiler, J. Kläs, R. Wagner, D. Lützenkirchen-Hecht

Fakultät 4-Physik, Bergische Universität Wuppertal, Gaußstr. 20, 42097 Wuppertal, Germany

Heat treatments of niobium-based particle accelerator cavities are nowadays routinely carried out under nitrogen gas atmospheres to improve the RF-superconducting properties of the Nb-materials [1-6]. Furthermore, a substantial lowering of the surface resistance and the quality factor of the cavities was also reported for treatments in Ar gas [3]. While the structural modifications of the cavities under nitrogen exposure are intensively studied by numerous groups worldwide, no such investigations have been performed during or after an equivalent noble-gas exposure up to now. Due to the positive experience obtained from EXAFS investigations of nitrogen-doping [7], we have used EXAFS spectroscopy for in-situ studies of niobium heat treatments in Ar- and Kr-atmospheres and temperatures of up to 1200 °C.

The in-situ preparation was performed in a dedicated, remote controlled vacuum chamber (base pressure ca. 10^{-7} mbar) with a ceramic heating plate, featuring heating rates of more than 500 °C/minute are possible, while cooling takes much more time. For the present experiment, smooth Nb metal films with a thickness of 7.5 μm were first annealed in vacuum for 1 h at 900 °C, and subsequently exposed to (4.0) Kr-gas with pressures of 3 mbar or 30 mbar, respectively, for varying times. For comparison, some samples were prepared in dilute Ar atmospheres, and some samples were annealed at 1200 °C. EXAFS data at the Nb K-edge (18986 eV) were collected in transmission mode prior to any heat treatment as well as during the different process steps at elevated temperature. Furthermore, the samples were investigated after the cool-down to room temperature under vacuum and under Kr/Ar atmospheres (the latter to prevent the loss of noble gases during cooling). The samples were also measured at 100 K, in order to improve the data quality and to reduce thermal disorder in the samples. All the experiments presented here were performed at the wiggler beamline 8 of the DELTA storage ring (Dortmund, Germany) [8].

The data analysis comprised a background subtraction and a Fourier-transformation of the k^3-weighted X-ray absorption fine structure $\chi(k)*k^3$. This radial distribution function was back-transformed into k-space for 1.5 Å $\leq$ R $\leq$ 3.5 Å and fitted with calculated phase and amplitude functions (FEFF 8, [9]) using the bcc Nb lattice (space group Im-3m, no 229) with a lattice parameter of 3.30 Å as a starting parameter. In order to minimize the potential correlation of the determined distances and the inner potential shift ΔE_0, ΔE_0 was simultaneously fitted for all measured spectra, and thus trends in the data can be interpreted in a straightforward manner. Furthermore, the amplitude reduction factor S_0^2 was treated as global fit parameters for all considered Nb-Nb-shells, and the distances R_1 and R_2 of the first two Nb-Nb shells as well as the related mean squared displacement σ_1^2 and σ_2^2 of those shells were fitted separately for each data set. Fits were optimized using k^1-, k^2- and k^3-weighted fine structure data $\chi(k)$ simultaneously.

As can be seen in Fig. 1, the results obtained for R_1 and R_2 scatter around the values expected for bulk niobium, i.e. $R_1 \approx 2.86$ Å and $R_2 \approx 3.30$ Å, with no systematic trends. Some of the samples were heat-treated in the commissioning phase of the high-temperature cell with insufficient vacuum conditions – those samples (indicated accordingly) suffered from a slight oxidation of the Nb according to XANES data, and show slightly larger nearest neighbor distances, probably due to the formation of Nb-oxides. This observation is contradicting to the EXAFS results obtained after Nb-treatments in N_2: The continuous increase of both Nb-Nb bond lengths with increasing N_2-exposure can be explained by an increasing occupation of octahedral vacancy sites by N-atoms, leading to a slight expansion of the host lattice with N_2-exposure. In the latter case, the increasing uptake of nitrogen in the Nb-lattice also leads to a substantial increase of the (static) disorder (σ_1^2 and σ_2^2). In contrast, for noble-gas treatments, no systematic trend was found for the heat-treated Nb-foils. In particular, for the second coordination shell, σ_2^2 is almost constant for all the investigated samples. Thus, for the conditions in temperature, pressure and time used here, we cannot give any evidence for a substantial accumulation of noble metals in the Nb lattice from the measured and analyzed X-ray absorption data.

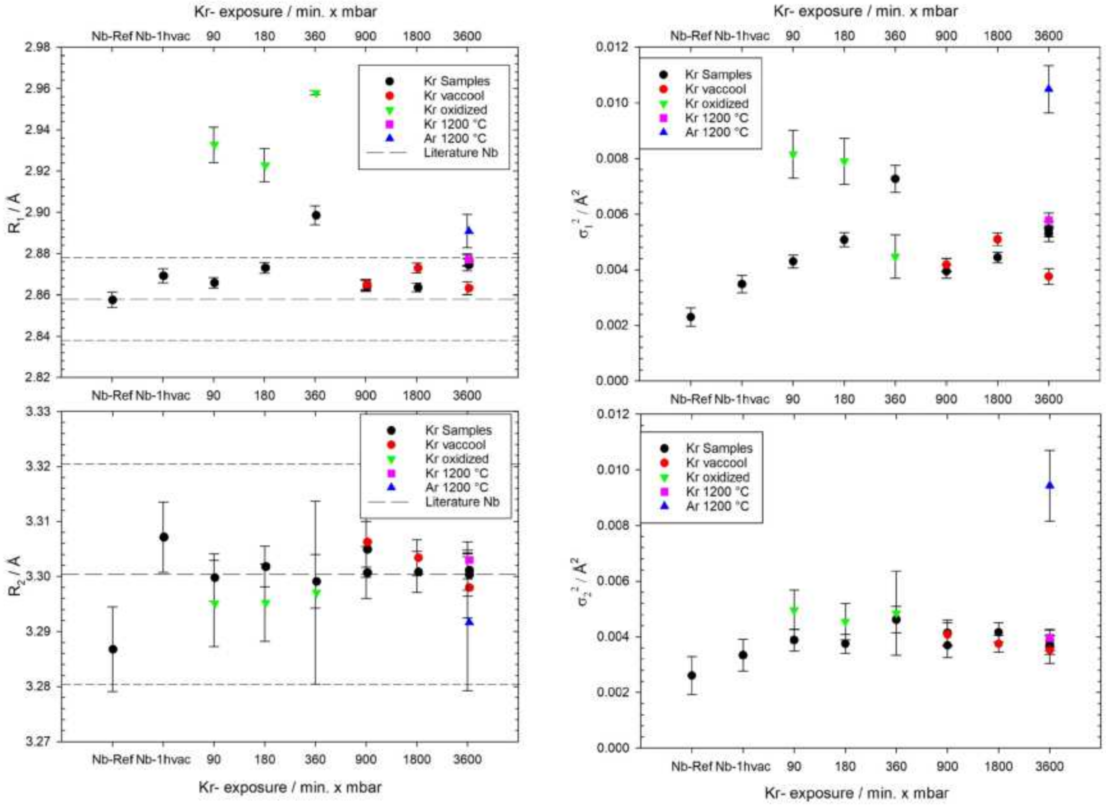

Fig. 1: Results obtained from an EXAFS data fitting procedure applied to Nb-samples exposed to Kr at 900 °C, the exposure is calculated as the product of the exposure time and the applied pressure. The fit was applied in the radial range from 1.5 Å to 3.5 Å and only comprises the first two Nb-Nb coordination shells, i.e. the distances R_1 and R_2, and the disorder σ_1^2 and σ_2^2 (k-range for the Fourier-transform: 2.6 Å^{-1} $\leq$ k $\leq$ 15.0 Å^{-1}, R-range for the fit: 1.5 Å $\leq$ R $\leq$ 3.5 Å). The literature values for $R_1 \approx 2.86 \pm 0.02$ Å and $R_2 \approx 3.30 \pm 0.02$ Å are indicated by dashed horizontal lines. All the samples were measured at 100 K to suppress thermal disorder and to pronounce the effects related to the heat treatments in the noble gas atmospheres. For comparison, examples of a sample heated at 1200 °C and in Argon atmosphere are also included.

Acknowledgement

We gratefully acknowledge the DELTA machine group for providing synchrotron radiation for the experiments. The financial support of the BMBF under project No. 05H15PXRB1 and 05H18PXRB1 is gratefully acknowledged.

References

[1] H. Padamsee, Supercond. Sci. Technol. 14 (2001) R28.

[2] M. Pham Tu, K. Mbaye, L. Wartski, J. Halbritter, J. Appl. Phys. 63 (1988) 4586.

[3] A. Grasselino, A. Romanenko, O. Melnychuk, Y. Trenikhina, A. Crawford, A. Rowe, M. Wong, D. Sergatskov, T. Khabiboulline, F. Barkov, Supercond. Sci. Technol. 26 (2013) 102001.

[4] A. Grassellino, A. Romanenko, S. Posen, Y. Trenikhina, O. Melnychuk, D.A. Sergatskov, M. Merio, M. Checchin, M. Martinello, In: Proceedings SRF2015, Whistler, BC, Canada, (2015) MOBA06, pp 748.

[5] D. Gonnella, R. Eichhorn, F. Furuta, M. Ge, D. Hall, V. Ho, G. Hoffstaetter, M. Liepe, T. O'Connell, S. Posen, P. Quigley, J. Sears, V. Veshcherevich, A. Grassellino, A. Romanenko, D.A. Sergatskov, J. Appl. Phys. 117 (2015) 023908.

[6] A. Dangwal Pandey, G. Dalla Lana Semione, A. Prudnikava, T.F. Keller, H. Noei, V. Vonk, Y. Tamashevich, E. Elsen, B. Foster, A. Stierle, J. Mater. Sci. 53 (2018) 10411.

[7] J. Kläs, R. Wagner, B. Bornmann, R. Frahm, D. Lützenkirchen-Hecht, DELTA annual report (2018) 131.

[8] D. Lützenkirchen-Hecht, R. Wagner, U. Haake, A. Watenphul, R. Frahm, J. Synchrotron Rad. 16 (2009) 264.

[9] A.L. Ankudinov, B. Ravel, J.J. Rehr, S.D. Conradson, Phys. Rev. B 58 (1998) 7565.

XANES investigations of pea plants exposed to soil contaminated with Cu nanoparticles

P. Mathiak, R. Wagner, R. Frahm, D. Lützenkirchen-Hecht

Fakultät 4-Physik, Bergische Universität Wuppertal, Gaußstr. 20, 42097 Wuppertal, Germany

As a continuation of previous studies [1 - 3], the present experiments are meant to investigate the uptake and location of Cu nanoparticles (NPs) in peas, and to provide information about the influence of Cu NPs on micronutrients in the exposed pea plants. The study is motivated by the use of Cu-NPs in particular in the agricultural sector [4], and a potential risk to introduce those NPs into the food chain, for example through contamination of food crops [5, 6]. In this context, it is not clear how the NPs are stored within the plants, and if a biotransformation of metal nanoparticles occurs in the plants, i.e. there is a huge lack of information especially for copper NPs (e.g. [7-9]).

For the present study, commercial seeds of a regional German cultivar „kleine Rheinländerin" peas (Pisum sativum) were grown in soils with well-defined loads of CuNPs, here a mixture of sand and garden mould (500 g and 400 g dry mass per pot, respectively) was loaded with 125, 250, 500, and 1000 mg/kg of nCu powder in 1.8 kg air-dried potted soil (P1 - P4), respectively. Two different sizes of the Cu NPs were used, i.e. 25 nm and 60-80 nm, as obtained from Iolitec (IoLiTec-Ionic Liquids Technologies GmbH, Heilbronn, Germany). The pea-plants were cultivated for 11 weeks in an open greenhouse and irrigated with rainwater. Flourishing of the cultivated peas took place after five weeks, and first fruits were observed one week later. The plants were finally harvested after 11 weeks and separated from the soil. The roots were repeatedly and carefully washed with water to remove any remaining soil from the plant materials. Subsequently, roots, stems with leaves and seed pods were air-dried separately.

XANES experiments were performed at beamline 10 of the DELTA storage ring [10], making use of the Si (111) channelcut monochromator and an ionization chamber in front and behind the samples to measure the X-ray absorption spectra in the vicinity of the Cu K-edge (8980 eV). The sample preparation includes fine-cutting of the different plant materials, and a distribution of the materials on adhesive Kapton tapes. The fruits were pestled into a fine powder and dispensed on Kapton tape. Cu speciation was done in all roots (P1-P4) and the fruits of the sample with highest Cu NP exposure (P4), for both sizes of the Cu NPs. Due to the low Cu-concentrations within the samples, the XANES spectra were collected in fluorescence mode, using either a large area PIPS-diode or a a peltier-cooled Silicon-Drift-Diode (SDD, Amptek XR-100 SDD) with a pulse processor and a multichannel analyzer. Typical acquisition times of 5-10 s for each data point and repeated scans are required to obtain a XANES data quality suited for further analysis. The obtained spectra were compared to reference compounds such as the spectrum of the used Cu nanoparticles, Cu_2O, CuO, Cu-glutathione, Cu-histidine, and Cu-nicotianamine. Spectra of the latter three samples were kindly provided by Ana Mijovilovich [11]. Data analysis comprised a linear combination fitting with the spectra of all the reference compounds mentioned above. In addition, the samples were also measured at the Fe K-edge (7112 eV) and the Zn K-edge (9659 eV), as those elements are also important for the biology sample.

In Fig. 1, XANES spectra from sample P3 (500 mg/kg of nCu powder in 1.8 kg potted soil) and their linear combination fits are compared for the two sizes of Cu NPs investigated here. First of all, Cu histidine is detectable in almost all plant samples. In contrast to previous experiments [3], the concentration of Cu nicotianamine appears lower in the present study, and also small contributions of CuO are detectable. Cu_2O and metallic Cu were not observed in any of the particles. In general, the Cu chemical valence as deduced from the exact position of the Cu k-edge in comparison to those of Cu reference compounds, has a value close to +2.

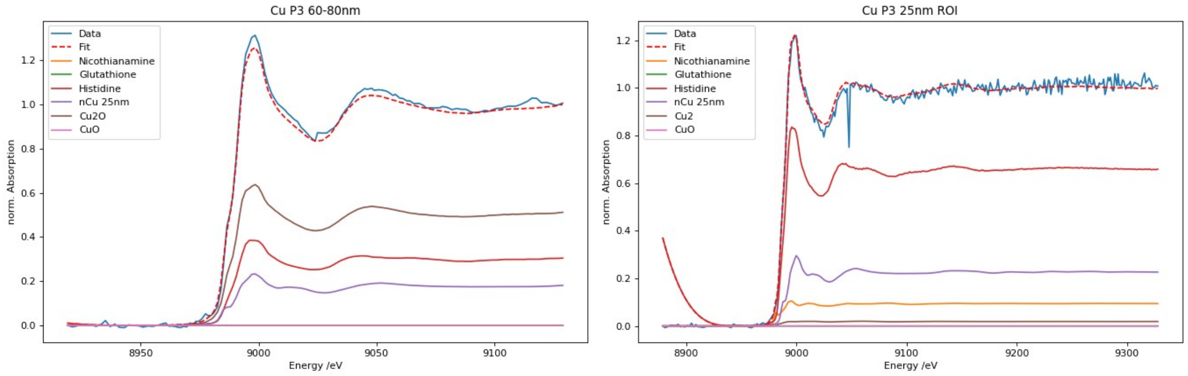

Fig. 1: Cu K-edge fluorescence mode X-ray absorption near edge spectra of root samples obtained from pea plants grown in soil loaded with 500 mg/kg of nCu powder in 1.8 kg potted soil (samples P3) for two sizes of the Cu NPs (left 60-80 nm, right 25 nm).

A main goal of the study was, to obtain general trends for the samples. As such, a reduction of the Cu-histidin content with decreasing Cu concentration in the soil was found, while the nicotianamine content seems to increase. Cu-glutathione is practically not detectable in any of the samples. A more systematic analysis is currently under way. For future experiments, it is planned to refine the XANES data analysis, and to speciate the contributions from the metal cations in more detail, in particular those of Cu, by means of EXAFS experiments.

Acknowledgement

The like to thank Prof. Dr. G. Lohaus for the opportunity to use her greenhouse facilities for the germination and the growth of the pea plants investigated here. We furthermore acknowledge the DELTA machine group for providing synchrotron radiation for the presented experiments, and for the allocation of beamtime.

References

[1] C.O. Ogunkunle, B. Bornmann, R. Wagner, P.O. Fatoba, R. Frahm, D. Lützenkirchen-Hecht, DELTA annual report (2016) p. 81.
[2] P. Mathiak, R. Wagner, R. Frahm, D. Lützenkirchen-Hecht, DELTA annual report (2018) p. 127.
[3] C.O. Ogunkunle, B. Bornmann, R. Wagner, P.O. Fatoba, R. Frahm, D. Lützenkirchen-Hecht, Environmental Nano-technology, Monitoring & Management 12 (2019) 100231.
[4] J. Trujillo-Reyes, S. Majumdar, C.E. Botwz, J.R. Peralta-Videa, J.L. Gardea-Torresdey, J. Hazard. Mater. 267 (2014) 255.
[5] Y.-N. Chang, M. Zhang, L. Xia, J. Zhang, G. Xing, Materials 5 (2012) 2850.
[6] M.L.J. Xu, H. Iwai, Q. Mei, D. Fujita, H. Su, H. Chen, N. Hanagata, Sci. Rep. 2 (2012) 406.
[7] P. Zhang, Y. Ma, Z. Zhang, X. He, J. Zhang, Z. Guo, R. Tai, Y. Zhao, Z. Chai, ACS Nano 6 (2012) 9943.
[8] M.L. Lopez-Moreno, G. de la Rossa, J.A. Hernandez-Viezcas, H. Castillo-Michei, C.E. Botez, J.R. Peralta-Videa, J.L. Gardea-Torresdey, Environ. Sci. Technol. 44 (2010) 7315.
[9] Y. Ma, P. Zhang, Z. Zhang, X. He, J. Zhang, Y. Ding, J. Zhang, L. Zhang, Z. Guo, L. Zhang, Z. Chai, Y. Zhao, Environ. Sci. Technol. 49 (2015) 10668.
[10] D. Lützenkirchen-Hecht, R. Wagner, S. Szillat, A. K. Hüsecken, K. Istomin,U. Pietsch, R. Frahm, J. Synchrotron Rad. 21 (2014) 819.
[11] A. Mijovilovich, B. Leitenmaier, W. Meyer-Klaucke, P.M.H. Kroneck, M. Götz, H. Küpper, Plant Physiol. 151 (2009) 715.

Notes

Notes